

# UC Irvine

## UC Irvine Electronic Theses and Dissertations

### Title

Linkage-based Orthoses Designed for Individualized Motion Requirements

### Permalink

<https://escholarship.org/uc/item/8195k0m1>

### Author

Ghosh, Shramana

### Publication Date

2017

Peer reviewed|Thesis/dissertation

UNIVERSITY OF CALIFORNIA,  
IRVINE

Linkage-based Orthoses Designed for Individualized Motion Requirements

DISSERTATION

submitted in partial satisfaction of the requirements  
for the degree of

DOCTOR OF PHILOSOPHY

in Mechanical and Aerospace Engineering

by

Shramana Ghosh

Dissertation Committee:  
Professor J. Michael McCarthy, Chair  
Professor Nina P. Robson  
Professor David Reinkensmeyer

2017



# DEDICATION

To my parents and mentors

# TABLE OF CONTENTS

	Page
<b>LIST OF FIGURES</b>	<b>vi</b>
<b>LIST OF TABLES</b>	<b>x</b>
<b>ACKNOWLEDGMENTS</b>	<b>xi</b>
<b>CURRICULUM VITAE</b>	<b>xii</b>
<b>ABSTRACT OF THE DISSERTATION</b>	<b>xiv</b>
<b>1 Introduction</b>	<b>1</b>
1.1 Overview of Orthotic Devices . . . . .	1
1.2 Finger Orthoses . . . . .	2
1.3 Lower-leg Assistive Devices: Knee-Ankle-Foot Orthosis (KAFO) . . . . .	7
1.3.1 Locked Knee KAFOs . . . . .	9
1.3.2 Stance Control KAFOs (SC-KAFOs) . . . . .	11
1.3.3 Active KAFOs . . . . .	13
1.3.4 Multi-axis Knees . . . . .	15
1.4 Motion Analysis . . . . .	17
1.4.1 Optical Motion Capture . . . . .	18
1.4.2 Motion Capture of Human Thumb . . . . .	18
1.4.3 Motion Capture of Lower-leg . . . . .	21
1.5 Geometric Design of Planar Linkages . . . . .	25
1.5.1 Overview . . . . .	26
1.5.2 Complex Notation . . . . .	27
1.5.3 Design Equations . . . . .	28
1.6 Performance Optimization of Linkages . . . . .	29
1.6.1 Overview . . . . .	29
1.6.2 Objective Functions . . . . .	30
1.6.3 Constrained Optimization . . . . .	31
1.6.4 Optimization Approaches . . . . .	32
1.7 Contributions . . . . .	33

<b>2</b>	<b>Design of Passive Mechanical Thumb Orthosis</b>	<b>35</b>
2.1	Introduction . . . . .	35
2.2	Design Procedure . . . . .	36
2.2.1	Individualized Task Specifications using Thumb Motion Capture . . . . .	36
2.2.2	Kinematic Synthesis of Four-bar Thumb . . . . .	41
2.2.3	Synthesis Results . . . . .	44
2.3	Thumb Orthosis . . . . .	45
2.4	Summary . . . . .	46
<b>3</b>	<b>Design of Passive Mechanical Multi-Axis Knee</b>	<b>49</b>
3.1	Introduction . . . . .	49
3.2	Design Procedure . . . . .	50
3.2.1	Individualized Task Specification using Gait Data . . . . .	50
3.2.2	Kinematic Synthesis of Knee Linkage . . . . .	53
3.2.3	Synthesis Results . . . . .	57
3.3	Multi-Axis Hands-free Crutch . . . . .	58
3.4	Pilot Study of Prototype & Results . . . . .	59
3.5	Summary . . . . .	61
<b>4</b>	<b>Design of Knee-Ankle-Foot Orthosis based on Six-Bar Linkage</b>	<b>64</b>
4.1	Introduction . . . . .	64
4.2	Design Procedure . . . . .	65
4.2.1	Individualized Task specifications based on Lower-leg Motion Capture Data . . . . .	65
4.2.2	Kinematic Synthesis of Six-bar Knee-Ankle-Foot Orthosis . . . . .	71
4.2.3	Synthesis results . . . . .	75
4.3	Knee-Ankle-Foot Orthosis Prototype . . . . .	78
4.4	Pilot Study of Prototype & Results . . . . .	80
4.5	Summary . . . . .	85
<b>5</b>	<b>Performance Optimization of Knee-Ankle-Foot Orthoses</b>	<b>86</b>
5.1	Introduction . . . . .	86
5.2	Forward Kinematics of Stephenson III Six-bar Linkage . . . . .	88
5.3	Formulation of Objective Function for Performance Optimization . . . . .	92
5.3.1	Angular Movement Error Function . . . . .	92
5.3.2	Metatarsal Trajectory Constraints . . . . .	96
5.4	Performance Optimization of Lower-leg Linkage . . . . .	102
5.4.1	Selection of Target Curve . . . . .	102
5.4.2	Selection of Design Variable Vector . . . . .	104
5.4.3	Selection of Initial Designs . . . . .	105
5.4.4	Solution of Performance Optimization Problem . . . . .	107
5.5	Results . . . . .	108
5.6	Summary . . . . .	111

<b>6</b>	<b>Conclusion</b>	<b>113</b>
6.1	Summary . . . . .	113
6.2	Future Work . . . . .	115
	<b>Bibliography</b>	<b>117</b>
<b>A</b>	<b>Mathematica Code</b>	<b>126</b>
A.1	Import and Plot Motion Capture Data . . . . .	126
A.1.1	Transformation of Lower-leg Data . . . . .	130
A.1.2	Transformation of Thumb Data . . . . .	134
A.1.3	Motion Capture Data for Thumb Trajectory . . . . .	137
A.1.4	Motion Capture Data for Knee Trajectory . . . . .	141
A.1.5	Motion Capture Data for Metatarsal Trajectory . . . . .	142
A.2	2R Synthesis with Position, Velocity and Acceleration Constraints . . . . .	145
A.3	Performance Optimization . . . . .	152
A.3.1	Objective Function . . . . .	152
A.3.2	Grid Search . . . . .	159

# LIST OF FIGURES

	Page
1.1 Classification of orthoses based on modality of providing assistance. . . . .	2
1.2 Previously developed hand/finger rehabilitation devices. (a) The mentor [9], (b) FINGER curling robot [10], (c) Single DOF finger exoskeleton [11], (d) Robotic finger exoskeleton with slider mechanism [12]. . . . .	3
1.3 Previously developed hand devices including the thumb. (a) Index and thumb rehabilitation device [18], (b) A 3 DOF thumb motion assist mechanism [19], (c) Two spatial CRR-RRR thumb guidance mechanisms [20], (d) Three fingered hand exoskeleton [21], (e) The BRAVO active hand orthosis [22], (f) A Watt I six-bar thumb curling exoskeleton [23]. . . . .	5
1.4 Stationary gait rehabilitation machines. (a) Schematic of driven gait orthosis, Lokomat [30]. (b) Schematic of ARTHuR [26]. (c) Schematic of LOPES [27]. (d) Active orthoses ALEX [28]. . . . .	7
1.5 Passive stationary gait rehabilitation machines. (a) A Gait Rehabilitation system using a four-bar mechanism [31]. (b) A ten-bar mechanism to guide gait [32]. (c) A cam-linkage mechanism rehabilitation robot [33]. . . . .	8
1.6 Gait trainers. (a) The Stephenson II six-bar linkage used in a wheeled gait trainer [35]. (b) A single DOF passive orthosis [36]. (c) A gravity balancing passive orthosis [37]. . . . .	9
1.7 An example of a commercially available KAFO device [39]. . . . .	10
1.8 An example of a KAFO with locked knee joint and carbon fiber spring ankle joint [40]. . . . .	10
1.9 Joint ROM controlled SC-KAFO. Locking and unlocking mechanism of the Ottobock Free Walk and Becker UTX [44]. . . . .	12
1.10 (a) The Horton Stance Control Knee and (b) the Fillauer Swing Phase Lock [44]. . . . .	12
1.11 Becker Orthopedic 9001 E-Knee [44]. . . . .	13
1.12 The Ottobock C-Brace. . . . .	14
1.13 Multi-axis knee mechanisms. (a) Knee brace design with four-bars [55], (b) & (c) Crossed four-bar knee joint for orthoses [56, 57], (d) Six-bar prosthetic knee mechanism [58], (e) Four-bar prosthetic knee joint [59], (f) Crossed four-bar prosthetic knee mechanism [60], (g) Four-bar knee mechanism controlled by MR damper [61]. . . . .	16
1.14 The experimental setup showing the capture space and four of the seven Qualisys <i>OQUS500+</i> cameras used for motion capture of hand movement. . . . .	19

1.15	(a) Marker placement locations of the hand to study grasping motion. (b) Motion Capture still displaying the thumb capture data. . . . .	20
1.16	The anatomy of the human hand [64]. . . . .	20
1.17	Kinematic model of the thumb in XZ plane. . . . .	21
1.18	Experimental set up for motion capture data collection for locomotion. . . .	22
1.19	(a) The L-frame placed on the capture space's floor to set the capture volume's origin and axes. (b) Marker placement locations of the lower leg to study normal walking. . . . .	23
1.20	The geometry of the knee joint in the sagittal plane [65]. . . . .	24
1.21	(a) Marker placement locations of the lower leg to study normal walking. (b) Motion Capture still displaying the capture data in 2D (X-Z) consisting of markers (black points), left leg markers are connected with line segments in red, right leg markers are connected by line segments in blue. . . . .	25
1.22	Human gait through one cycle in the sagittal plane, beginning and ending at heel strike. . . . .	26
1.23	Three types of task specifications for kinematic synthesis. . . . .	27
1.24	A 2R chain in the complex plane. . . . .	28
2.1	2D Motion Capture stills of thumb at the beginning and end of the planar curling task. . . . .	37
2.2	Position, velocity (blue) and acceleration (magenta) data at the tip of thumb during its curling motion. . . . .	38
2.3	Velocities (blue) and accelerations (magenta) calculated at the beginning and end of the thumb trajectory. . . . .	39
2.4	Task specifications for synthesis of a 2R chain to produce thumb trajectory: The green frames indicate position specification, blue lines indicate velocity specifications, and the magenta line indicated the acceleration specification. . . . .	40
2.5	The kinematic task for synthesis of a 2R chain. . . . .	41
2.6	A general planar 2R chain displayed in the 1 <sup>st</sup> and 2 <sup>nd</sup> task positions. . . . .	42
2.7	Result of synthesis of mechanical thumb at its (a) initial and (b) final positions in Mathematica. . . . .	45
2.8	Conceptual design of the thumb assistive device. . . . .	46
2.9	Classification of the individualized four-bar thumb orthosis designed based on modality of providing assistance. . . . .	47
2.10	Full-scale 3D printed prototype of the thumb orthosis. . . . .	48
3.1	Motion capture data of the lower-leg when the thigh held fixed. The knee joint trajectory in the sagittal plane over a complete gait cycle is indicated in magenta. . . . .	51
3.2	Trajectories of infra-red markers placed at knee and ankle joints during natural walking, transformed with respect to the thigh fixed frame. . . . .	52
3.3	Position, velocity and acceleration data overlaid on the knee trajectory obtained from motion capture data of an individual walking. The blue arrows on the knee position data indicate the direction of knee joint movement over a single gait cycle starting and ending at heel strike. . . . .	53

3.4	The various sets of kinematic specifications at the knee joint trajectory. Task positions are indicated with a coordinate frame, velocity specifications are indicated with blue, and acceleration is shown in magenta. . . . .	54
3.5	The selected kinematic specifications on the knee trajectory. Task positions are indicated with a coordinate frame, velocity specifications are indicated with blue, and acceleration is shown in magenta. . . . .	54
3.6	A four-bar linkage shown at the two tasks specified. The black frames indicate position specifications, blue lines denote velocity and magenta lines show the acceleration specification. . . . .	55
3.7	The synthesized four-bar linkage at the two task positions specified. . . . .	58
3.8	Classification of the individualized four-bar linkage based multi-axis hands-free crutch based on modality of providing assistance. . . . .	59
3.9	Solid model of the fabricated four-bar linkage. . . . .	60
3.10	Full-scale prototype of the multi-axis hands free crutch. . . . .	61
3.11	Gait Analysis of experimental data obtained from pilot test of walking with the MHC. . . . .	62
3.12	Comparison of knee height of the test subject walking normally, with a fixed-knee HFC, and with the MHC. . . . .	63
4.1	The lower leg transformed in the sagittal plane when the thigh is held stationary.	66
4.2	Knee joint angle variation over a complete gait cycle, beginning and ending at heel strike. Gray lines indicate knee angles calculated for a single gait cycle, and blue line indicates the average knee angle obtained from the motion data over seven gait cycles. . . . .	67
4.3	Ankle joint angle variation over a complete gait cycle, beginning and ending at heel strike. Gray lines indicate ankle angles calculated for a single gait cycle, and blue line indicates the average ankle angle obtained from the individual's motion data over seven gait cycles. . . . .	67
4.4	Kinematic model of the lower leg in the sagittal plane when the thigh is held fixed. The curve traced by the LToe marker gives the metatarsal trajectory with respect to a thigh fixed frame. . . . .	68
4.5	A Stephenson III path generator obtained by coordinating the RR joints with a Stephenson II function generator (adapted from [96]). . . . .	70
4.6	(a) Eleven specified task points on the foot trajectory, (b) The function between $\nu$ and $\zeta$ , the input and output of the 2R serial chain (c) The function between $\psi$ and $\zeta$ , the input and output angles of the Stephenson II function generator. . . . .	72
4.7	Stephenson II six bar linkage (adapted from [71]). . . . .	73
4.8	Design candidates I & II. . . . .	76
4.9	Design candidates III & IV. . . . .	76
4.10	Design candidates V & VI. . . . .	77
4.11	A solid model of the individualized six-bar linkage based knee-ankle-foot orthosis. The locations of the pivots of the six-bar linkage are indicated. . . .	79
4.12	Classification of the individualized six-bar linkage based knee-ankle-foot orthosis based on modality of providing assistance. . . . .	80

4.13	The components of the individualized knee-ankle-foot orthosis designed based on a planar six-bar linkage. . . . .	81
4.14	Evolution of design of link $DGH$ . . . . .	81
4.15	Reduced scale 3D printed model of the orthotic device. . . . .	82
4.16	Full scale prototype of the KAFO device. . . . .	82
4.17	Metatarsal trajectory of a healthy subject walking with and without the KAFO device compared to design predictions. . . . .	83
4.18	Knee angle of a healthy subject walking with and without the KAFO device compared to design predictions. . . . .	83
4.19	Ankle angle of a healthy subject walking with and without the KAFO device compared to design predictions. . . . .	84
5.1	Geometry of the Stephenson III six bar linkage. . . . .	88
5.2	Relative orientations of moving links of the Stephen III six-bar linkage in the $j^{th}$ position (adapted from [71]). . . . .	93
5.3	A linkage (a) without and (b) with a closed and continuous metatarsal trajectory between precision points numbered 1 and 10. . . . .	98
5.4	Two branches of a given linkage. . . . .	99
5.5	The Jacobian determinant values for a given linkage during one gait cycle. . . . .	99
5.6	Bounding boxes of the coupler curve (blue) and the target trajectory (gray). . . . .	100
5.7	The numerical procedure for performance optimization of the lower-leg KAFO mechanism. . . . .	103
5.8	Set of 50 points obtained from basis spline of the motion data. . . . .	104
5.9	Initial designs for the performance optimization of six-bar KAFO. . . . .	106
5.10	Visualization of the grid of positions where the objective function is to be evaluated. . . . .	108
5.11	Comparison of Design Candidate 1 with the optimal linkage solution. . . . .	109
5.12	Comparison of Design Candidate 4 with the optimal linkage solution. . . . .	109
5.13	Comparison of Design Candidate 5 with the optimal linkage solution. . . . .	110
5.14	Solid model of the optimized design solution IV that is selected to be developed as a KAFO device. . . . .	111
5.15	Prototype of the new KAFO device. . . . .	111

# LIST OF TABLES

	Page
2.1 Dimensions of a 2R chain that models the planar motion of the human thumb obtained from motion capture data. . . . .	37
2.2 The anthropomorphic task data obtained from the motion capture of the curling movement of a human thumb. . . . .	41
2.3 The synthesis solutions for the pivot locations of the 2R constraint (in bold) that achieves the anthropomorphic contact and curvature task requirements. . . . .	44
3.1 Task specifications for synthesis of four-bar knee linkage. . . . .	55
3.2 The chosen solutions for the simultaneous synthesis of the two planar 2R mechanical knee linkage. . . . .	58
4.1 Selected pivot positions and dimensions for the 2R lower-leg kinematic model at the beginning of the cycle. . . . .	68
4.2 Coordinates of point P on the 2R backbone chain at the task positions selected for synthesis task, and the corresponding values of $\Delta\nu$ and $\Delta\zeta$ , the input and output of the 2R serial chain and, $\Delta\psi$ and $\Delta\zeta$ , the input and output angles of the Stephenson II function generator. . . . .	71
4.3 Design parameters for Design Candidates I & II (all pivot locations are given in mm). . . . .	75
4.4 Design parameters for Design Candidates III & IV (all pivot locations are given in mm). . . . .	77
4.5 Design parameters for Design Candidates V & VI (all pivot locations are given in mm). . . . .	77
5.1 Input data and variables for the synthesis and optimization process . . . . .	104
5.2 Design parameters of the optimal design solution I (all pivot locations are given in mm). . . . .	108
5.3 Design parameters of the optimal design solution IV (all pivot locations are given in mm). . . . .	110
5.4 Design parameters of the optimal design solution V (all pivot locations are given in mm). . . . .	110

## ACKNOWLEDGMENTS

I owe the deepest gratitude to Prof. Nina P. Robson and to Prof. J. Michael McCarthy, my co-advisors, whose constant support, guidance and encouragement made it possible to carry out my graduate work. In particular, I would like to express my sincerest appreciation to Prof. McCarthy for always being so approachable and incredibly generous with his time, for sharing his deep passion for kinematics, and for inspiring and supporting the explorations in my work. I also want to thank Prof. David J. Reinkensmeyer for taking an interest in my work, serving on my committee, and providing constructive advice.

I am truly grateful to Dr. Mark Plecnick for his help and guidance on synthesis of six-bar linkages, Prof. Gim Song Soh for his advice on synthesis of finger linkages, and Prof. Alba Perez-Garcia for sharing her knowledge of human hands and grasping. I would like to thank Zonghao ‘Benjamin’ Liu for creating the beautiful CAD models used in this work. I would also like to thank Dr. Neda Hassanzadeh, Abhijit Mahakal, Vanessa Corralez-Yang, Uriel Jiminez, Hilen Rocha, Abdulsahib Al-Hazza, Abdullaaziz Al-Kharas, Ahmed Shehab, Kevin Masone, Carresa Brewer, Jeffery Glabe and Sihao Xu for their valuable contributions to our collaborative projects, and time they spent working with me during this period.

I would like to thank my lab mates, Mark Plecnick, Kaustubh Sonawale, Brian Parrish, Brandon Tsuge, Yang Liu, Jeffery Glabe, Peter Wang, Benjamin Liu, Carresa Brewer, and Sihao Xu for sharing their time and knowledge, and for all the crazy and wonderful conversations we have enjoyed over the years. Their support and friendship have made the last four years incredibly rewarding, and some of the best that I have known. Most of all, I would like to thank my loved ones - my family and my friends.

I would also like to gratefully acknowledge the support of the department of Mechanical and Aerospace Engineering at UC Irvine and the National Science Foundation.

# CURRICULUM VITAE

Shramana Ghosh

## EDUCATION

**Ph.D. in Mechanical and Aerospace Engineering** 2017  
University of California *Irvine, CA*

**M.S. in Industrial Engineering** 2013  
Texas A&M University *College Station, TX*

**B.E. in Manufacturing Processes and Automation Engineering** 2011  
University of Delhi *New Delhi, India*

## WORK EXPERIENCE

**Graduate Research Assistant** 2013-2017  
University of California, Irvine *Irvine, California*

**Teaching Assistant** 2014-2017  
University of California, Irvine *Irvine, California*

**Intern** 2015  
Khalifa University of Science Technology and Research *Abu Dhabi, U.A.E*

**Intern** 2014  
California State University Fullerton *Fullerton, California*

**Graduate Research Assistant** 2011-2013  
Texas A&M University *College Station, Texas*

**Intern** 2012  
University of Tsukuba *Tsukuba, Japan*

## PUBLICATIONS

Hassanzadeh, N., Ghosh, S., Robson, N., 2018, "In-Hand Manipulative Synthesis Using Velocity Subspaces". *Advances in Robot Kinematics 2016*, pp. 235-244, Springer.

Ghosh, S., Robson, N., McCarthy, J.M., 2017, "Design of Wearable Lower Leg Orthotic Based on Six-Bar Linkage". *ASME International Design Engineering Technical Conference*.

Ghosh, S., Robson, N., McCarthy, J.M., 2017, "Development of Customized Orthotics Based on Lower-Leg Anthropometric Data and Task". *International Conference on Applied Human Factors and Ergonomics*, pp. 54-63.

Ghosh, S., Gan, D., 2016, "Design of Passive 3-PRR Planar Parallel Manipulators for Self-Alignment of Exoskeleton Axes". ASME International Design Engineering Technical Conference.

Hassanzadeh, N., Ghosh, S., Robson, N., Perez-Gracia, A., 2016, "Velocity Fields and Tangent Bundles for In-Hand Manipulative Synthesis". Advances in Robotic Kinematics.

Robson, N., Ghosh, S., 2015, "Geometric Design of Planar Mechanisms Based on Virtual Guides for Manipulation". Robotica, 34(12), pp. 2653-2668.

Robson, N., Ghosh, S., McCarthy, J.M., 2015, "Simultaneous Geometric Design of Mechanical Fingers for Coordinated Movement". Proceedings of the 14th IFToMM World Congress, pp. 392-402.

Ghosh, S., Robson, N., McCarthy, J.M., 2015, "Geometric Design of a Passive Mechanical Knee for Lower Extremity Wearable Devices Based on Anthropomorphic Foot Task Geometry Scaling". ASME International Design Engineering Technical Conference.

Ghosh, S., Robson, N., 2014, "Development of a One degree of Freedom Mechanical Thumb Based on Anthropomorphic Task for Grasping Applications". Advances in Robot Kinematics, pp. 335-344.

Robson, N., Ghosh, S., Soh, G.S., 2013, "Development of a Sensor-Based Glove Device for Extracting Human Finger Motion Data used in the Design of Minimally-Actuated Mechanical Fingers". Proceedings of 3rd IFToMM International Symposium on Robotics and Mechatronics.

Ghosh, S., Moon, H.S., Robson, N., 2013, "Reconstructing Human's Hand Motion: Preliminary Results and Applications in the Design of Mechanical Fingers for Anthropomorphic Tasks". ASME International Design Engineering Technical Conference.

Ghosh, S., Singh, S.P., 2011, "Optimizing Feeding Systems". Assembly Line Theory and Practice, InTech.

Singh, S.P., Ghosh, S., Khanna, P., 2009, "Mathematical performance analysis of a reciprocating-fork hopper feeder". IEEE Student Conference on Research and Development (SCORED), pp. 464-467.

# ABSTRACT OF THE DISSERTATION

Linkage-based Orthoses Designed for Individualized Motion Requirements

By

Shramana Ghosh

Doctor of Philosophy in Mechanical and Aerospace Engineering

University of California, Irvine, 2017

Professor J. Michael McCarthy, Chair

This dissertation presents and demonstrates a new design procedure for customized wearable devices that provide joint guidance, support, and increased mobility for individuals with hand or lower-leg impairments. This new procedure uses motion capture data to guide kinematic synthesis of closed-loop linkages that match the specific movement of an individual and is demonstrated in the design and evaluation of a mechanical thumb, a hands-free crutch and a knee-ankle-foot orthosis.

The mechanical thumb was designed using motion capture data of a thumb curling task. A geometric model of the resulting four-bar linkage moved smoothly between the task positions and matched the desired thumb tip physiological movement. Then, a hands-free crutch was designed with a four-bar linkage synthesized to match motion capture data defining the movement of an individual's knee joint during walking. Tests of a prototype demonstrated reduced hip-hiking and increased stride length compared to a fixed-knee hands-free crutch.

A six-bar knee-ankle-foot orthosis was designed to match both the angular movements at the knee and ankle joints and the metatarsal trajectory obtained from motion capture data of a natural walking gait in the sagittal plane. Tests of a prototype showed normal knee function and stride lengths during walking. Optimization was combined with the kinematic synthesis procedure to match the metatarsal trajectory.

The result is a new design procedure to obtain simple and robust wearable devices for application as hand, knee, and knee-ankle-foot orthoses that match natural human movement kinematics.

# Chapter 1

## Introduction

### 1.1 Overview of Orthotic Devices

An orthosis is defined as an externally applied assistive device, that is designed and fitted to the body of a user, to increase their independence in daily living. Their functions can include one or more of the following: control of biomechanical alignment of the body, limit joint Range of Motions (ROM) to support recovery after an injury, prevent further injury, reduce pain, assist rehabilitation [1].

Orthoses are classified as exoskeleton type or end-effector type [2] based on whether it supports the movement of the joints it spans, or if it connects to the distal end of the limb segment, respectively, in this work as shown in Figure. 1.1. Each of these type of devices can then be further categorized into lower extremity (hip, knee, ankle, and foot) or upper extremity (shoulder, elbow, wrist, fingers and thumb).

They are used by individuals with a needs ranging from ranging from preventive care, recovery from ligament injuries, post-operative rehabilitation, to support and management of

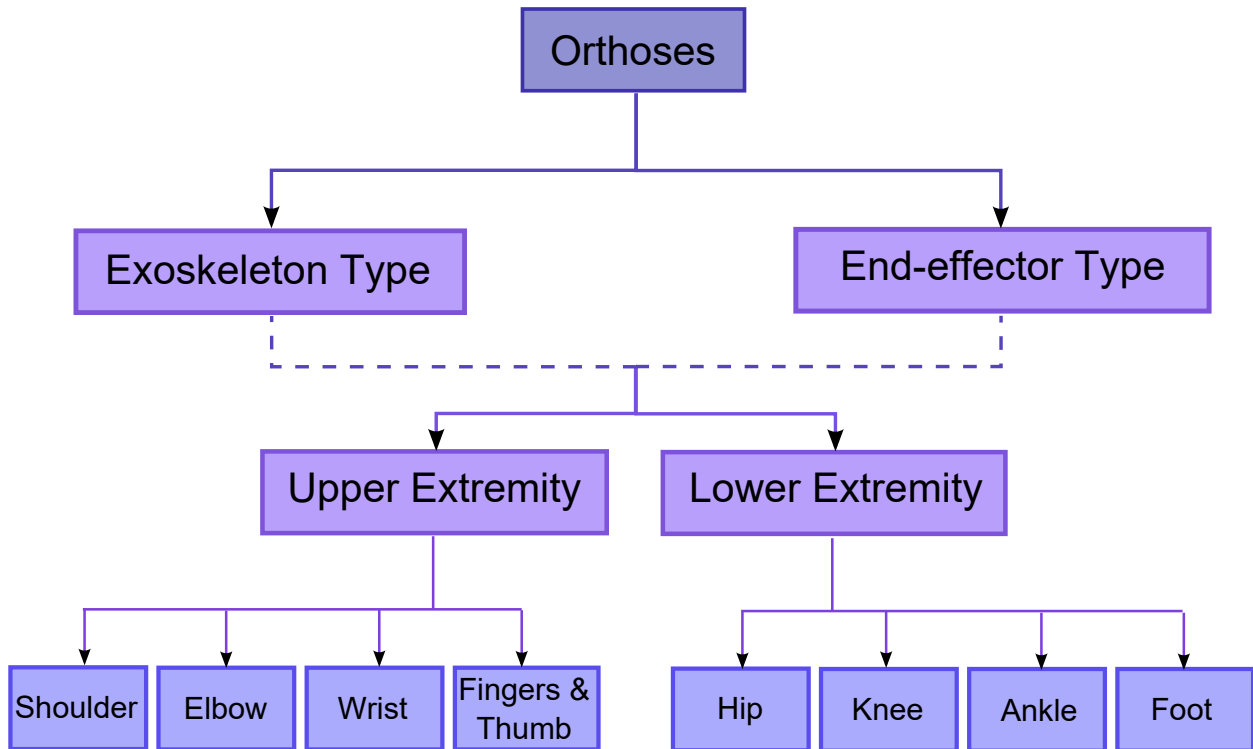


Figure 1.1: Classification of orthoses based on modality of providing assistance.

chronic or degenerative conditions among others. The global orthopedic devices market is predicted to grow by 4.35% - 5.5 % annually between 2016 - 2022, be valued at USD 1.33 billion [3, 4, 5].

Supported by a growing demand, the design of assistive devices for both fingers and lower-leg is an active area of research, and many different design philosophies and strategies are currently being explored for the design of finger and thumb assistive devices [6], and knee-ankle-foot orthoses [7].

## 1.2 Finger Orthoses

Assistive devices for the hand and fingers are designed to help individuals with disabilities perform activities of daily living such as grasping, or to perform simple rehabilitative exercises

such as finger and thumb curling [8]. While the human hand is a very complex, with many degrees of freedom (DOFs) of motion and a relatively small size, the kinematics of the individual fingers during object grasping tasks or typical therapeutic exercises can be simplified to motions such as flexion-extension and abduction-adduction. This suggests that single DOF finger assistive devices can be developed to address targeted needs.

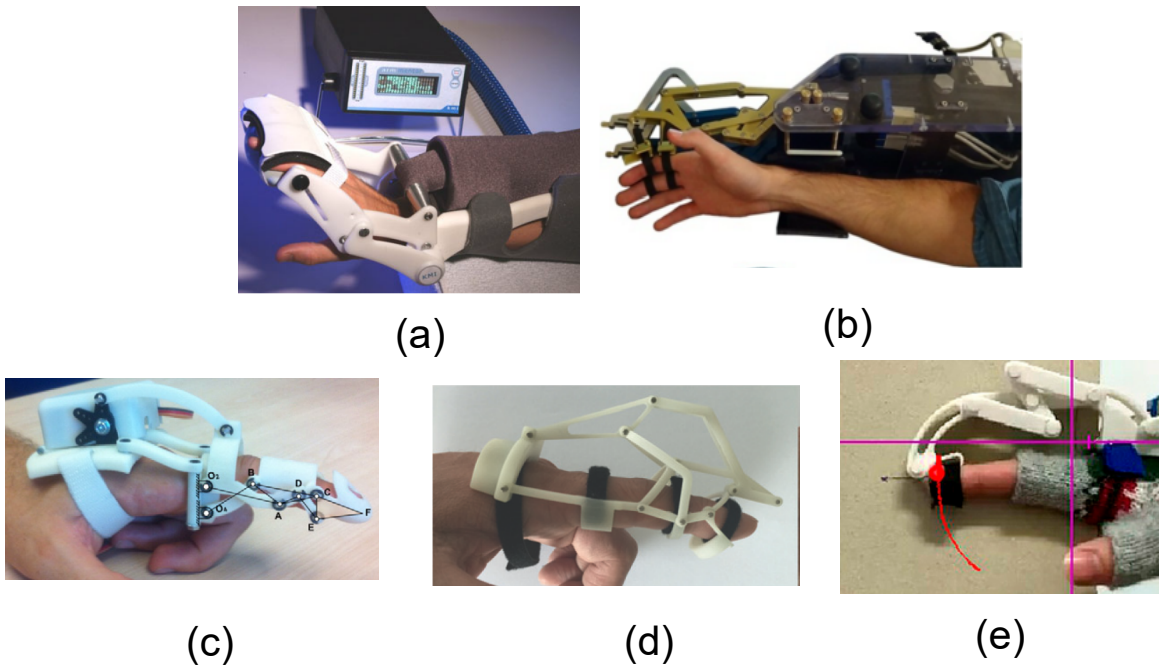


Figure 1.2: Previously developed hand/finger rehabilitation devices. (a) The mentor [9], (b) FINGER curling robot [10], (c) Single DOF finger exoskeleton [11], (d) Robotic finger exoskeleton with slider mechanism [12].

Hand and finger assistive devices (that do not encompass the thumb) based on planar linkages include the Mentor (Kinetic Muscles Inc., Tempe, AZ), shown in Figure. 1.2(a), a commercially available pneumatic muscle driven hand therapy device, that utilizes a modified Watt linkage to provide extension and flexion movement at the wrist and fingers [9]. It is an end-effector type device.

The following devices are considered to be exoskeleton-type. The Hand Spring Operated Movement Enhancer (HandSOME), is a passive lightweight wearable exoskeleton with a four-bar linkage and elastic elements designed to provide an assistive torque profile for finger

flexion [13]. Finger INdividuating Grasp Exercise Robot (FINGER) (Figure. 1.2(b)) is a finger curling robot that can individually assist both index and middle fingers through a natural grasping motion guided by an eight-bar mechanism that controls the orientation and position of the proximal phalanx and the position of the middle phalanx [10]. Bataller et al. use an evolutionary algorithm based optimization process to design a Stephenson III six-bar finger exoskeleton (Figure. 1.2(c)) that can trace a specified fingertip trajectory [11]. Robson and Soh presented a wearable eight-bar index finger device (Figure. 1.2(d)), designed using position, velocity and acceleration constraints on the fingertip trajectory [14]. Hsu et al. proposed a slider mechanism to ensure the robotic finger exoskeleton (shown in Figure. 1.2(e)) consisting of an N-shaped linkage follows human finger motion, and to reduce the size of the device [12].

In particular, several exoskeletons and end-effector type devices have been developed for thumb assistance. Agarwal et al. [2] review sixteen devices that actuate the thumb for a variety of purposes, of which six thumb designs are described by the authors to be primarily linkage-based and actuated with a locally situated motor, which include a haptic exoskeleton presented by Fontana et al. [15], thumb exoskeleton for hand rehabilitation by Lambercy et al. [16], and an under-actuated hand exoskeleton by Garcia-Hernandez et al. [17].

Zheng and Li presented the design of an exoskeleton-type hand rehabilitation device for the index finger and thumb (Figure. 1.3(a)). Each finger consists of an open 3R chain combined with a four-bar linkage at each phalange [18]. The Hand Exoskeleton Rehabilitation Robot (HEXORR) is an exoskeleton that uses a four-bar linkage that minimizes the force required by the fingertips to move the linkage through its Range Of Motion (ROM) to actuate the fingers and the thumb [8]. The linkage is synthesized by graphically changing the pivot positions of the linkage for three specified task positions, and then utilizing custom optimization routines to obtain a satisfactory design. The 18-DOF hand-assist robot by Ueki et al. [19], consists of four finger mechanisms, a wrist mechanism and a 3 DOF thumb motion assist

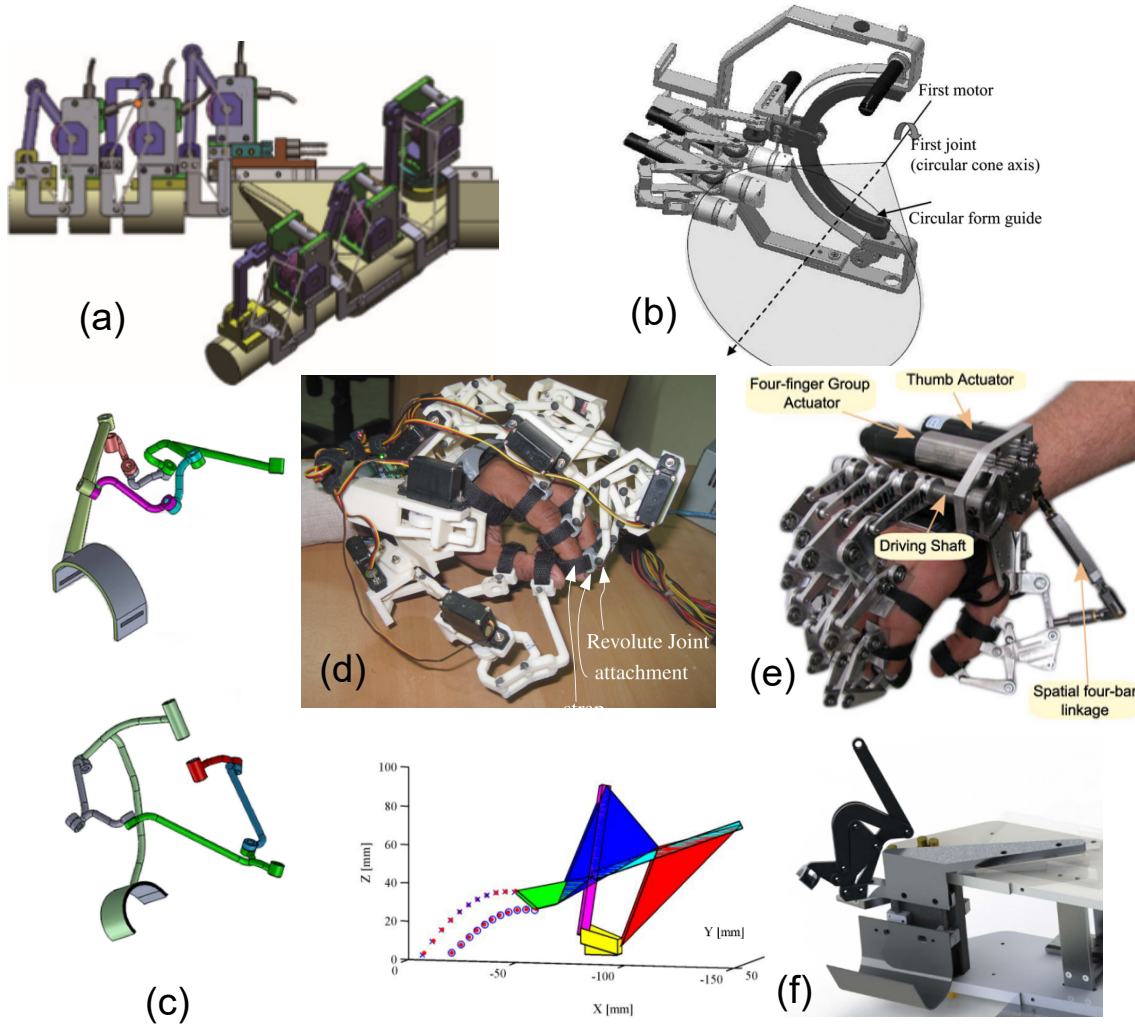


Figure 1.3: Previously developed hand devices including the thumb. (a) Index and thumb rehabilitation device [18], (b) A 3 DOF thumb motion assist mechanism [19], (c) Two spatial CRR-RRR thumb guidance mechanisms [20], (d) Three fingered hand exoskeleton [21], (e) The BRAVO active hand orthosis [22], (f) A Watt I six-bar thumb curling exoskeleton [23].

mechanism designed to provide the required movable ROM at the joints and maximum joint torques. The mechanism forms three closed loops with the human thumb by means of fixtures attached to the phalanges. Yihun et al. [20] presented the design of two spatial CRR-RRR mechanisms for thumb guidance using motion capture data consisting of C-cylindrical and R-revolute joints. Nishad et al. [21] presented a three finger hand exoskeleton (Figure. 1.2(e)) consisting of nine planar four-bar linkages, three for each finger exoskeleton, concatenated serially that are optimally designed to follow the motion of all the phalanges of the index

and middle finger. The thumb of the hand exoskeleton consists of three four-bar linkages. The four-bar controlling the movement of the fingertip relative to the thumb CMC joint is out of the plane with respect to the other two four-bars that control the motion of the MCP and IP joints. For flexion-extension movements, the thumb is actuated only by the first linkage which guides the sub-assembly of the other two linkages that are locked to maintain the digit in the state of desired flexion. For adduction-abduction movements, the second linkage guides the MCP joint and the third four-bar guides the IP joint, while the first linkage is locked to keep the other two linkages on the sagittal plane of thumb. The BRAVO active hand orthosis has two independent DOF, one for fingers and one for thumb, to provide assistance in grasping of cylindrical objects [22]. The thumb mechanism actuates the flexion/extension movements of the two distal phalanges only. The position and the plane of motion of the thumb is adjustable through a passive six DOF serial mechanism and a spatial four-bar linkage connecting the thumb links and the actuator shaft. Wolbrecht et al. [23] presented an initial prototype of a thumb curling exoskeleton as an add-on to the FINGER (robot). The thumb mechanism consists of a Watt I six-bar linkage that guides the position and orientation of the proximal phalanx of the thumb through a single DOF naturalistic grasping motion defined using motion capture data.

All the devices presented above are exoskeleton-type, with the exception of the design presented by Yihun et al. [20], which provides end-effector guidance.

Of the thumb designs proposed, barring a few instances the design and development process for the mechanism is not described. Also, the designs presented, including single DOF mechanisms, are fairly complicated with many moving parts. Thus, the open problem is to find a design formulation that can fulfill design requirements within a rational procedure. For thumb assistive device, size, weight and safety are of primary consideration. As seen in existing designs, passive planar mechanisms, with their multiple varieties of single DOF configurations, provide an adequate solution base for this design problem.

### 1.3 Lower-leg Assistive Devices: Knee-Ankle-Foot Orthosis (KAFO)

In general, the gait rehabilitation process towards regaining meaningful mobility can be classified into two stages: (1) restoration of gait and, (2) improvement of gait in order to meet the requirements of daily living [24].

The first stage, restoration of gait, has seen major strides since the 1980s with the introduction of robotic devices to support task-specific repetitive gait training. Stationary gait rehabilitation machines such as the driven gait orthosis Lokomat (Hacoma, Switzerland) [25], Ambulation-assisting Robotic Tool for Human Rehabilitation (ARTHuR) [26], Lower extremity Powered ExoSkeleton (LOPES) [27] and an unilateral active orthoses called Active Leg EXoskeleton (ALEX) [28] include treadmill devices, supportive frameworks and a robotic orthosis to assist patients as shown in Figure. 1.4. Such devices relieve the physical demands on physiotherapists as the mechanical framework supports the patient, and help provide repeatable, and measurable assistance [29].

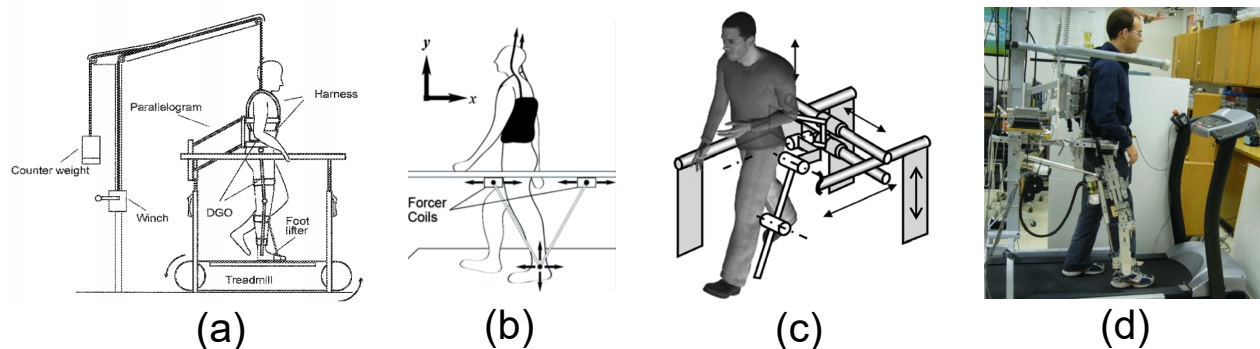


Figure 1.4: Stationary gait rehabilitation machines. (a) Schematic of driven gait orthosis, Lokomat [30]. (b) Schematic of ARTHuR [26]. (c) Schematic of LOPES [27]. (d) Active orthoses ALEX [28].

Passive stationary gait rehabilitation machines have also been designed to provide inexpensive and robust alternatives for patients outside clinical settings. Use of mechanisms

to achieve desired movement leads to a reduction in the number of DOF of the device, which simplifies the control design required. Some examples include a four-bar crank-rocker mechanism to obtain desired ankle trajectory presented by Ji et al. [31], a 1 DOF ten-bar mechanism to trace the trajectory of the toe presented by Tsuge et al. [32], and a cam-linkage mechanism presented by Shao et al. [33] as shown in Figure. 1.5.

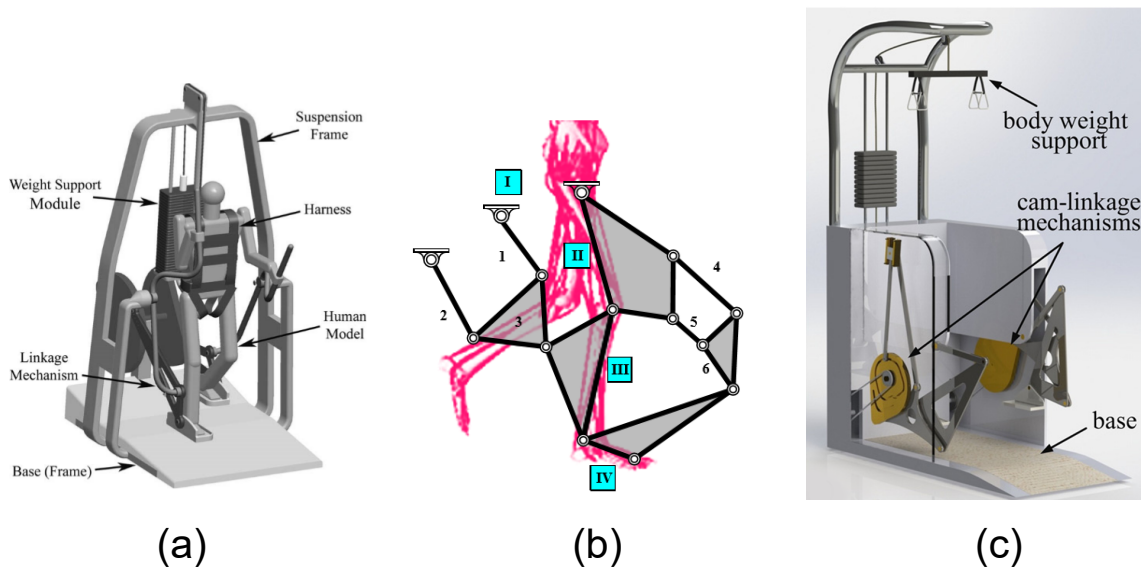


Figure 1.5: Passive stationary gait rehabilitation machines. (a) A Gait Rehabilitation system using a four-bar mechanism [31]. (b) A ten-bar mechanism to guide gait [32]. (c) A cam-linkage mechanism rehabilitation robot [33].

In addition to the rehabilitation efforts, lower-limb orthotics are prescribed once the patient's general condition has stabilized and they are able to stand or engage in walking training, particularly in cases of lingering instability at the knee and ankle joints [34]. Some mobile lower-limb devices include a supportive framework with wheels, such as a Stephenson II six-bar mechanism active gait trainer (shown in Figure. 1.6 (a)) designed by Wang et al. [35]. Another class of devices that are often used to support and improve walking include orthoses that have potential to be used as daily-wear devices. The passive orthosis proposed by Berkelman et al. [36], which aims to mitigate toe drop using a four-bar linkage (shown in Figure. 1.6 (b)), a passive leg orthosis developed at University of Delaware (shown in Figure. 1.6 (c)) [37] are some examples of gait rehabilitation machines that make use of kinematic

programming to couple the motion between the joints of the leg to achieve their task.

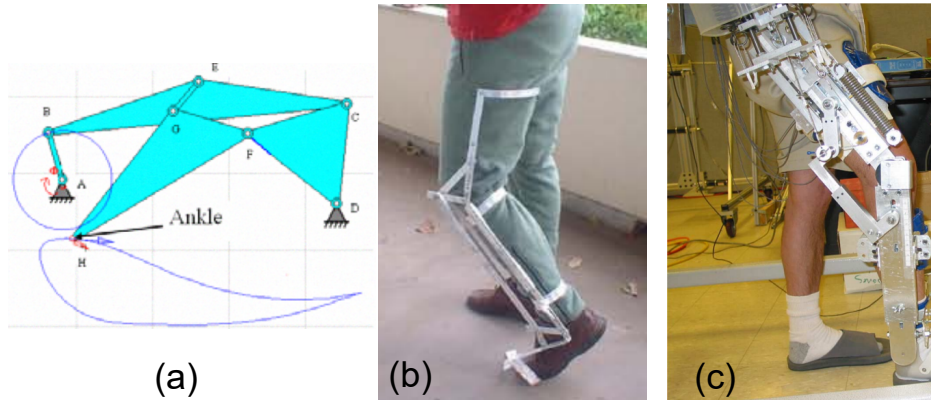


Figure 1.6: Gait trainers. (a) The Stephenson II six-bar linkage used in a wheeled gait trainer [35]. (b) A single DOF passive orthosis [36]. (c) A gravity balancing passive orthosis [37].

Lower extremity orthoses which extend over the knee, ankle, and foot - called Knee-Ankle-Foot-Orthosis (KAFO) have been reported to be prescribed to patients with knee instability due to neuromuscular disorders and central nervous system conditions up to 74.75% of the time to assist with joint stability [38]. They are further classified into different types based on the orthotic knee joint design, locking and unlocking mechanism, etc. An example of a KAFO device is shown in Figure. 1.7. These are exclusively exoskeleton-type devices.

### 1.3.1 Locked Knee KAFOs

KAFOs with a locked knee (as shown in Figure. 1.8) constrain the motion at the knee joint in a fully extended position to provide stability during walking in both stance and swing phases [7]. They are commonly prescribed for assisting diminished function at the knee joint, for for example in children with Arthrogryposis, which is a rare disorder characterized by the presence of multiple joint contractures in multiple body areas that are present at birth, with a reported incidence from 1 per 3,000 to 1 per 5,100 live births [40].

Some commonly used knee-locks are: (a) Drop lock - locks at full extension or unlocks to



Figure 1.7: An example of a commercially available KAFO device [39].



Figure 1.8: An example of a KAFO with locked knee joint and carbon fiber spring ankle joint [40].

allow full flexion, (b) Bail lock - a spring-loaded joint that locks automatically as the leg reaches full extension, and can be unlocked by reaching back and pulling a metal loop in the back, (c) Ratchet lock - incremental locking mechanism every  $710^\circ$ , (d) Offset knee - a posterior offset axis at the knee to allow inherent stability from  $0^\circ$  to  $30^\circ$  and (e) Trick knee - allows up to 25 of flexion in its locked position [41].

However, as a locked-knee device does not allow flexion-extension motion at the knee during walking, users typically adopt abnormal gait patterns, including circumduction, hip hiking and/or vaulting and excessive trunk and pelvic movements. These gait compensations lead to premature exhaustion during ambulation due to increased energy expenditure levels, as well as limited mobility, pain due to soft tissue injuries, and a decreased ROM in knee and ankle joints, resulting in high rates of KAFO disuse (in excess of 60%) [42].

### **1.3.2 Stance Control KAFOs (SC-KAFOs)**

A new generation of KAFOs, namely, Stance Control KAFOs (SC-KAFOs) were introduced in 1978 [43]. These devices enable free knee flexion during the swing phase, resulting in a more normal gait pattern compared to locked-knee KAFOs. The knee joint is locked during the stance phase to provide stability for weight bearing by activating a lock or brake, which is then deactivated during the swing-phase.

The mechanisms of stance control reported in literature either have a mechanical (passive) or electronically controlled (externally powered) knee joint. Commercially available SC-KAFOs like the Otto Bock Free Walk, Becker UTX, and Full Stride/ Safety Stride are activated through joint ROMs, as shown in Figure. 1.9. The Free Walk and UTX have a spring-loaded pawl that locks the knee automatically the end of swing phase, as the knee reaches full extension prior to heel strike, and unlocks it at the beginning of the swing phase characterized by a  $10^\circ$  ankle dorsiflexion angle by pulling a control cable connected to the pawl.

For SC-KAFOs such as the Horton stance control knee joint, the Fillauer Swing Phase Lock (Figure. 1.10), and the Sensor Walk from Otto Bock, locking/unlocking mechanism depends on the relative position of the thigh or the hip angle. The Horton Stance Control Orthosis locks and unlocks the knee through the relative positioning of a cam against a friction ring.

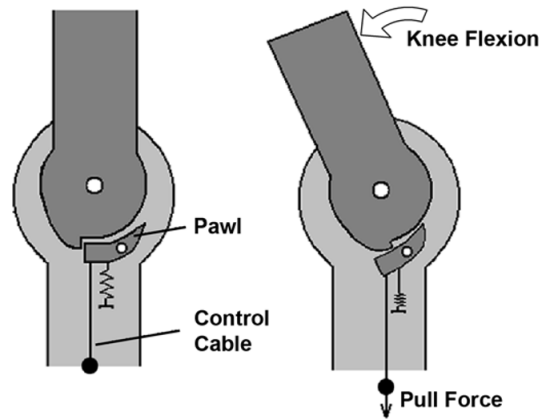


Figure 1.9: Joint ROM controlled SC-KAFO. Locking and unlocking mechanism of the Ottobock Free Walk and Becker UTX [44].

Fillauer uses a gravity actuated weighted pawl as a knee joint locking system. At heel strike, the knee joint is locked in full extension as the pawl falls into the locking position. As the thigh moves behind the trunk, the knee is set free as the pawl disengages. In these devices the locking/unlocking mechanism depends on the hip angle.

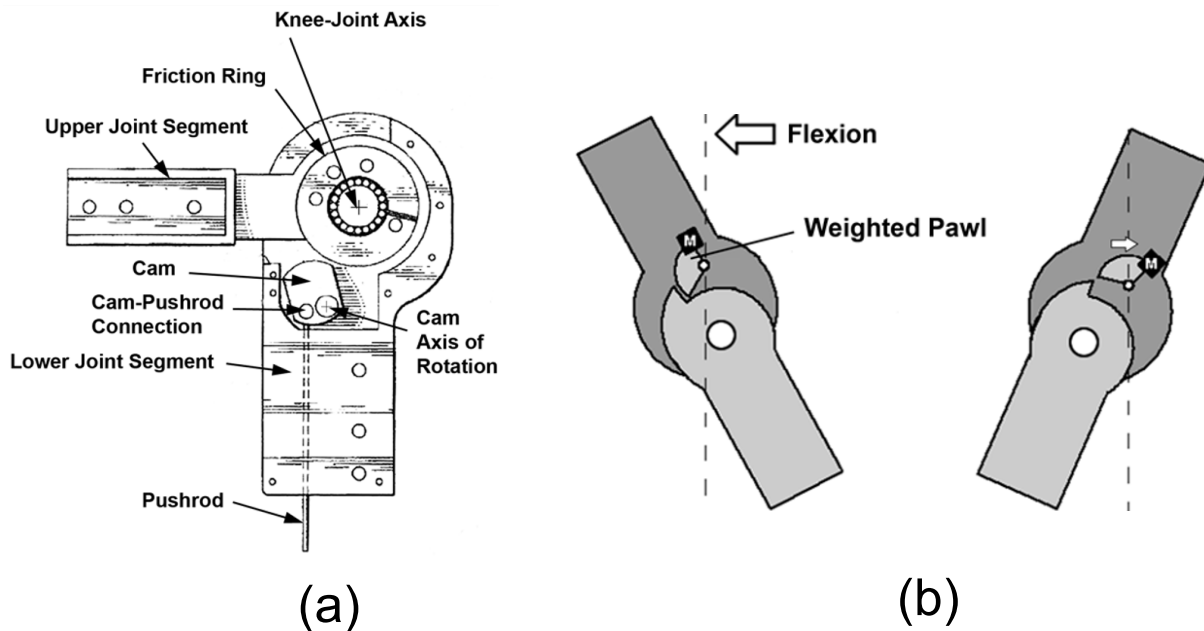


Figure 1.10: (a) The Horton Stance Control Knee and (b) the Fillauer Swing Phase Lock [44].

In the 9001 E-Knee from Becker Orthopedics, E-MAG Active from Otto Bock and SPL, the control of knee joint is position sensor activated as shown in Figure. 1.11. The knee joint

on the Becker Orthopedic 9001 E-Knee brace includes a magnetically activated one-way dog clutch. The electromagnetic system includes two circular ratchet plates, a coil, a tension spring, a foot switch, and a battery pack. During the stance phase, the foot switch causes the ratchet plates to engage by coming together. Only extension is allowed in this period. During the swing phase, the ratchet plates are disengaged as the spring recoils, allowing free rotation.

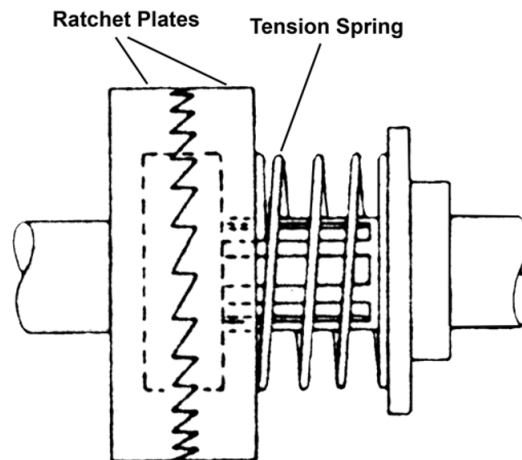


Figure 1.11: Becker Orthopedic 9001 E-Knee [44].

Studies comparing SC-KAFOs with locked knee KAFOs show that SC-KAFOs have an increased acceptance rate, and report some improvements in gait kinematics such as increased walking speed and reduction in compensatory gait deviations. However, improvements observed in hip and pelvic motions, walking speed and energy expenditure were small and were not observed consistently in all studies [45, 44, 7, 42]. Additionally, these devices can only be used if the individual has sufficient hip strength. Finally, current commercial SC-KAFOs are often noisy, bulky, heavy, and expensive, restricting their widespread usage.

### 1.3.3 Active KAFOs

Mechanically active or powered KAFOs control the knee joint both during stance and swing phases by applying external torque throughout the whole gait cycle [7]. These devices

typically subdivide gait into discrete states, and based on the current state of the device the actuators follow specific strategies. For example, the Ottobock C-Brace (shown in Figure 1.12) offers microcontroller regulated extension and flexion dampening of the hydraulic knee joint with the help of servomotors and a planetary gear set in order to provide real-time control of stance knee flexion, knee flexion during weight bearing, and dynamic control of the swing phase [43].



Figure 1.12: The Ottobock C-Brace.

Active KAFOs present safety issues due to their high impedance, and their use is limited to rehabilitation devices in lab environments [46]. Additionally, powered KAFO usage was not found to significantly improve any of primary gait measures for poliomyelitis subjects. [47]

Issues regarding unsatisfactory performance, bulkiness and complexity are some of the major reasons for underutilization and abandonment of orthotic devices [48]. This creates a crucial health care need as orthotic devices prescribed for knee instability play an important role in maintaining and enhancing participation in activities of daily living, and promote physical and psychological well-being [49].

While there is a paucity of high-quality literature on the effectiveness and comparative utility of various orthotic devices proposed for knee instability, in general, SC-KAFOs provide

improved functionality compared to locked-knee KAFOs for people who have sufficient hip/thigh strength to operate them. However their use has been found to result in lower walking speeds, which might be attributed to an increase in the the concentration required for their operation and control. Additionally, vaulting of the contra lateral leg over the braced leg remains a concern with SC-KAFOs in the stance phase, along with a lack smooth switching between stance and swing modes.

Based on the above discussion, there is a need to develop passive KAFOs that can provide normal knee motion for the user during the entire gait cycle - i.e. controlled flexion during stance, knee-extension assistance and smooth switching between stance and swing modes. More efficient devices can be designed by exploiting the dynamics of human walking and the leg morphology. The cyclic nature of closed-loop gait trajectory can be suitably addressed through deployment of linkage-mechanisms, which automatically constrain the ROM of the joints. Since the coordination of joint motion and limitation of joint ranges are achieved simultaneously, utilizing linkages should result in safe and reliable KAFO designs.

### **1.3.4 Multi-axis Knees**

The separate category of knee joints, called polycentric or multi-axis knees are usually designed to replicate the ICR of the anatomical knee joint. Polycentric knee joints with gears or cam-follower type mechanisms have been presented by Foster and Milani [50], Walker et al. [51] and Townsend and Knecht [52]. Of multi-axis knee composed of linkage-based mechanisms, four-bar knees are most common, as they are similar in structure to the human knee joint in the sagittal plane. Four-bar knee designs have been utilized extensively in the design of transfemoral prosthesis, and Radcliffe [53] documented the kinematic characteristics and advantages of such knee mechanisms. An analysis of the strengths and weaknesses of four-bar linkage knee mechanisms for clinicians prescribing prosthetics was given by de

Vries [54].

For the design of knee braces, Townsend and Williams [55] patented a design consisting for a pair of four bar mechanisms placed on the lateral and medial sides of the human knee that are designed to constrain the motion of the calf with respect to the thigh. Bertomeu et al. [56] present a knee design based on a crossed four-bar linkage mechanism which has been designed to optimally follow a motion curve representing the knee kinematics in the position at which the knee hinge should be placed. The design of a crossed four-bar knee mechanism for a KAFO device was presented by Bapat and Sujatha [57], that is optimally synthesized using genetic algorithms to mimic the ICR of the human knee.

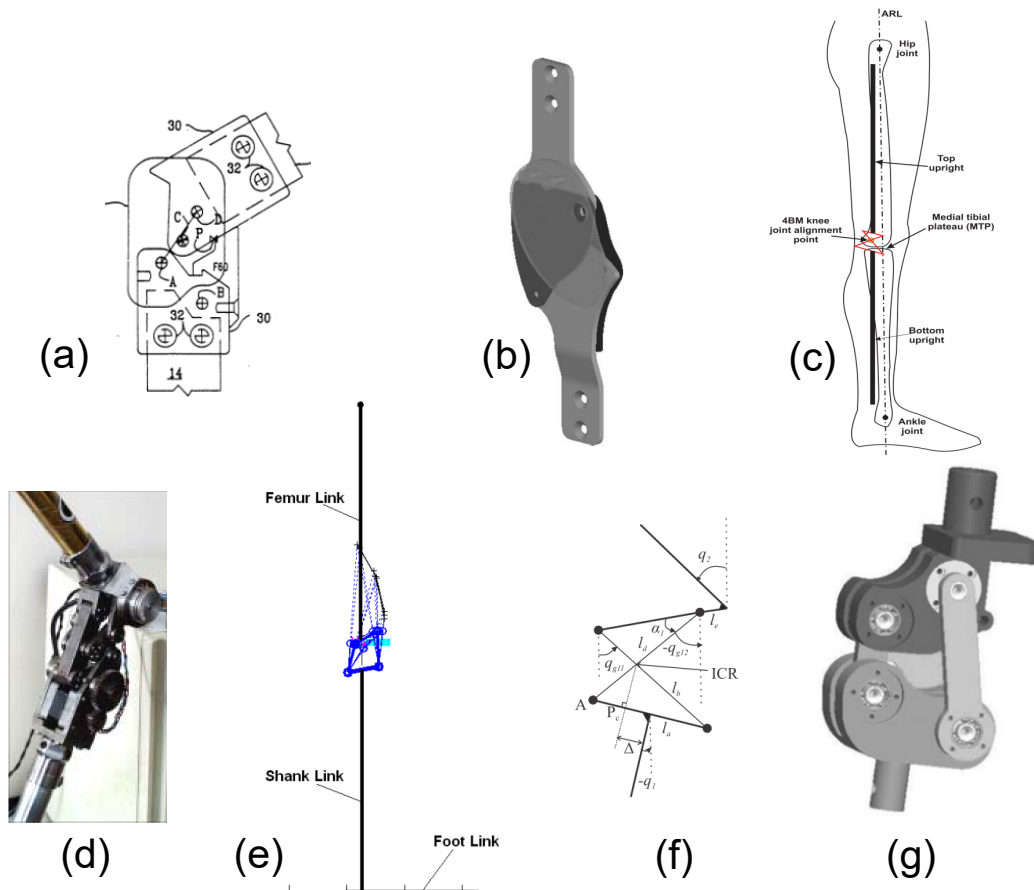


Figure 1.13: Multi-axis knee mechanisms. (a) Knee brace design with four-bars [55], (b) & (c) Crossed four-bar knee joint for orthoses [56, 57], (d) Six-bar prosthetic knee mechanism [58], (e) Four-bar prosthetic knee joint [59], (f) Crossed four-bar prosthetic knee mechanism [60], (g) Four-bar knee mechanism controlled by MR damper [61].

Other examples of linkage-based multi-axis knee joints have been reported for prosthetic design, where four and six-bar linkages are synthesized for specified ICR trajectory. For example, Jin et al. [58] investigated the kinematics and dynamics of a six-bar knee mechanism, and presented the prototype of an experimentally developed knee joint that is optimized to meet the requirements imposed on its ICR and to ensure stability in full extension. Sancisi et al. [59] presented an optimization procedure for the synthesis of a four-bar linkage for knee prosthesis based on a reference motion and patient-specific constraints on its ICR. Hamon and Aoustin [60] propose a crossed four-bar linkage designed to have an optimal energetic trajectory. Xie et al. [61] presented a prototype of a four-bar knee mechanism designed to mimic the ICR of the human knee and controlled by a magneto-rheological damper for intelligent bionic legs.

These devices can be considered to be a hybrid of the exoskeleton and end-effector type devices, as they guide the motion of the knee joint, however the device axes do not coincide with the anatomical human joint axes.

## 1.4 Motion Analysis

Traditional techniques for kinematic synthesis of planar mechanism tend to focus on three approaches: trial and error, graphical and algebraic synthesis. Using trial and error, motion of a mechanism can be generated by adjusting its parameters. However, this approach is not repeatable and it can be difficult to generate different solutions.

In this work, algebraic synthesis techniques are used to propose systematic procedures for generating anthropometric planar one DOF linkages for anthropomorphic tasks. Designing effective wearable and anthropomorphic mechanisms using algebraic techniques requires an understanding and quantitative study normal human movement patterns. The physiological

translational and rotational motions of the body segments serve as the source for kinematic design of linkages to mimic such motion.

### **1.4.1 Optical Motion Capture**

Typically, human motion data is obtained experimentally using computer-aided video motion capture systems with infrared cameras, and consist of accurate three-dimensional spatial positions of reflective markers placed on key anatomical sites [62]. The spatial position coordinates for each reflective marker is expressed with respect to capture volume's origin and axes that is set by the user during calibration.

For the work presented in this text the motion analysis was performed using a computer-aided video motion analysis system with seven infrared cameras (Qualisys Oqus500) under the control of a computer (HP ENVY Phoenix 810-160 with NVIDIA GeForce GT 640 graphics card running Qualisys OptiTrack 4.2) at the Human Interactive Robotics Laboratory at California State University, Fullerton.

### **1.4.2 Motion Capture of Human Thumb**

The opposable thumb is one of the distinguishing features of a human hand, and it allows us to perform precision pinching and grasping. Its motion is a result of a complex arrangement of bones, muscles and tendons in the human hand, and is critical to hand function for nearly all of the basic activities of daily living [63]. This subsection describes motion capture and data analysis used to characterize the thumb curling action for a healthy human subject. Reflective markers were attached to the thumb, index and middle fingers of the subject, and the grasping action was recorded using four IR cameras. The experimental set up used for hand motion capture is shown in Figure. 1.14. The global fixed frame was set on the surface

of the table, with x-axis pointing to the right, and y-axis points to the front the room.



Figure 1.14: The experimental setup showing the capture space and four of the seven Qualisys *OQUS500+* cameras used for motion capture of hand movement.

The thumb consists of the proximal and the distal phalanges, which are treated as rigid bodies, and its motion is entirely described by the position-time information for the markers placed at the thumb MCP joint, IP joint and the thumb tip as shown in Figure. 1.21.

### **Kinematic Model of the Human Thumb and Motion Analysis**

The flexion-extension of the thumb as it curls can be described in terms of the rotational motion of the Metacarpophalangeal (MCP) and Interphalangeal (IP) joints along their biological joint axes as shown in Figure. 1.16. The MCP joint of each finger links the metacarpal bone to the proximal phalanx, and have two DOF, which permit flexion - extension, abduction -adduction movements. The proximal phalanx and the distal phalanx are lined by the IP joint at the thumb. It is a one DOF joint, and are usually modeled as having as

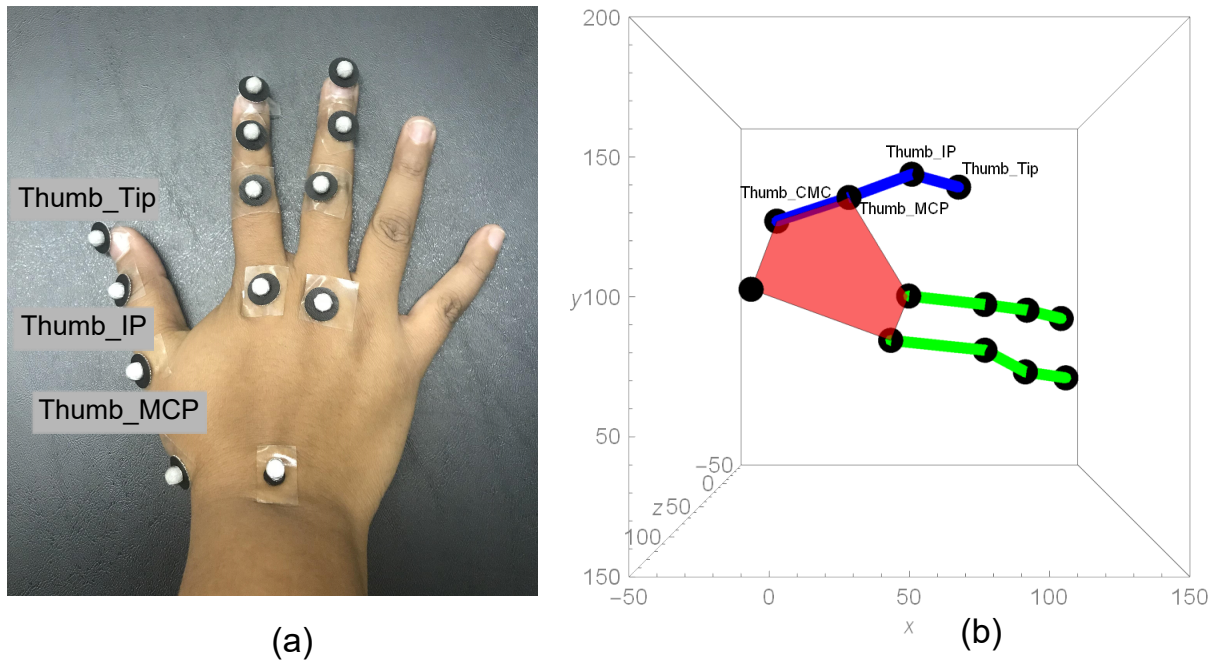


Figure 1.15: (a) Marker placement locations of the hand to study grasping motion. (b) Motion Capture still displaying the thumb capture data.

having a single axis of rotation.

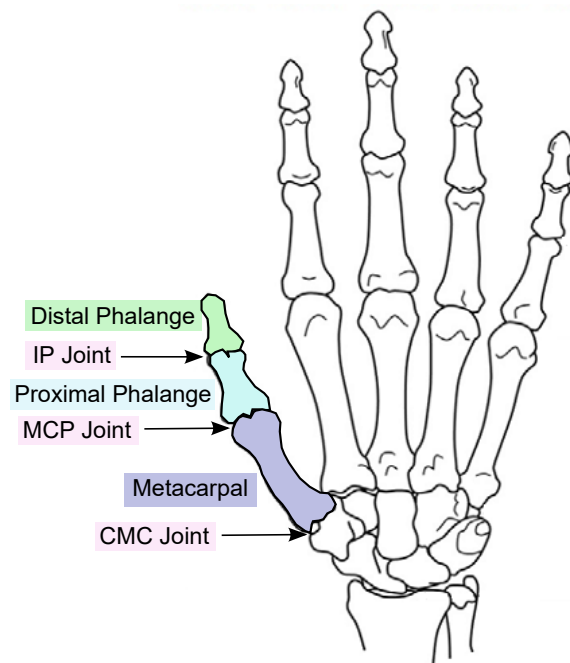


Figure 1.16: The anatomy of the human hand [64].

To study only the flexion-extension motion of the thumb in a plane, its kinematic structure

can be simplified and modeled as a 2R serial chain as shown in Figure. 1.17. The IP and MCP joints are modeled as one DOF revolute joints. As this model ignores the abduction-adduction motion of the thumb, during the experimental data collection of the curling motion of the thumb care is taken to ensure that the out of plane motions are kept to a minimum and are not significant.

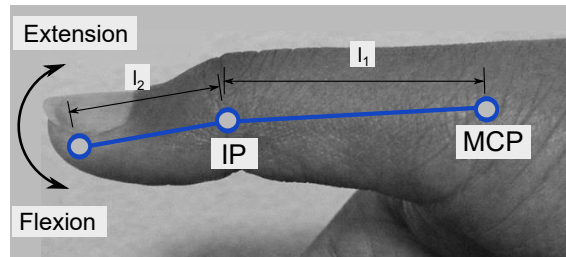


Figure 1.17: Kinematic model of the thumb in XZ plane.

From the positional data of the markers, the relative angular rotation of the individual finger phalanges are isolated using the simplified kinematic model of the thumb. A closing movement of a human thumb can be obtained by either actuating the two revolute joints separately. However, it is clear from the motion analysis that the rotational motion of the two revolute joints are not independent, consequently, a very good approximation of human thumb motion could be obtained by a single DOF closed-loop kinematic chain. By constraining the 2R chain of the thumb with another RR constraint, we synthesize thumb mechanisms composed of four-bar linkages.

### 1.4.3 Motion Capture of Lower-leg

For gait analysis, we obtain 3d data of a healthy person walking on a treadmill. The experimental set up used for gait experiments is shown in Figure. 1.18.

The global fixed reference frame is defined by calibrating the system with a L-frame (shown in Figure. ??(a)) placed on the treadmill's surface, such that the X-axis points to the



Figure 1.18: Experimental set up for motion capture data collection for locomotion.

left, the Y-axis points out of the plane of the paper, and thus, the Z-axis of the right-handed coordinate system points upwards as it is perpendicular to both these axes. Marker placement to capture lower-leg motion during walking is shown in Figure ?? (b).

### **Kinematic Model of the Human Knee Joint and Motion Analysis**

The complexity of the knee joint makes understanding its structure and kinematics a key component in the design of knee orthoses. It is one of the largest joints in the human body and it supports fundamental body movements. Its movement is the result of interactions among bones, ligaments, cartilage and muscles, and has been completely described by six DOF. Due to the knee's complexity, the mechanism theory is gradually used to simplify and simulate the joint motion. OConnor [65] proposed a planar fourbar linkage in sagittal plane as shown in Figure. 1.20. It had significant value in analyzing the knee motion and

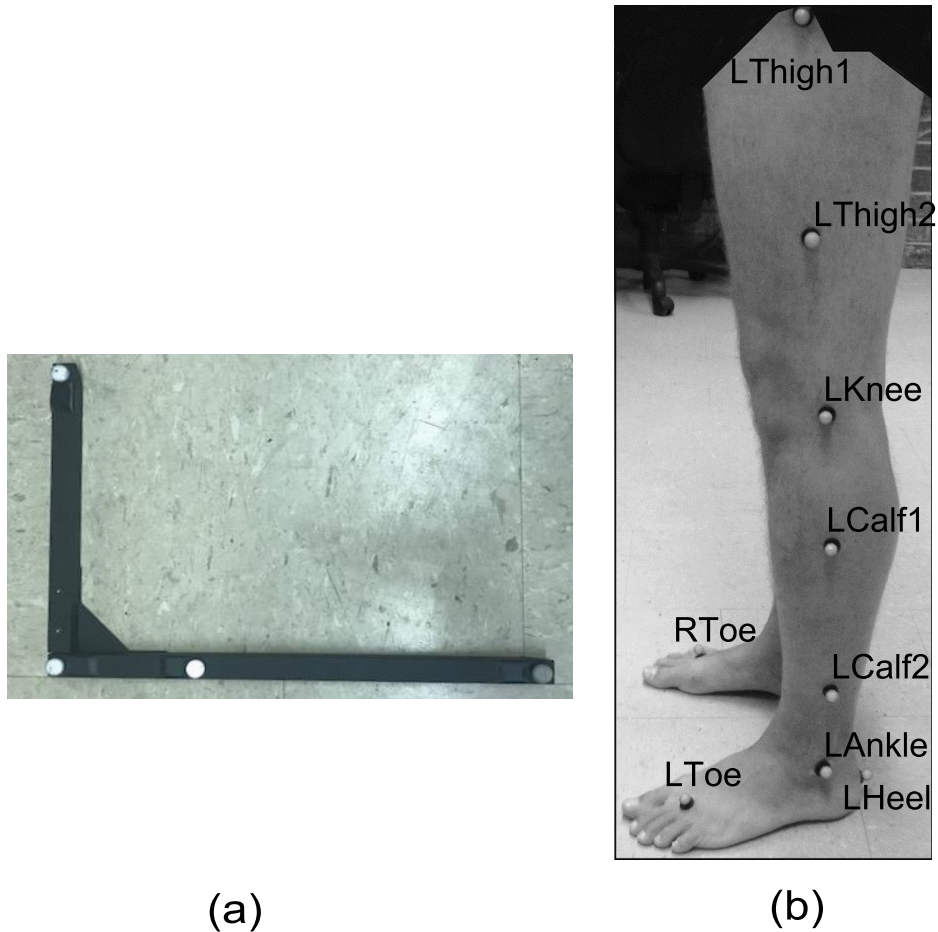


Figure 1.19: (a) The L-frame placed on the capture space's floor to set the capture volume's origin and axes. (b) Marker placement locations of the lower leg to study normal walking.

the interaction forces between the ligament and muscle, and also developing a machine to restore knee functions. The simplest knee joints consist of an external hinge joint, placed at a manually approximated location of the knee joint's center of rotation. This technique is not accurate and the approximation in enforcing an articular joint to an unnatural mechanical behavior may lead to unwanted results in post-traumatic knee kinematics. Other researchers have proposed more accurate kinematic models of the knee. Under suitable assumptions, and for specific motions, the three-dimensional motion at the knee joint can be approximated as a single DOF mechanism [66].

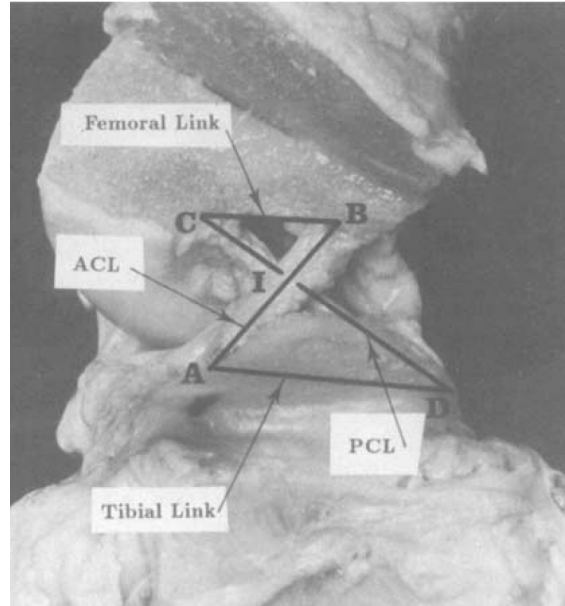


Figure 1.20: The geometry of the knee joint in the sagittal plane [65].

### Lower-leg Motion Analysis

From the positional data of the markers, the relative angular rotation of the individual body segments are derived using analytical techniques based on their simplified kinematic models. Human body segments are treated as rigid bodies, and sites for marker placement are chosen to minimize relative motion between the skin and underlying bony structures (as illustrated in Figure 1.21 (a)), as well as to facilitate the definition of local/relative coordinate systems for each of the body segments.

We record the normal gait of a young adult male subject walking on a treadmill at a self-selected speed of 1.2 m/s. Normal walking speed for healthy adults is reported to be  $1.4 \pm 0.2$  m/s [67]. Slower walking speeds can result in decreased flexion at the hip and knee during the swing phase, which is commonly seen in patients with neurological gait deficits [68].

As the kinematics of human walking are cyclic in nature, we can study its characteristics over the duration of a cycle. A complete gait cycle is defined as the portion between two successive contacts of the heel of the leg under consideration with the floor. Based on this, the

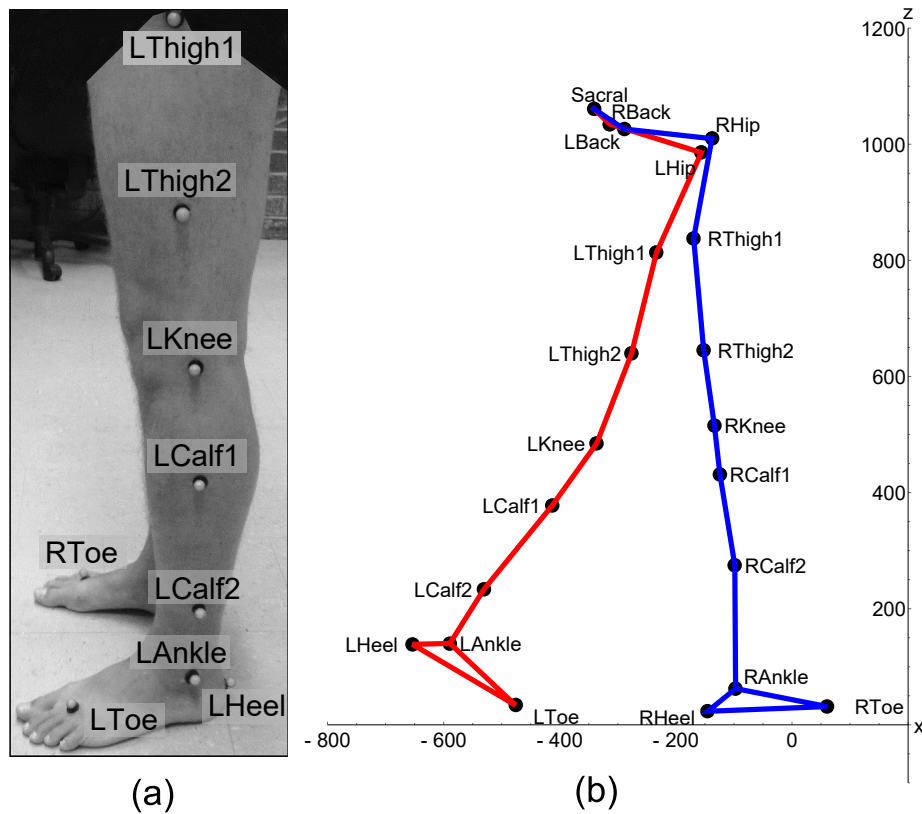


Figure 1.21: (a) Marker placement locations of the lower leg to study normal walking. (b) Motion Capture still displaying the capture data in 2D (X-Z) consisting of markers (black points), left leg markers are connected with line segments in red, right leg markers are connected by line segments in blue.

recorded motion capture information is sectioned into multiple cycles, starting and ending at the heel strike of the same foot as shown in Figure 1.22. Each full cycle is divided into the stance phase (0-60%) when the foot is in contact with the ground, and the swing phase (60% - 100%) when it is not. Foot trajectory and joint angles are computed for each cycle.

## 1.5 Geometric Design of Planar Linkages

From the above discussion, we observe that for both wearable orthotic devices, as well as robotic thumb devices, it is preferable to have devices with a simple structure, anthropometric sizes and, ideally, anthropomorphic appearance. It has been observed that even though

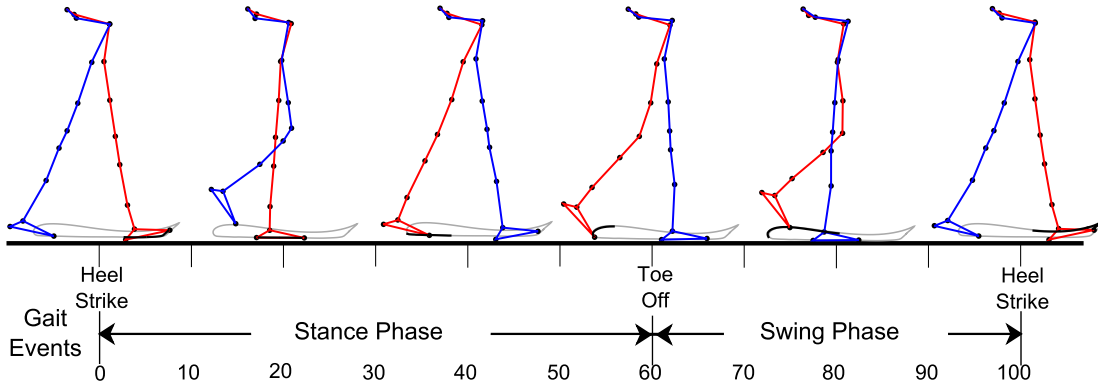


Figure 1.22: Human gait through one cycle in the sagittal plane, beginning and ending at heel strike.

the trajectories formed by the human lower-limb during walking, and fingers during grasping are not exactly planar due to the presence of abduction degree of freedom at the hip and MCP joints respectively, successful clinical trials of devices such as Lokomat and HandSOME [13] show that the ankle and fingertip trajectories can be treated as planar in the sagittal plane, and for palmar movements respectively [69]. In the work presented here, we aim to synthesize exoskeleton- type linkages to trace anthropomorphic trajectories.

### 1.5.1 Overview

The objective of the kinematic synthesis of linkages is to find the dimensions of a mechanism that can produce a specified trajectory. It is often divided into three categories of tasks: function generation, path-point generation and motion generation. Function generation requires that the angles of two links are coordinated in a particular fashion,  $(\phi_j, \psi_j), j = 0, \dots, N - 1$ , see Figure. 1.23(a). Motion generation requires that an end-effector link moves through a set of task positions, each specified by a translation and orientation,  $T_j = (P_j, \theta_j), j = 0, \dots, N - 1$ , see Figure. 1.23(b). The position and orientation of the guided rigid-body at the designated location is called a task position. Path generation requires that a coupler point traces through a set of points,  $P_j, j = 0, \dots, N - 1$ , see Figure. 1.23(c). In each case, the task specification is defined by  $N$  control points [70, 71].

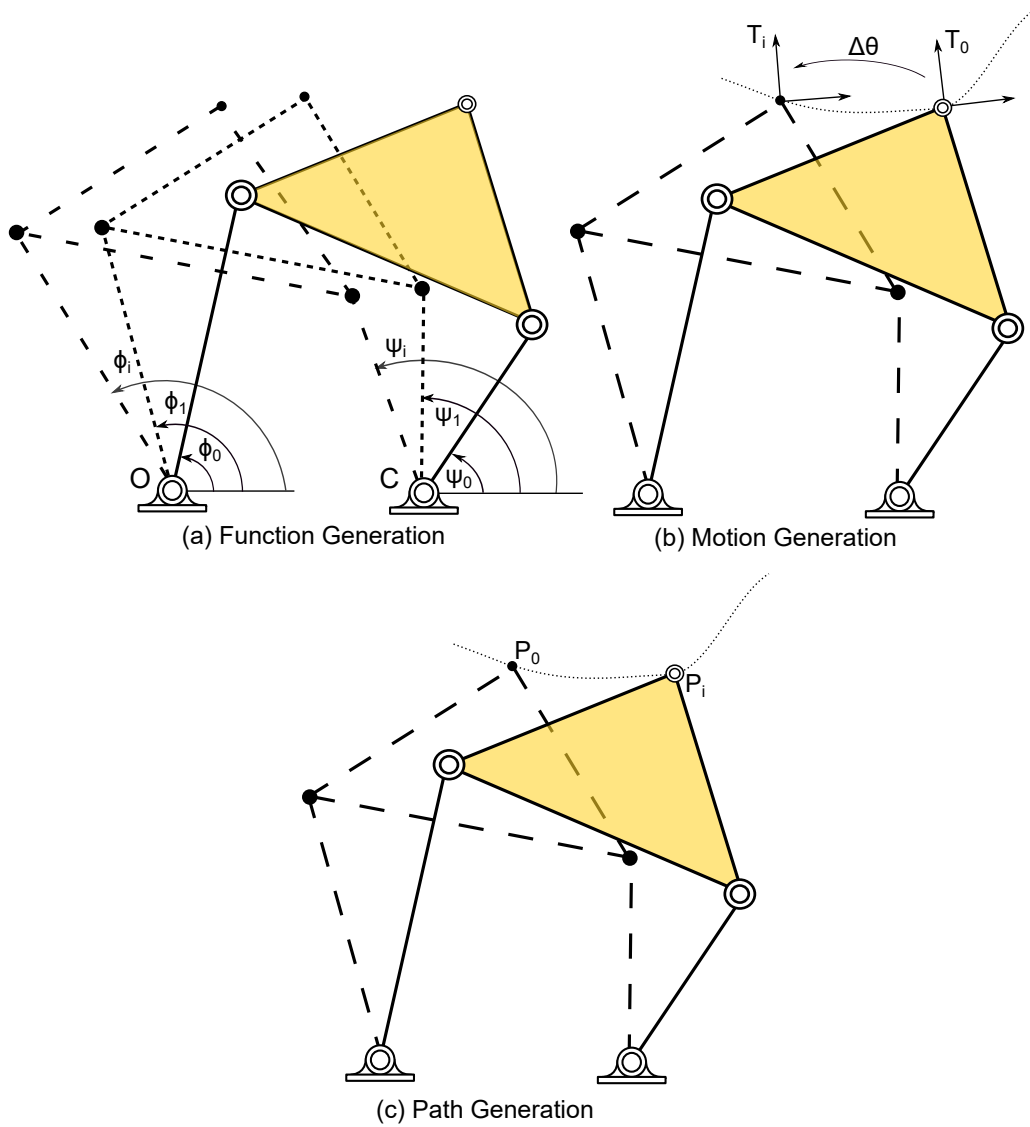


Figure 1.23: Three types of task specifications for kinematic synthesis.

## 1.5.2 Complex Notation

Kinematic formulations can be described using complex numbers to represent vectors. That is, the position of a point  $G$  relative to a fixed frame  $F$  can be specified in the complex plane as:

$$G = G_x + G_y i \tag{1.1}$$

It has a complex conjugate given by  $\bar{G} = G_x - G_y i$ , where  $i = \sqrt{-1}$ . For a serial 2R chain,

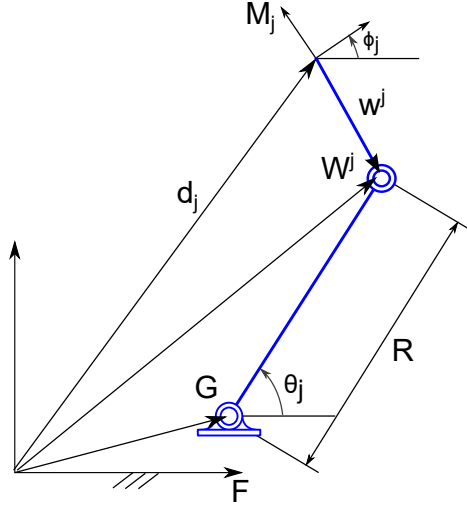


Figure 1.24: A 2R chain in the complex plane.

consisting of a proximal link and distal link as shown in Figure. 1.24, the location of the fixed pivot relative to the fixed frame  $F$  is  $G$  and the length of the proximal link is  $R$ . The  $j^{th}$  task position is described by  $M_j$  and can be specified by a location vector  $d_j = d_{jx} + d_{jy}i$  and an orientation angle  $\phi_j$ , both relative to the fixed frame  $F$ . For convenience, the position can be given by the transformation  $[T_j] = [e^{\phi_j i}, d_j]$ . The location of the moving pivot relative to  $M_j$  is  $w^j = w_x^j + w_y^j i$ , having a complex conjugate  $\bar{w}^j = w_x^j - w_y^j i$ . With respect to the fixed frame, it can be written as:

$$W^j = W_x^j + W_y^j i = (W - G)e^{\theta_j i} = (W - G)T_j \quad (1.2)$$

### 1.5.3 Design Equations

Solving the constraint equations for motion, function or path generation of four and six-bar linkages generates all possible solutions but can be a challenging task.

The synthesis equations of a 2R serial chain for position, velocity and acceleration specifications will be formulated in the following chapters, and the algebraic solution to the set

of four bilinear equations that describe a 2R chain is presented in McCarthy & Soh [70] for the case of five position synthesis and applies without any changes to the case of two position synthesis with velocities and acceleration specifications. Combining two 2R constraints yields a four-bar linkage.

Synthesis equations for general six-bar linkages result in polynomial systems of very high degrees. Wampler et al.[97] presented techniques for using complex coordinates to solve these polynomial systems by using homotopy methods. The general synthesis equations are solved by Plecnick and McCarthy [72] using regeneration homotopy method using the software package BERTINI.

## **1.6 Performance Optimization of Linkages**

### **1.6.1 Overview**

In applications requiring continuous path generation, algebraic synthesis techniques may not be sufficient to obtain satisfactory linkage designs as they cannot provide control over the path generated between the consecutive precision points specified by the designer on a curve [73]. In particular, cam-linkage mechanisms [33] and optimization techniques [31] have played an important role in synthesizing mechanisms that generate precise gait trajectories. The importance of optimization process for this problem lies in the fact that the number of points of the path generated by the coupler or the number of variables which defines the path is much higher than the number of design variables available for single DOF linkages.

## 1.6.2 Objective Functions

Since the target of path synthesis and optimization based synthesis methods is to determine the dimensions of linkages that can follow a specified curve, the path of the coupler point of the designed mechanism must be compared with the target path. The most commonly used objective function measures the error as the sum of the square of distances between the points of the desired and generated paths, which is called structural error function [74].

Ullah and Kota [75] introduced the concept of defining an objective function that purely compares the shape of the desired and coupler curves using Fourier descriptors. The size, orientation, and position of the desired curves were addressed in a later stage, however such methods are only applicable when its possible to scale, translate or rotate the optimal solution to obtain the final design. Zhou and Cheung [76] use the orientation structural error of the fixed link to calculate the difference between the desired and generated paths. Sedano et al. [77] introduced a new error estimator which compared the function generated by the proposed mechanism with the desired function. Matekar and Gogate [78] introduced a modified distance error function by introducing a tunable factor of equivalence between the transverse and longitudinal errors between the prescribed and the synthesized paths. Buskiewicz [79] presented a new technique for the path generation synthesis of four-bar linkages in that the deviation of generated path of the joints from the ideal path is considered as the error function. Nadal et al. [80] describe the use of turning functions to compare errors between the coupler and the target paths. As with Fourier descriptors, measured errors described with turning functions do not depend on the mechanism scale or the position and rotation of the ground link, therefore, reducing the search space. Kim [81] use the first and second order derivatives of the root mean squared error of the coupler and desired curves to classify the trajectory of the four-bar crank rocker linkage into four types of shapes. Then the second step of optimization is carried out on the subset of the design candidates that generate the desired shape of the trajectory. Further, Kafash and Nahvi [82] used a Circular

Proximity Function based objective function that requires the least number of optimization variables.

Tsuge et al. [83] introduced a method to quantify the deviation of the coupler curve from the desired curve through the use of the inverse kinematics formulation of the linkage to be optimized for the all the points on the desired curve.

### 1.6.3 Constrained Optimization

For the development of wearable devices, considerations of size, shape and manufacturability are important practical concerns that impose constraints on the search space during the optimization process. The objective function is minimized under the condition that the generated solution satisfies a set of constraints. A general formulation for constrained optimization is:

$$\begin{array}{ll}
 \text{Find} & \mathbf{x} = (x_0, x_1, \dots, x_{n-1})^T, \quad x \in \mathfrak{R}^n \\
 \text{minimize} & \mathbf{f}(\mathbf{X}) \\
 \text{subject to} & \mathbf{G}_m(\mathbf{x}) \leq 0, \quad m = 1, \dots, M
 \end{array} \tag{1.3}$$

Constraints typically increase solution complexity of the optimization problem because they can create forbidden regions or introduce discontinuities on the objective function landscape that restrict the free assignment of values to the design parameter vectors. Design parameter vectors that violate the constraints can either be modified by the optimization algorithm such that the modified vector satisfies all constraints or penalties can be applied to the objective function so as to make the set of design parameters unfeasible [84].

Commonly used constraints in optimal synthesis of mechanisms include ensuring that the link

dimensions are within a desired range, the mechanism satisfies Grashofs criteria, positions are generated in the desired order, all generated positions belong to the same branch, mechanical advantages at design positions are satisfactory, and transmission angles fall within acceptable limits [85].

#### 1.6.4 Optimization Approaches

Numerous authors have dealt with solving the problem of optimum synthesis of path-generating planar mechanisms, using both gradient-based and nature-inspired algorithms. Evolutionary strategies such as Genetic Algorithm (GA) are widely used for finding four-bar linkages [86] when a globally optimal solution is desired. Other evolutionary strategies like Cuckoo Search (CS) [87], Imperialistic Competitive Algorithm (ICA) [88] and Krill Herd (KH) [89] among others have also been used for synthesis of planar-mechanisms. A lot of work has also been done on combining methods, such as using GA with fuzzy logic controllers [90], real-valued GA with Differential Evolution (DE) [91], as well as combining gradient based methods with evolutionary methods such as tabu-search [85]. Hybrid Algorithms aim to improve efficiency, accuracy of the optimization process and to drive the solution ever closer to the global minimum.

Typically for evolutionary strategies, the initial linkage design is randomly selected or based on mechanism catalogs. Hongying et al. [92] proposed a method to select a subset of all possible four-bar linkages coupler curves that form the solution space by introducing a coupler angle function, thereby reducing the size of the optimization problem. More recently, Tsuge et al. [83], introduce a method in which homotopy generated exact solutions are used as starting guesses for gradient optimization methods to generate a number of locally optimal linkage candidates, from which the designer selects the final solution.

## 1.7 Contributions

The goal of this dissertation is a design process for customized wearable devices that provide joint guidance and support for individuals with disabilities in their hands or legs in order to increase mobility. As discussed above, a variety of general purpose devices have been developed to address the need for joint guidance and support, ranging from robotic exoskeletons to braces with spring activated clutches and ratchets. The design process presented in this dissertation yields devices adapted to the specific needs of the individual that do not require external power or spring-actuated clutches and ratchets. They are less complex, more robust, and less costly solutions to providing the mobility needs of an individual. The specific contributions of this dissertation are as follows:

- A new procedure to combine motion capture to specify the position, velocity and acceleration of thumb curling with the design of a four-bar linkage driven thumb to facilitate grasping.
- A new procedure to combine motion capture to specify the position, velocity and acceleration of the knee joint and the design of a four-bar linkage driven hands-free crutch. An example device was built and tested and found to reduced hip-hiking compared to locked-knee devices.
- A new procedure to combine motion capture that specifies the angular movement of the knee and ankle as well as the trajectory of the metatarsal and the design of a six-bar linkage driven knee-ankle-foot orthosis. An example device was built and tested and found match the knee and angle angular movement, but did not match the metatarsal trajectory, over-extended the ankle by  $20^\circ$ , and match the stride length up to 97% of normal walking.
- A new approach to the combination of kinematic synthesis and optimization in order

to design a six-bar linkage for a knee-angle-foot orthosis that achieves a specified coordination of joint angles and metatarsal trajectory. The result is a device that matches the knee and ankle angular movement and the metatarsal trajectory.

# Chapter 2

## Design of Passive Mechanical Thumb Orthosis

### 2.1 Introduction

A systematic method for the kinematic synthesis of one DOF thumb linkage is presented here. The motion of the thumb in consideration for this design is a planar curling motion around the anterior-posterior axis at the thumb MCP joint used in rehabilitative exercise therapy. We propose to replicate this planar thumb movement by synthesizing a single DOF four-bar linkage. This topology is selected as we kinematically model the curling movement of the thumb with a 2R serial chain. Combining two 2R serial chains yields a four-bar linkage.

The design of a thumb linkage that is anthropometric in size and moves through an anthropomorphic trajectory is a challenging task. In this work the anthropomorphic design tasks are defined by specifying not only positions, but higher order motion derivatives such as velocities and accelerations that are related to the curvature constraints of the thumb trajectory.

The five task specifications required for exact synthesis of a four-bar motion generator are specified from the motion capture data of an individual performing the thumb curling task. This yields position, velocity and acceleration constraint equations that constitute the set of algebraic design equations for planar 2R chains. The solution of these design equations give dimensions for 2R constraints that are attached together to form the individualized four-bar thumb orthosis that moves smoothly through the anthropomorphic task specified.

## **2.2 Design Procedure**

### **2.2.1 Individualized Task Specifications using Thumb Motion Capture**

To design the custom anthropometric thumb orthosis, we obtain 3D optical motion capture data of an individual performing the planar thumb curling action. This planar movement can be attributed to the flexion-extension motion of the thumb around its MCP joint, and the flexion-extension motion of the distal phalanx of the thumb around the IP joint. In order to isolate the planar motion from the 3D motion capture data, the thumb motion data is transformed such that the MCP joint is placed at origin of the fixed reference frame. Studying the movement of the proximal and distal phalanges in terms of their direction cosines helps to identify the dominant plane of movement of the thumb during this particular task. The 3D data is then transformed such that the primary plane of motion of the thumb coincides with the X-Z plane. This ensures that the planar data of the thumb movement describes its general behavior with high fidelity, and the out-of-plane movements are negligible. The transformed 2D motion capture stills of the thumb motion (in XZ plane) are shown in Figure. 2.1.

In addition to the trajectory, we study the velocity and accelerations observed at the tip

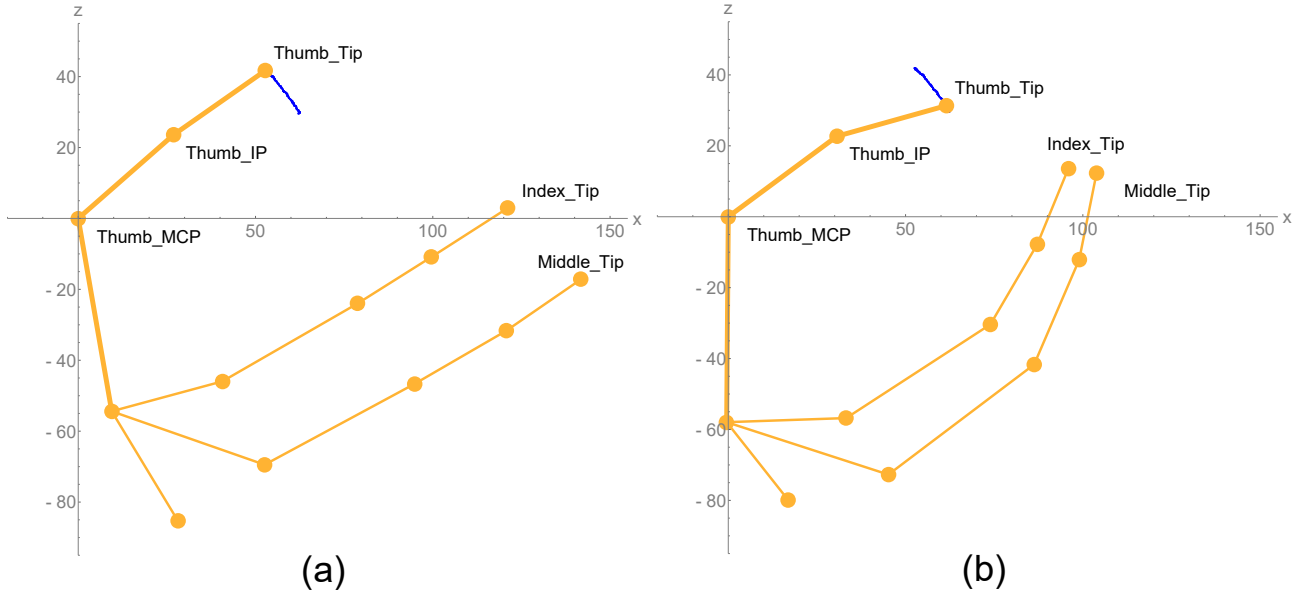


Figure 2.1: 2D Motion Capture stills of thumb at the beginning and end of the planar curling task.

of the individual’s thumb during the curling motion. These are obtained by taking time derivatives of the motion data, and are shown in Figure. 2.2.

Kinematically the motion of the thumb is approximated with a 2R serial chain, with the two revolute joints coinciding with the MCP and IP joints of the individual’s thumb. The average lengths of the proximal and distal phalanges are used to size the link lengths  $l_1$  and  $l_2$  of the 2R chain, and are listed in Table. 2.1. In the next section we solve the algebraic

$l_1$ (mm)	$l_2$ (mm)
36.97	31.96

Table 2.1: Dimensions of a 2R chain that models the planar motion of the human thumb obtained from motion capture data.

synthesis equations for a four-bar linkage in order to obtain a thumb orthosis. The goals of the synthesis process are to identify a four-bar linkage that is compact, lies behind the thumb during the entire range of its motion and acts as an exoskeleton type orthosis - i.e. provide exact guidance at the MCP and IP joints of the thumb.

The task specification for the kinematic synthesis are specified in terms of task positions and

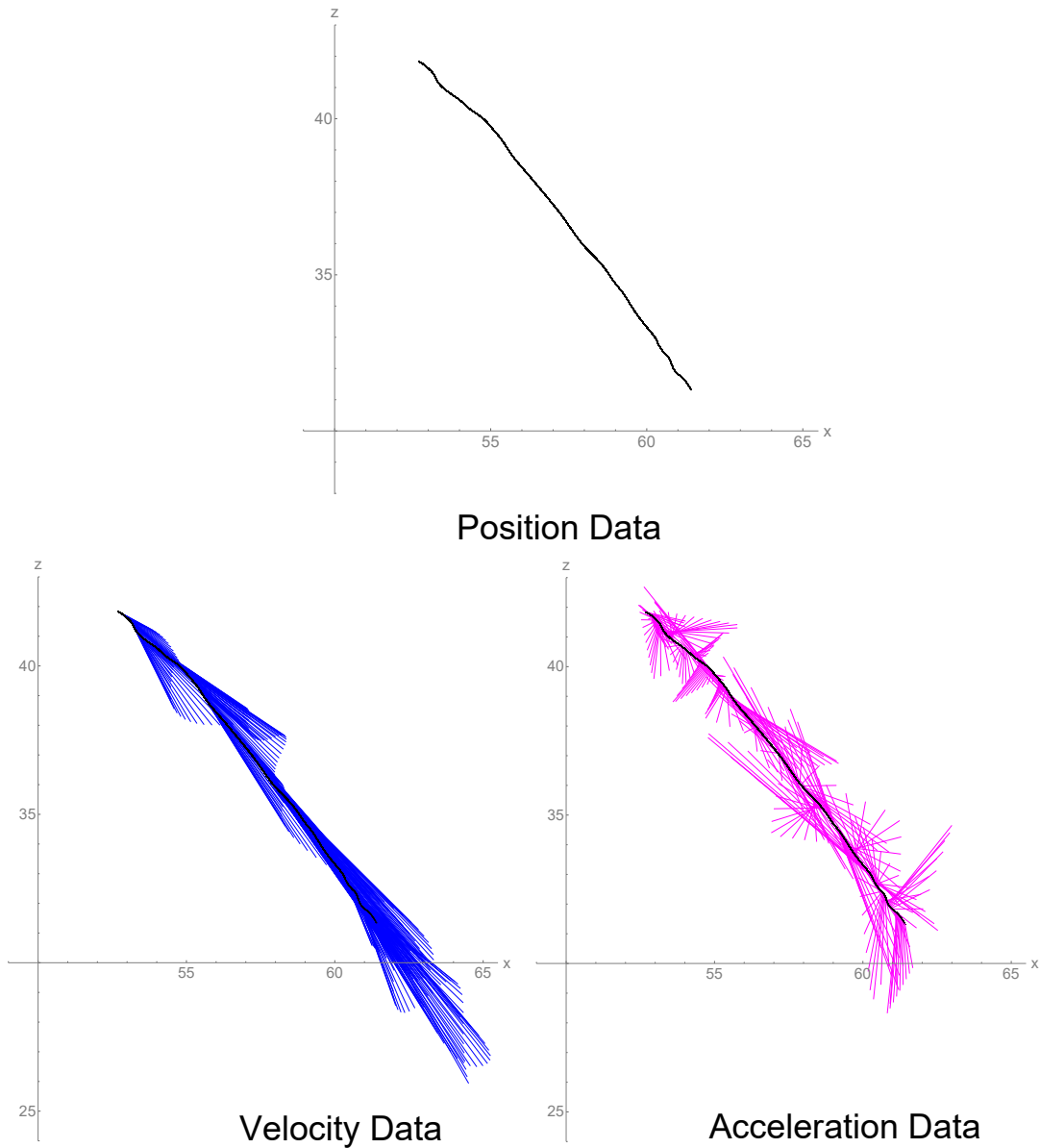


Figure 2.2: Position, velocity (blue) and acceleration (magenta) data at the tip of thumb during its curling motion.

their higher-order motion derivatives, based based on the theoretical framework created by Robson and McCarthy [93, 94], which used contact with specified objects in the environment to define velocity and acceleration specifications for the movement of an end-effector. Here we obtain this data from optical motion capture.

The movement  $M$  of the end-effector is determined such that its position and velocity are known in one location, and its position, velocity and acceleration are known in the second

location. As the synthesized linkage will trace a trajectory between these two locations, we specify  $M_1$  at the beginning of the thumb curling trajectory, and  $M_2$  at its end. Figure. 2.3 shows a set of 20 velocities and accelerations isolated at the beginning of the curling motion, and a set of 10 velocities and accelerations at the end.

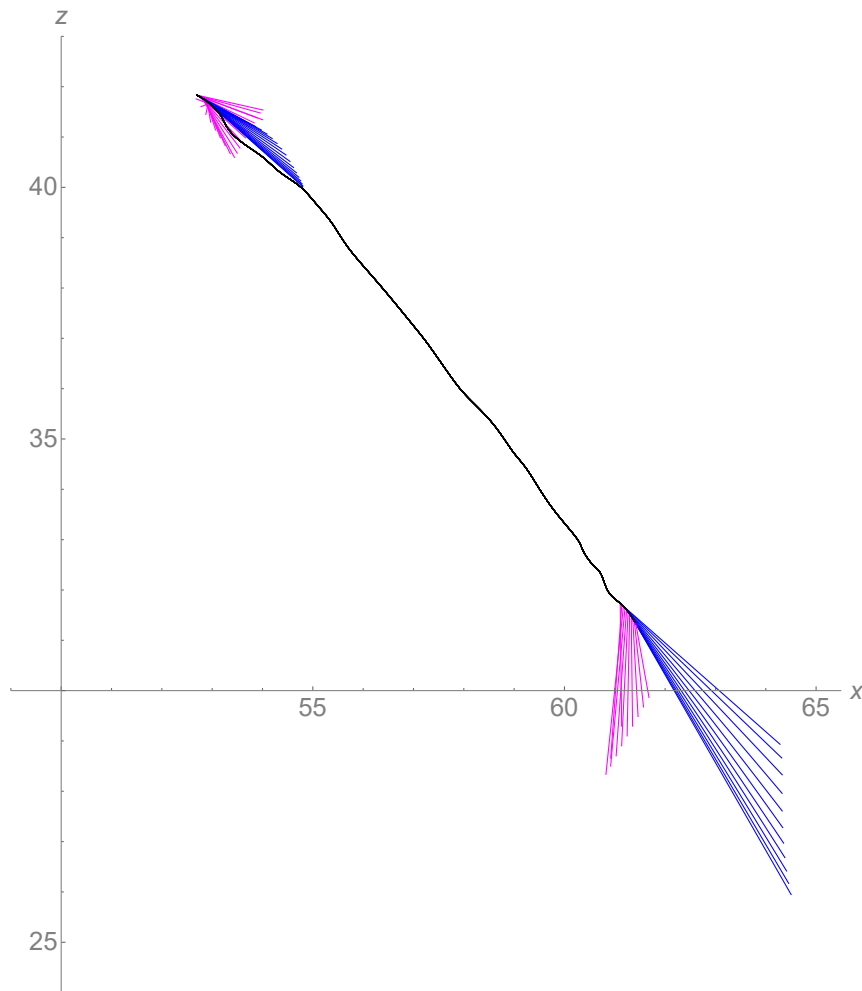


Figure 2.3: Velocities (blue) and accelerations (magenta) calculated at the beginning and end of the thumb trajectory.

We have to choose a set of two task specifications such that at the first location  $PV_1$ , which corresponds to the onset of the flexion motion of the thumb, position and velocity are specified, and at the second location  $PVA_2$ , which coincides with the point of contact of the thumb with the object being grasped, position, velocity and acceleration of the thumb tip are specified, as shown in Figure. 2.4. The acceleration of the thumb tip at the second

location enforces the curvature constraints for maintaining the contact between the tip of the thumb and the grasped object. The negative velocity and acceleration values indicate that the trajectory curves downwards as shown Figure. 2.3.

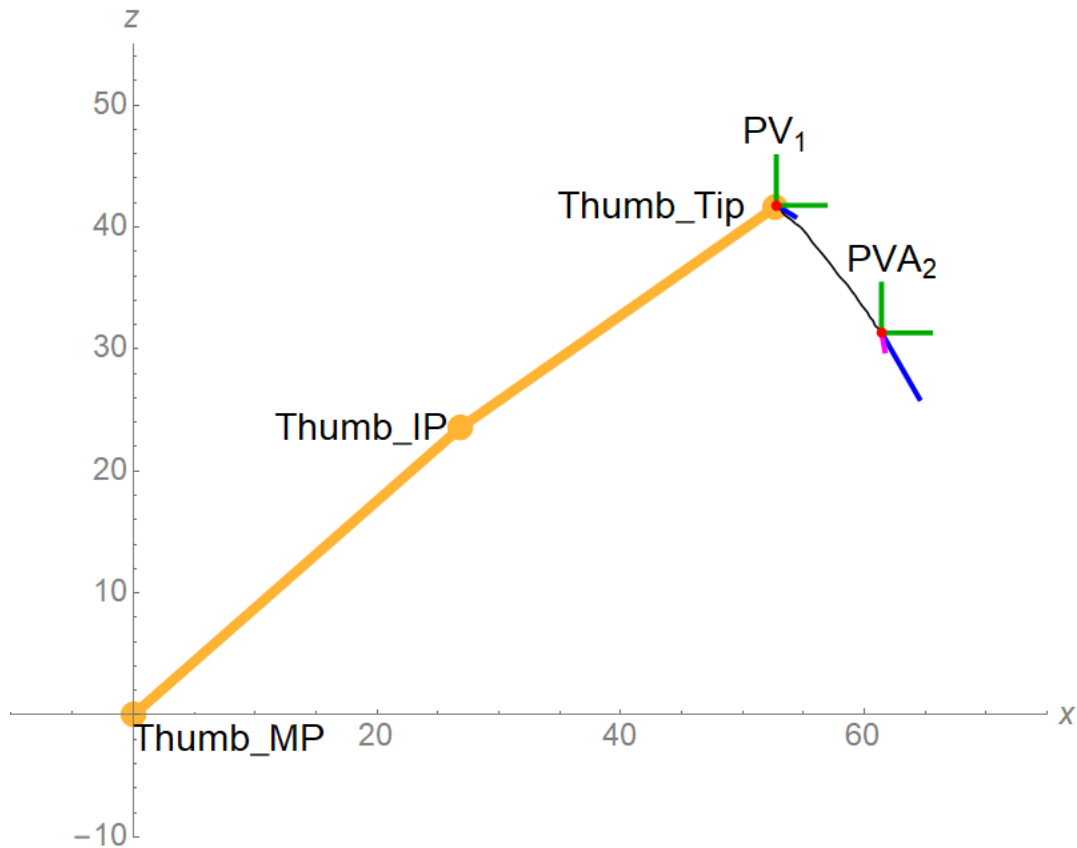


Figure 2.4: Task specifications for synthesis of a 2R chain to produce thumb trajectory: The green frames indicate position specification, blue lines indicate velocity specifications, and the magenta line indicated the acceleration specification.

In order to choose an appropriate set of task positions from the dataset, an iterative algorithm is run which identifies the optimal set consisting of  $PV_1$  and  $PVA_2$ , where  $P_1$  is at the beginning of the trajectory and  $P_2$  lies at the end. The 2R constraint equations described in the next section are solved for a total of 200 combinations of  $PV_1$  and  $PVA_2$ . The optimal task positions found are shown in Figure. 2.5, and enumerated in Table 2.2.

Task	1	2
Position $(\theta(^{\circ}), P_x(mm), P_y(mm))$	(0, 52.7845, 41.7831)	(0, 61.418, 31.3272)
Velocity $(\dot{\theta}(^{\circ}), \dot{P}_x(mm/s), \dot{P}_y(mm/s))$	(1, 1.50581, -0.911455)	(1, 3.08535, -5.3787)
Acceleration $(\ddot{\theta}(^{\circ}), \ddot{P}_x(mm/s^2), \ddot{P}_y(mm/s^2))$	-	(0, 0.523598, -2.92859)

Table 2.2: The anthropomorphic task data obtained from the motion capture of the curling movement of a human thumb.

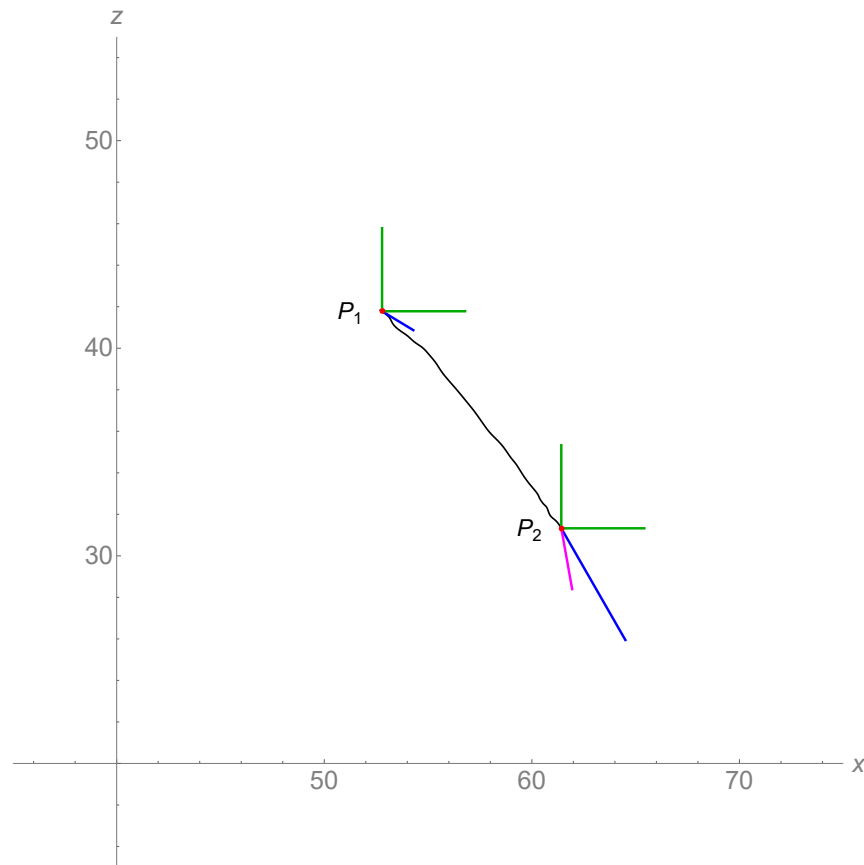


Figure 2.5: The kinematic task for synthesis of a 2R chain.

## 2.2.2 Kinematic Synthesis of Four-bar Thumb

The task consists of positioning the tip of the thumb, modeled as a planar 2R chain, at a start and a finish position, which are given by  $PV_1$  and  $PVA_2$ . The design parameters for the 2R chain are the pivot locations  $G = G_x + G_y i$  for the fixed pivot, and  $W = W_X + W_y i$

of the moving pivot at the first task position.

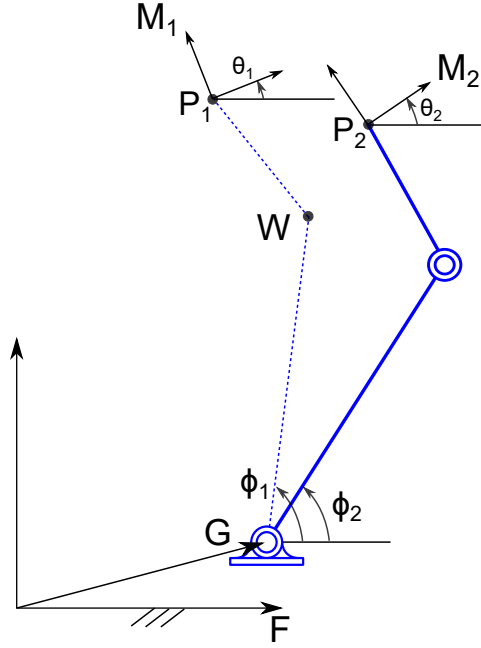


Figure 2.6: A general planar 2R chain displayed in the 1<sup>st</sup> and 2<sup>nd</sup> task positions.

The design equations for motion generation of a 2R chain can be developed for the given set of two task positions  $M_j, j = 1, 2$ , shown in Figure. 2.6. The orientation of the end-effector  $\theta_j$  and its position  $P_j = P_{xj} + P_{yj}$  on that link serve as the  $j^{\text{th}}$  task position. The orientation of the proximal link in the  $j^{\text{th}}$  position is measured by the angle  $\phi_j$ . The two sets of angles  $\phi_j$  and  $\theta_j$  define complex rotation operators  $Q_j$  and  $T_j$  as,

$$Q_j = e^{\phi_j i} \quad T_j = e^{\theta_j i}, \quad j = 1, \dots, N \quad (2.1)$$

which satisfy

$$\begin{aligned} T_j \bar{T}_j &= 1 \\ Q_j \bar{Q}_j &= 1 \quad j = 1, \dots, N \end{aligned} \quad (2.2)$$

The task positions  $P_j, j = 1, \dots, N$  can be written in terms of the locations of the fixed and

the moving pivots  $G$  and  $W$  as:

$$P_j = G + Q_j(W - G) + T_j(P_1 - W), \quad j = 1, \dots, N \quad (2.3)$$

The complex conjugate of the Equation. 2.3 is given by:

$$\bar{P}_j = \bar{G} + \bar{Q}_j(\bar{W} - \bar{G}) + \bar{T}_j(\bar{P}_1 - \bar{W}), \quad j = 1, \dots, N \quad (2.4)$$

Combining the constraint equations of the 2R chain, with its complex conjugates and the rotation normalization equations give us:

$$\begin{aligned} P_j &= G + Q_j(W - G) + T_j(P_1 - W) \\ \bar{P}_j &= \bar{G} + \bar{Q}_j(\bar{W} - \bar{G}) + \bar{T}_j(\bar{P}_1 - \bar{W}) \\ T_j \bar{T}_j &= 1 \\ Q_j \bar{Q}_j &= 1 \quad j = 1, \dots, N \end{aligned} \quad (2.5)$$

The unknowns  $Q_j, \bar{Q}_j$  can be eliminated from the above equation using the relationship  $Q_j \bar{Q}_j = 1$ , resulting in:

$$(W - G)(\bar{W} - \bar{G}) = ((G - P_j) + T_j(P_1 - W))((\bar{G} - \bar{P}_j) + \bar{T}_j(\bar{P}_1 - \bar{W})), \quad j = 2, \dots, N \quad (2.6)$$

Equation. 2.6 is a system of  $N - 1$  equations in four unknowns  $G, \bar{G}, W, \bar{W}$ , and for case where  $N = 2$ , it yields a single equation in four unknowns. Thus, we require three more equations to obtain an exact solution to this system.

The time derivative of the 2R constraint yields the velocity constraint equation,

$$\begin{aligned} &(-\dot{P}_j + i\dot{\theta}_j T_j(P_1 - W))((\bar{G} - \bar{P}_j) + \bar{T}_j(\bar{P}_1 - \bar{W})) \\ &+ ((G - P_j) + T_j(P_1 - W))(-\dot{\bar{P}}_j - i\dot{\theta}_j \bar{T}_j(\bar{P}_1 - \bar{W})) = 0, \quad j = 1, 2 \end{aligned} \quad (2.7)$$

And the time derivative of the velocity constraint yields the acceleration constraint equation,

$$(-\ddot{P}_j + i\ddot{\theta}_j T_j(P_1 - W) - \dot{\theta}_j^2 T_j(P_1 - W))((\bar{G} - \bar{P}_j) + \bar{T}_j(\bar{P}_1 - \bar{W})) + ((G - P_j) + T_j(P_1 - W))(-\ddot{\bar{P}}_j - i\ddot{\bar{\theta}}_j \bar{T}_j(\bar{P}_1 - \bar{W}) + \dot{\bar{\theta}}_j^2 \bar{T}_j(\bar{P}_1 - \bar{W})) = 0, \quad j = 2 \quad (2.8)$$

Equations. 2.6 -2.8 are the synthesis equations of a 2R serial chain that moves through two locations such that it does not violate the velocity and acceleration constraints defined at the locations. The algebraic solution to this set of four bilinear equations for a 2R chain is presented in McCarthy & Soh [70] for the case of five position synthesis and applies without any changes to the design equations formulated here. Combining two 2R constraints yields a four-bar linkage.

### 2.2.3 Synthesis Results

Of the set of solutions obtained for the 2R chain, solutions that place the all the pivots, both fixed and moving, at the back of the hand during the entire motion are selected. The most compact linkage that can produce the desired trajectory of the individual's thumb allows for a point of contact between the distal phalange and the coupler of the four-bar linkage, and guides the movement of the tip of the thumb. Then, real solutions of design equations for the task specifications chosen are shown in Table. 2.3.

Solution	$G = (u, v)$	$W_0 = (x, y)$
1	(16.79, 46.70)	(17.88, 76.36)
2	(0, 2.08)	(16.48, 34.42)

Table 2.3: The synthesis solutions for the pivot locations of the 2R constraint (in bold) that achieves the anthropomorphic contact and curvature task requirements.

The synthesis results for the planar four-bar linkage traversing the anthropomorphic trajectory described above is shown in Figure 2.7.

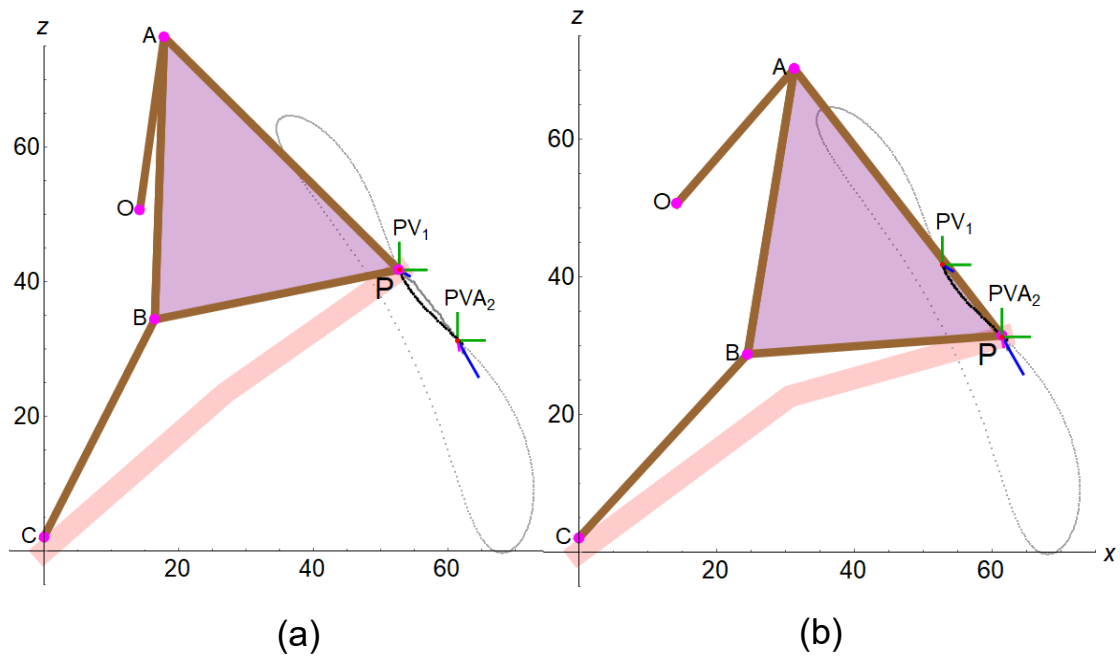


Figure 2.7: Result of synthesis of mechanical thumb at its (a) initial and (b) final positions in Mathematica.

## 2.3 Thumb Orthosis

Figure. 2.8 shows the conceptual design of the thumb orthosis, which places the four-bar linkage synthesized on the back of the human thumb, and acts as an end-effector type assistive device, as discussed in Chapter 1 (Figure. 2.9).

A full scale 3D printed thumb orthosis is manufactured and shown in Figure. 2.10.

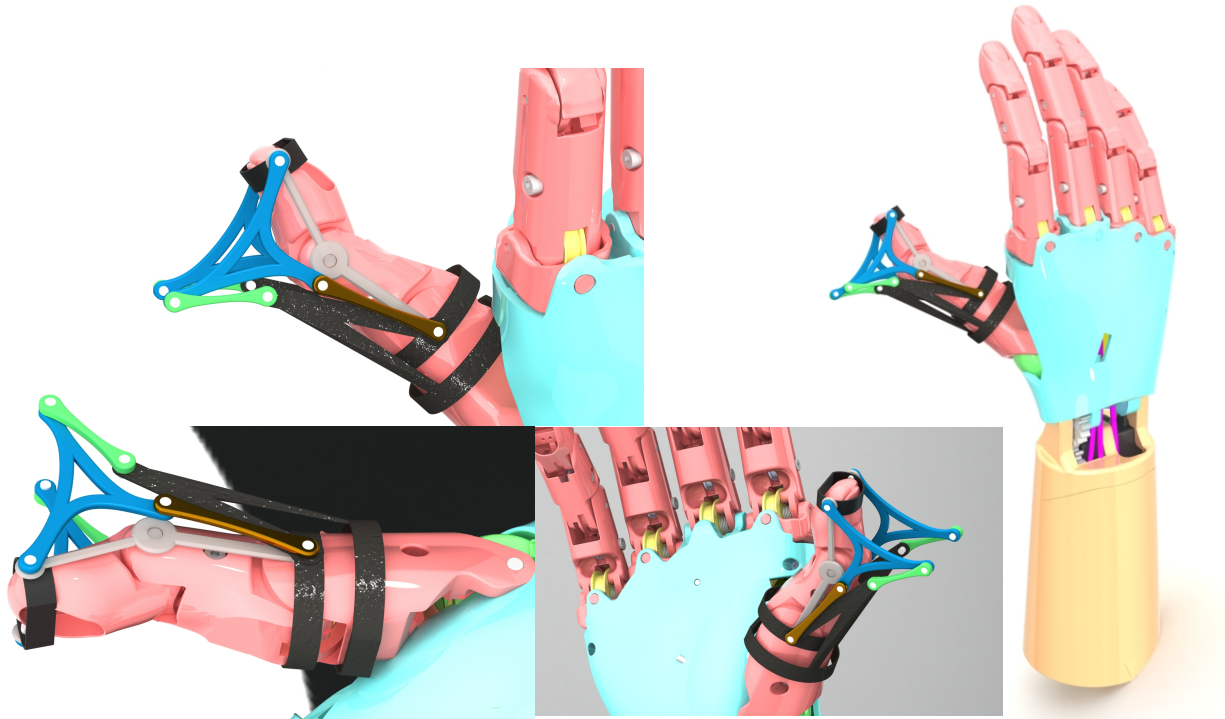


Figure 2.8: Conceptual design of the thumb assistive device.

## 2.4 Summary

A procedure for the synthesis of four-bar linkage for design of an individualized anthropomorphic end-effector type thumb orthosis is proposed. A four-bar linkage is chosen for the design as it is easy to design due to its simple structure, and it provides high grasping forces at the tip of the linkage. The design objectives for the thumb mechanism are to provide support at the MCP and IP joints of the thumb as it emulates the physiologically accurate curling motion for an individual. As the mechanism will be adapted to a wearable thumb orthosis, the body of the linkage must be located behind the hand for its full ROM to minimize interference with the user's hand. Finally the linkage must have anthropometric dimensions so that it can be attached easily to an individual's thumb to provide motion assistance.

The design solution results in an end-effector type thumb orthosis. The linkage synthesized passes smoothly through two task positions defined on the trajectory traced by the tip of

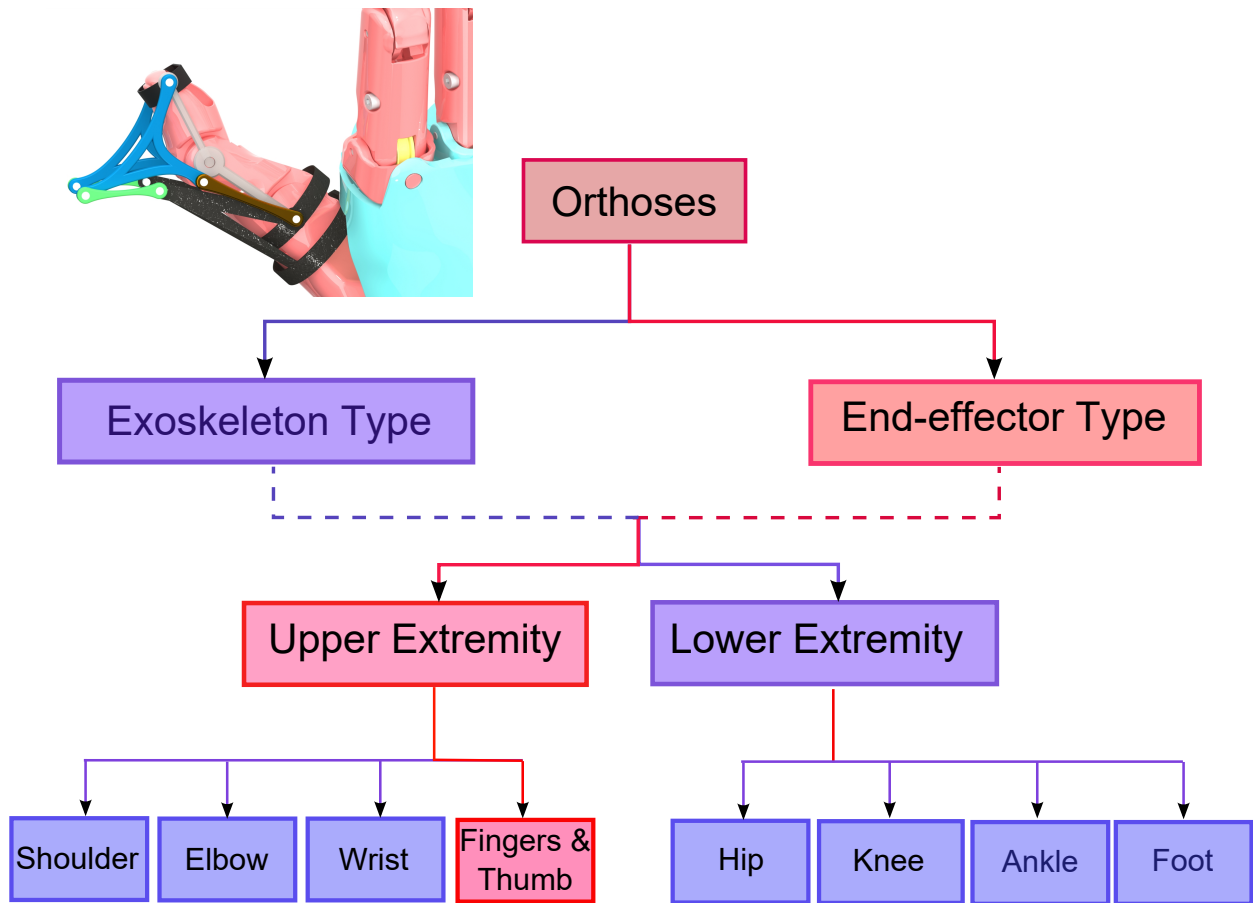


Figure 2.9: Classification of the individualized four-bar thumb orthosis designed based on modality of providing assistance.

the thumb for curling motion, obtained from the individual’s motion capture data. A solid model of the individualized thumb orthosis is built and a 3D printed full-scale prototype is also manufactured. The individualized thumb orthosis designed is anthropometric in size, compact and has fewer moving parts as compared to previously reported designs.



Figure 2.10: Full-scale 3D printed prototype of the thumb orthosis.

# Chapter 3

## Design of Passive Mechanical Multi-Axis Knee

### 3.1 Introduction

A process for the design of a multi-axis knee linkage-based orthosis that uses individual motion capture data is presented. The design of a knee device that can provide natural motion at the knee joint is expected to result in improvement in adoption and continued use of lower-leg assistive devices. The major reason for abandonment of lower-leg orthoses is restrictive or unnatural motion produced at the knee joint as discussed in Chapter 1.

Existing knee joints that are modeled as a single revolute joint fall under the category of single-axis knees, and in general are not able to simulate natural motion at the knee joint. Knee joint models with variable instantaneous center of rotations (also called multi-axis knees) have been found to produce a more natural motion. Multi-axis knees can be designed using closed-loop linkages, and the most commonly used linkage for this purpose is the four-bar [66].

Here we present a method that utilizes the movement trajectory and higher order motion constraints on knee joint trajectory to direct the synthesis of a compact four-bar knee mechanism. The designed knee mechanism is based on the individual optical motion capture data of the knee joint trajectory of a specific person during natural walking.

## 3.2 Design Procedure

### 3.2.1 Individualized Task Specification using Gait Data

In order to specify the task positions, we use experimental gait data obtained from motion capture of a subject walking normally on a treadmill at a self-selected speed of 1.3 m/s using a commercial infra-red passive marker-based motion capture system. The knee linkage has to be designed such that it attaches rigidly to the thigh of the user, thus the knee motion of interest is obtained by transforming the lower-leg motion data such that the thigh is held fixed. Figure. 3.1 shows the transformed lower-leg data.

Figure. 3.2 shows the relative trajectories of the markers placed on the bony landmarks at the anatomical knee and the ankle joints of the individual when the thigh is held stationary through out the walking motion.

Using the position data (XZ) of the marker on the knee joint, we obtain velocity and acceleration for the knee movement by numerical differentiation. The knee joint position, velocity and acceleration data obtained are shown in Figure. 3.3.

The position, velocity and acceleration data of the knee joint movement of an individual during walking is used to define the task specifications for the kinematic synthesis of a single DOF, closed-loop knee linkage. The four-bar linkage is the simplest planar closed-loop linkage, and is constructed by combining two 2R serial open chains with each other.

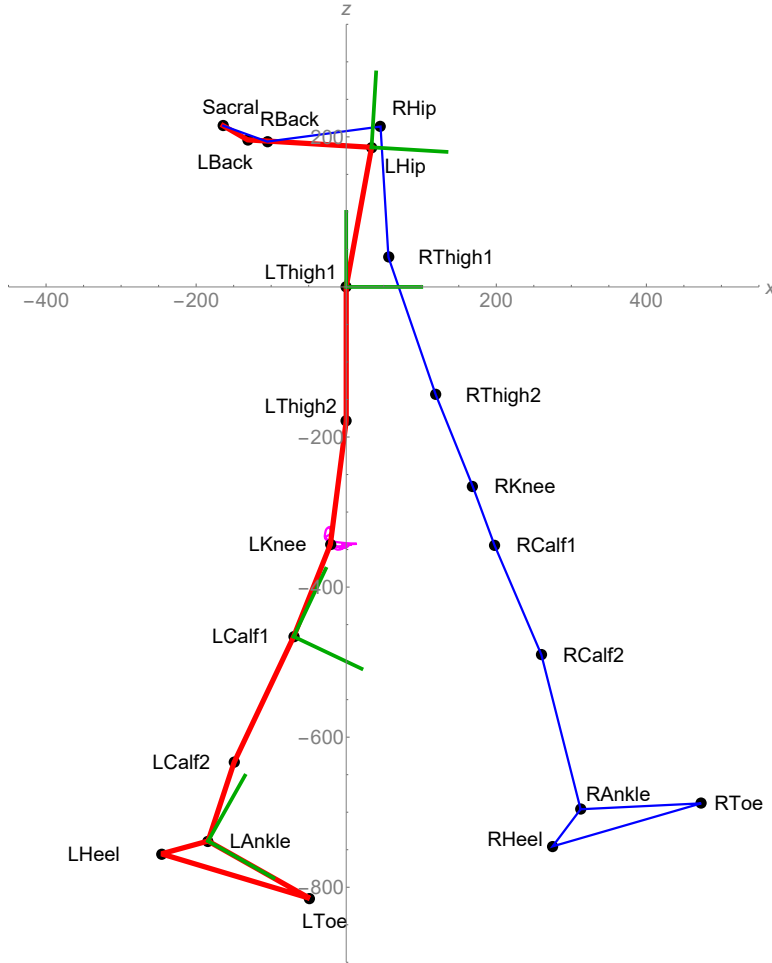


Figure 3.1: Motion capture data of the lower-leg when the thigh held fixed. The knee joint trajectory in the sagittal plane over a complete gait cycle is indicated in magenta.

A 2R chain has two DOF and is completely described by five structural parameters - the coordinates of its fixed and moving pivot, and length of the rigid link connecting these two pivots. When two 2R chains are combined together, the four-bar linkage obtained has one DOF. Thus we can specify five sets of task positions  $P_1, P_2, P_3, P_4, P_5$  to synthesize a 2R chain, where each task position is described by its location and orientation. We choose the five task specifications such that at the first task position, velocity and acceleration is specified as  $PVA_1$  and at the second task position  $PV_2$  defines the position and velocity of the knee joint trajectory. The acceleration is typically specified in positions where the shape of the desired trajectory must be taken into account - as in task position 1. In order to

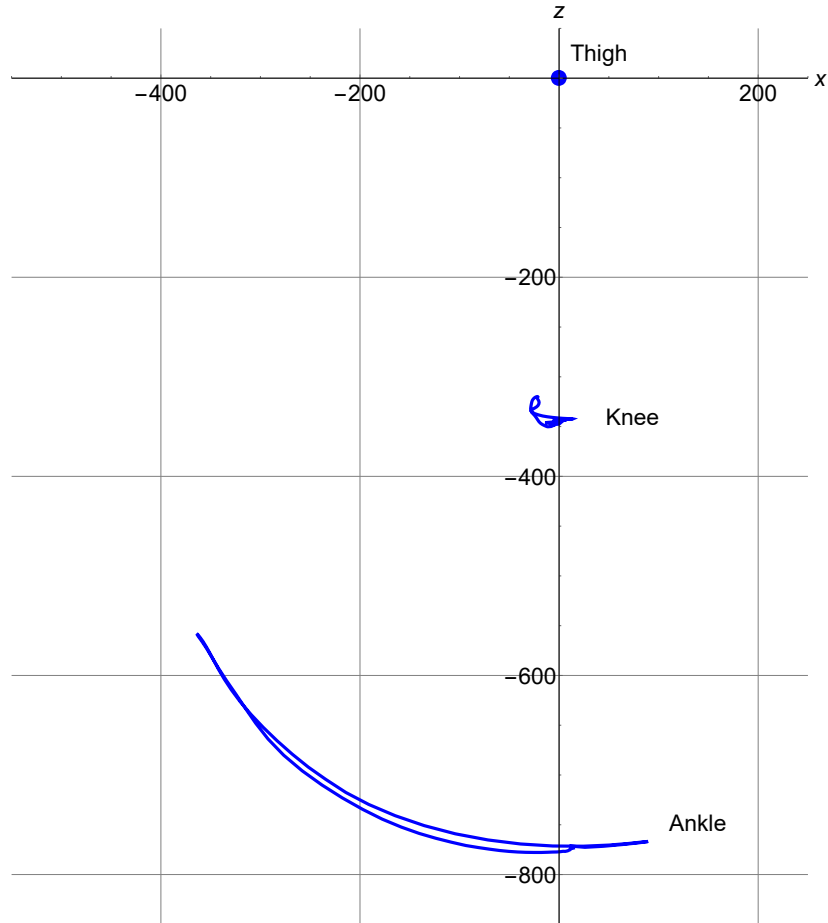


Figure 3.2: Trajectories of infra-red markers placed at knee and ankle joints during natural walking, transformed with respect to the thigh fixed frame.

choose the appropriate task positions from the dataset, a trial and error approach is used to find an optimal set of task positions and their higher-derivatives describing the whole movement as shown in Figure. 3.4. 190 combinations of  $PVA_1$  and  $PV_2$  are tested and the best set of task specifications are listed in Table. 3.1 and shown in Figure. 3.5. The positive velocity and acceleration value at the first task specification indicate which branch of the self intersecting knee trajectory is to be followed at the intersection point as shown in Figure. 3.5. Once the human motions are recorded and the contact task is specified, linkage based mechanism can be designed for the chosen physiological task.

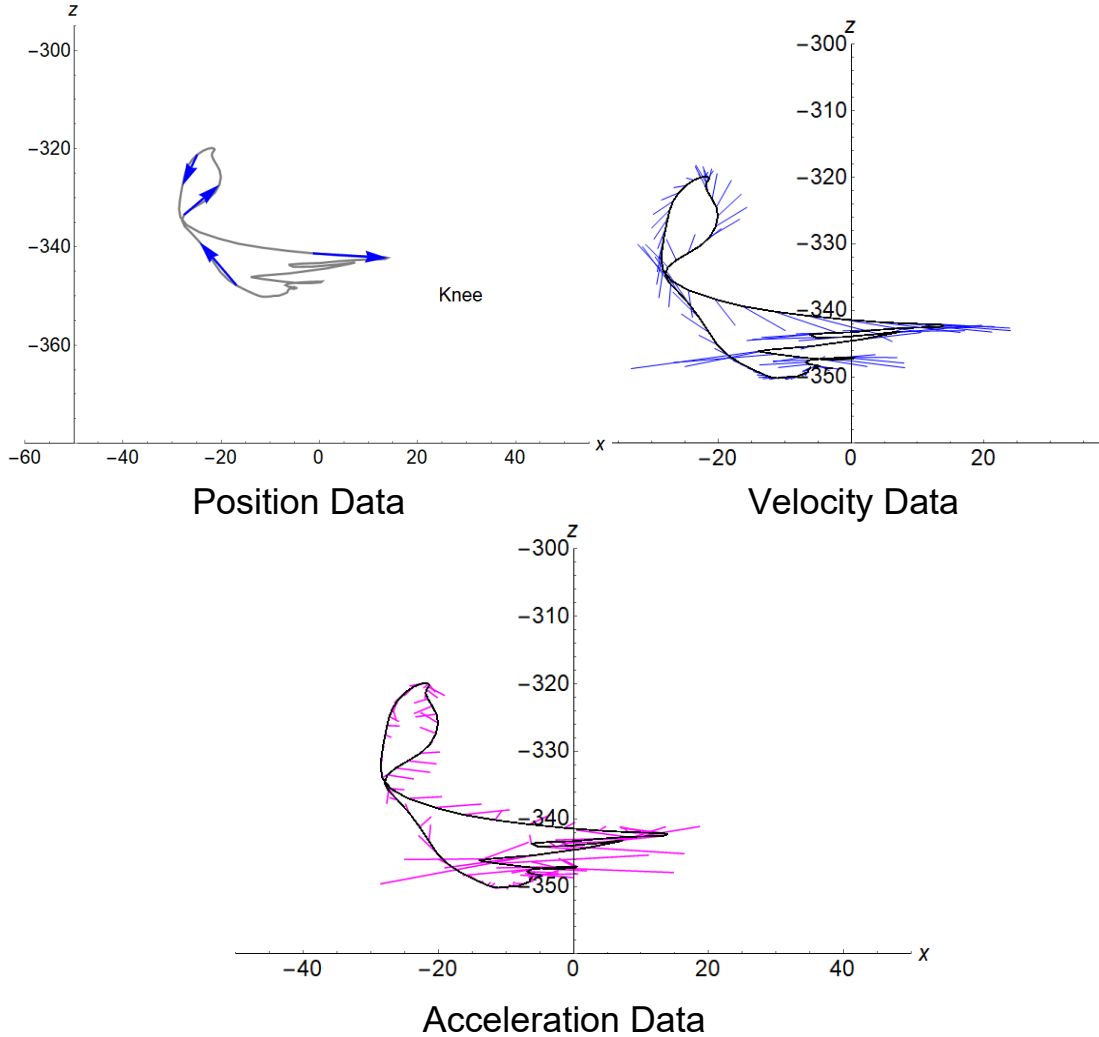


Figure 3.3: Position, velocity and acceleration data overlaid on the knee trajectory obtained from motion capture data of an individual walking. The blue arrows on the knee position data indicate the direction of knee joint movement over a single gait cycle starting and ending at heel strike.

### 3.2.2 Kinematic Synthesis of Knee Linkage

The objective of design process is to synthesize a four-bar linkage that can move an end-effector attached to its coupler link through  $N = 2$  task positions, defined by  $T_j = (P_j, \theta_j) = (P_{xj} + P_{yj}i, e^{i\theta_j})$ ,  $j = 1, 2$  as shown in Figure. 3.6. The goal of the synthesis process is to find the locations of the two ground pivots, given by  $O = O_x + O_yi$  and  $C = C_x + C_yi$ , and the two moving pivots,  $A_1 = A_x + A_yi$  and  $B_1 = B_x + B_yi$ , such that the four-bar linkage

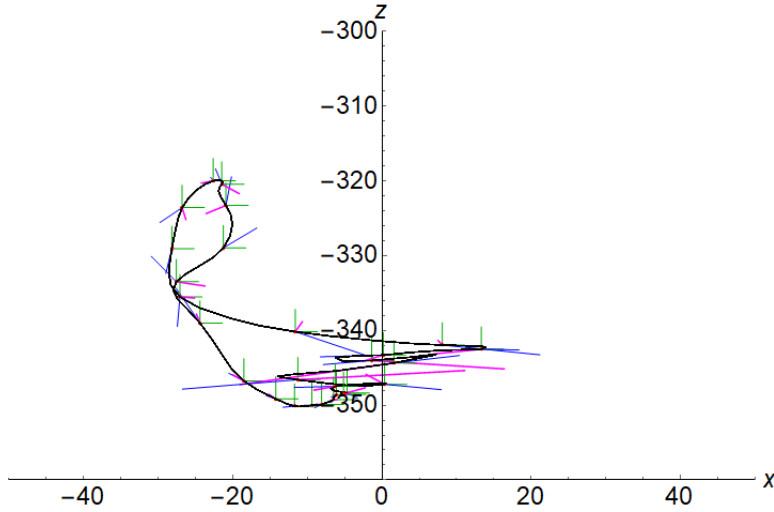


Figure 3.4: The various sets of kinematic specifications at the knee joint trajectory. Task positions are indicated with a coordinate frame, velocity specifications are indicated with blue, and acceleration is shown in magenta.

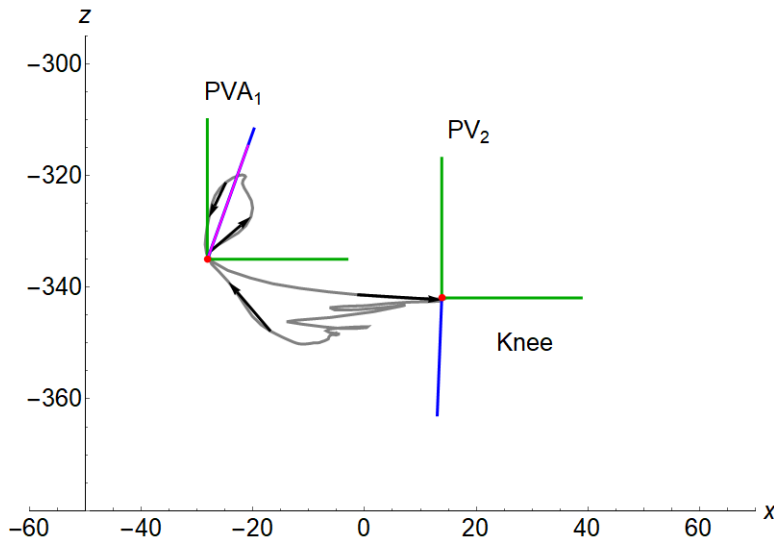


Figure 3.5: The selected kinematic specifications on the knee trajectory. Task positions are indicated with a coordinate frame, velocity specifications are indicated with blue, and acceleration is shown in magenta.

moves through the task positions,  $T_1 = (P_1, e^{i\theta_1}), T_2 = (P_2, e^{i\theta_2})$ , with velocity  $(\dot{P}_1, i\dot{\theta}_1 e^{i\theta_1})$  and acceleration  $(\ddot{P}_1, -\ddot{\theta}_1 e^{i\theta_1})$  defined at the  $j = 1$  position and only velocity  $(\dot{P}_2, i\dot{\theta}_2 e^{i\theta_2})$  at the  $j = 2$  position.

A four-bar linkage has three moving links  $OA, BC$  and  $ABP_1$ . The orientation of each link

Position	$(\theta_j, P_{jx}, P_{jy})$ ( $^\circ, mm, mm$ )	$(\dot{\theta}_j, \dot{P}_{jx}, \dot{P}_{jy})$ ( $^\circ/s, mm/s, mm/s$ )	$(\ddot{\theta}_j, \ddot{P}_{jx}, \ddot{P}_{jy})$ ( $^\circ/s^2, mm/s^2, mm/s^2$ )
1	(0, -28.17, -334.971)	(1, 0.33, 0.93)	(0, 0.29, 0.81)
2	(0, 13.81, -341.89)	(1, -0.03, -0.84)	-

Table 3.1: Task specifications for synthesis of four-bar knee linkage.

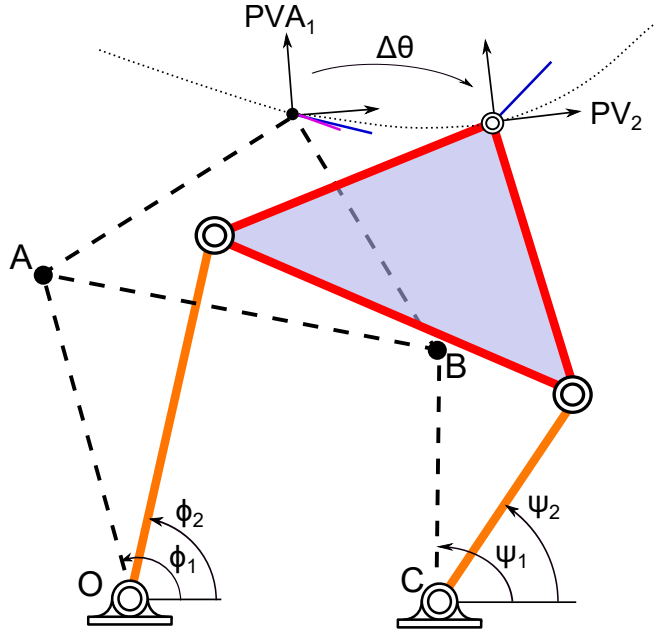


Figure 3.6: A four-bar linkage shown at the two tasks specified. The black frames indicate position specifications, blue lines denote velocity and magenta lines show the acceleration specification.

in the  $j^{th}$  position is measured by angles  $\phi_j$ ,  $\psi_j$ , and  $\theta_j$ , respectively. These three angles define complex rotation operators  $Q_j, S_j, T_j$ ,

$$Q_j = e^{i\phi_j}, \quad S_j = e^{i\psi_j}, \quad T_j = e^{i\theta_j}, \quad j = 1, 2. \quad (3.1)$$

The following two loop equations can be written for the four-bar linkage at each task position,

$$\begin{aligned} O + (A - O)Q_j + (P_1 - A)T_j - P_j &= 0, \\ C + (B - C)S_j + (P_1 - B) - P_j &= 0, \quad j = 1, 2. \end{aligned} \quad (3.2)$$

When  $j = 1$ , the loop equations degenerate to give  $0 = 0$ . The unknowns in Equation. 3.2 are  $O, A, B, C$  and  $Q_j, S_j$ . And the rotation operators  $Q_j$  and  $S_j$  must satisfy,

$$\begin{aligned} Q_j \bar{Q}_j &= 1, \\ S_j \bar{S}_j &= 1, \quad j = 1, 2 \end{aligned} \quad (3.3)$$

Appending the conjugate loop equations, we get:

$$\begin{aligned} \bar{O} + (\bar{A} - \bar{O})\bar{Q}_j + (\bar{P}_1 - \bar{A})\bar{T}_j - \bar{P}_j &= 0, \\ \bar{C} + (\bar{B} - \bar{C})\bar{S}_j + (\bar{P}_1 - \bar{B}) - \bar{P}_j &= 0, \quad j = 1, 2. \end{aligned} \quad (3.4)$$

This set of equations can be written as two independent systems of equations with the same structure in the unknowns,  $O, \bar{O}, A, \bar{A}, Q_j, \bar{Q}_j$  and  $C, \bar{C}, B, \bar{B}, S_j, \bar{S}_j$  respectively. Therefore, we only need to solve one of these systems, which is known as the synthesis equations for an 2R constraint.

The unknowns  $(Q_j, \bar{Q}_j)$  can be eliminated by utilizing the normalization condition  $Q_j \times \bar{Q}_j = 1$  to obtain,

$$(A_1 - O)(\bar{A}_1 - \bar{O}) = ((P_j - O) - (P_1 - A_1)T_j)((\bar{P}_j - \bar{O}) - (\bar{P}_1 - \bar{A}_1)\bar{T}_j), \quad j = 1, 2 \quad (3.5)$$

Combining two 2R constraints forms a four-bar linkage and provides a solution to the entire system. For case  $N = 2$ , it gives a single equation in four unknowns. Thus, we require 3 more equations to obtain an exact solution to this system. The time derivative of the 2R

constraint yields two velocity constraint equations,

$$\begin{aligned} & (-\dot{P}_j + i\dot{\theta}_j T_j(P_1 - A))((\bar{O} - \bar{P}_j) + \bar{T}_j(\bar{P}_1 - \bar{A})) \\ & + ((O - P_j) + T_j(P_1 - A))(-\dot{\bar{P}}_j - i\dot{\theta}_j \bar{T}_j(\bar{P}_1 - \bar{A})) = 0, \quad j = 1, 2 \end{aligned} \quad (3.6)$$

The time derivative of the velocity constraint yields a single acceleration constraint equation,

$$\begin{aligned} & (-\ddot{P}_j + i\ddot{\theta}_j T_j(P_1 - A) - \dot{\theta}_j^2 T_j(P_1 - A))((\bar{O} - \bar{P}_1) + \bar{T}_j(\bar{P}_1 - \bar{A})) \\ & + ((O - P_j) + T_j(P_1 - A))(-\ddot{\bar{P}}_j - i\ddot{\theta}_j \bar{T}_j(\bar{P}_1 - \bar{A}) + \dot{\theta}_j^2 \bar{T}_j(\bar{P}_1 - \bar{A})) = 0, \quad j = 1, 2 \end{aligned} \quad (3.7)$$

With the inclusion of the velocity and acceleration constraint equations, we now have a system of 4 equations in 4 unknowns,  $O, \bar{O}, A, \bar{A}$ , for two task positions, with two velocities and one acceleration specification. The analytical solution of the RR linkage design equations yield zero, two, or four sets of real values for the five design parameters for the chain that ensure that the floating link/knee joint moves through the task positions. When two of these chains are connected in parallel, in one of six possible ways, the workspace of the system reduces from two to one dimension to form a single degree of freedom 4R chain.

### 3.2.3 Synthesis Results

The synthesis process gives us a number of four-bar knee designs, of which we select the solutions that are compact, and have fixed pivots located behind the knee joint in a manner that they can be rigidly attached to the thigh of the individual. The chosen solutions for the simultaneous synthesis of two  $2R$  fingers are shown in Table 3.2. It yields an end-effector type device, as the coupler points guides the motion of the knee joint, but its pivots do not coincide with the anatomical position of the knee joint.

The four-bar linkage selected is shown in Figure. 3.7.

Solution	$O = (u, v)$	$A = (x, y)$
1	$(-77.46, -321.38)$	$(-98.73, -321.37)$
2	$(-16.83, -325.74)$	$(-38.27, -325.71)$

Table 3.2: The chosen solutions for the simultaneous synthesis of the two planar  $2R$  mechanical knee linkage.

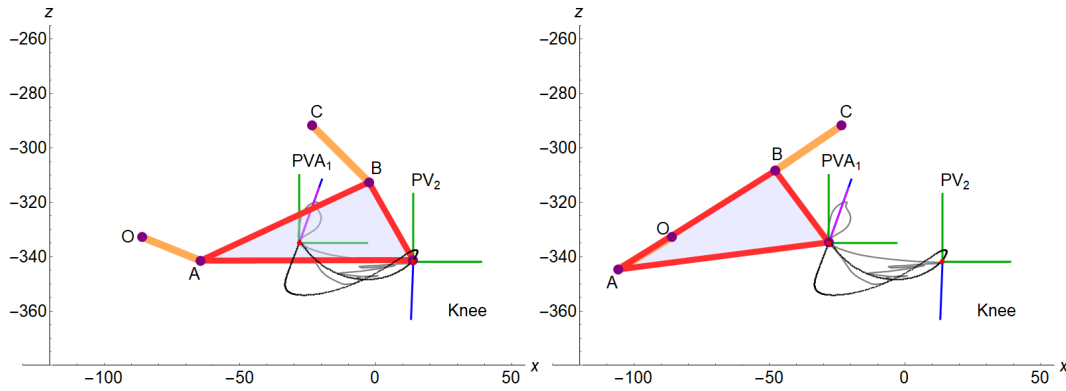


Figure 3.7: The synthesized four-bar linkage at the two task positions specified.

### 3.3 Multi-Axis Hands-free Crutch

The knee mechanism synthesized can be classified as an end-effector type device as per the classification scheme used in Chapter 1 (Figure. 3.8). A solid model schematic of the knee linkage attached to a Hands-free Crutch test bed is shown in Figure. 3.9. This device is christened as the Multi-axis Hands-free Crutch or MHC. Hands-Free Crutches (HFC) are devices that were introduced as alternatives to standard under-arm crutches for temporary lower leg injuries. They offer more freedom of movement, and reduce the discomfort in arms and shoulders experienced with use of under-arm crutches. Some popular commercial devices include FlexLeg and iWalk [95].

A full scale device prototype is manufactured, and is shown in Figure. 3.10.

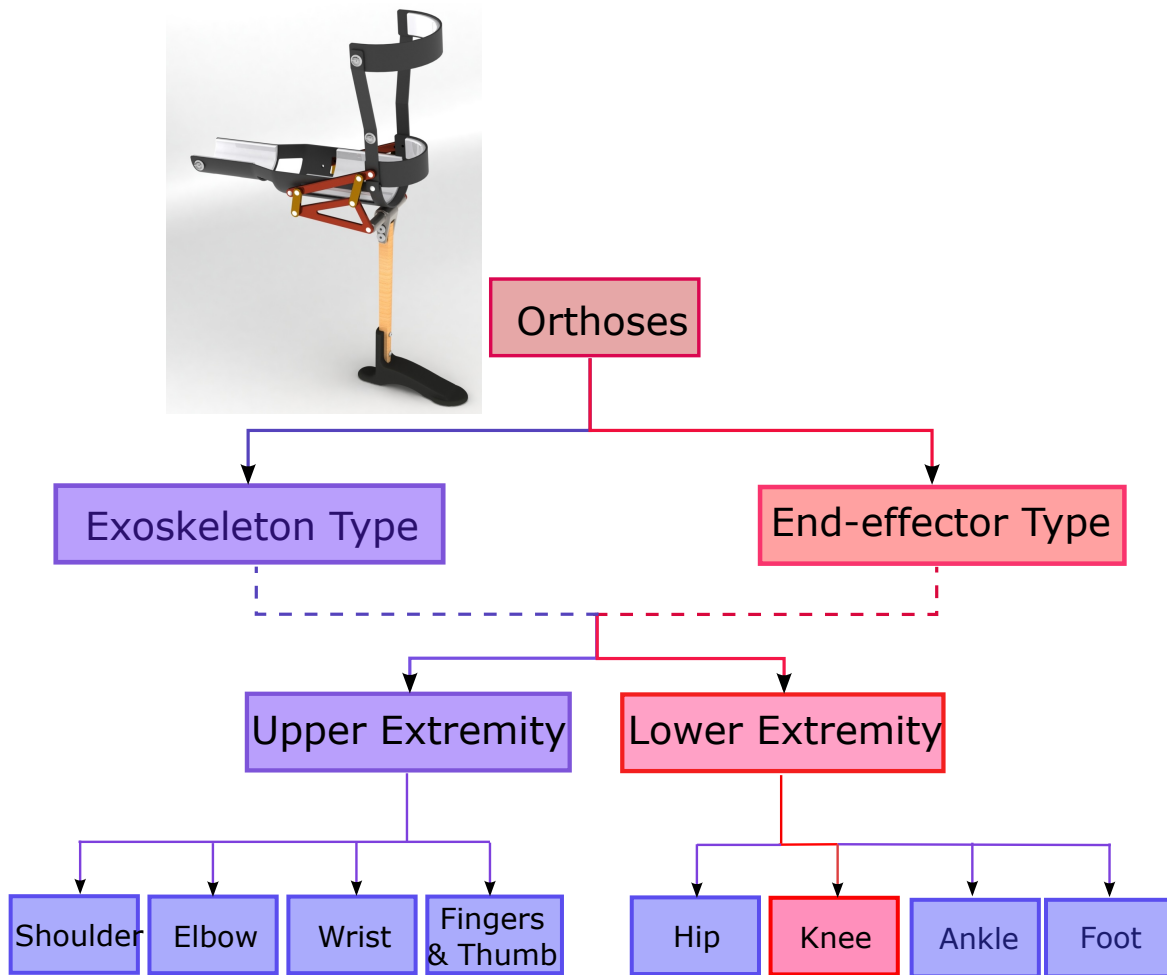


Figure 3.8: Classification of the individualized four-bar linkage based multi-axis hands-free crutch based on modality of providing assistance.

### 3.4 Pilot Study of Prototype & Results

In order to compare the knee linkage with natural walking motion as well as a locked knee device, the prototype MHC device is tested by one user walking on the level ground under the following conditions: (a) no assistance, (b) with the HFC, and (c) with the MHC, and their hip and knee heights and stride lengths are studied (Figures. 3.11 - 4.18).

Hip hiking when walking with a fixed-knee Hands-free Crutch was found to increase by 6.92 % of the hip height observed during walking normally overground. Walking with MHC reduces the amount of hip hiking to 2.81 % of normal walking.



Figure 3.9: Solid model of the fabricated four-bar linkage.



Figure 3.10: Full-scale prototype of the multi-axis hands free crutch.

Stride length during normal walking for the test subject is found to be 720 mm. Walking with the fixed-knee HFC reduces the stride length to 550 mm (76.39 % of normal walking). When walking with the MHC, the subject has a stride lengths of 618 mm (85.83 % of normal walking).

From Figure. 4.18, we can see that the knee height of a test subject walking with the MHC has similar motion profile as normal walking, but shows a vertical offset compared to the knee height observed when walking normally.

### 3.5 Summary

Through this work, we explore a design methodology which can be used to synthesize an individualized mechanical knee joint for a Hands-free Crutch device, which mimics natural knee movement in the sagittal plane. Starting from experimental data of the individual's lower-leg during normal walking, the proposed procedure finds a simple, compact four-bar linkage that is to be rigidly attached to the thigh of the user, and whose coupler point -

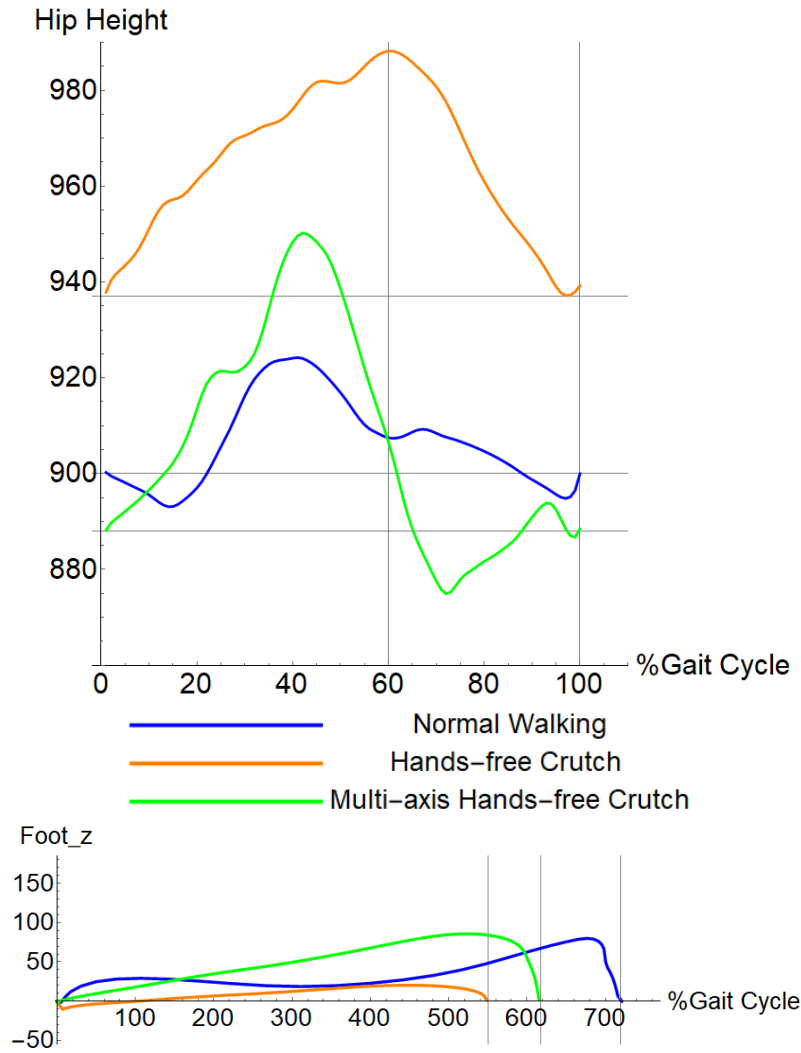


Figure 3.11: Gait Analysis of experimental data obtained from pilot test of walking with the MHC.

representing the instantaneous position of the knee joint - passes through the kinematic task positions specified.

A four-bar knee mechanism is synthesized and attached to a prototype of the MHC device. The MHC is tested by the individual by walking on level ground. Experimental data shows that the MHC decreases the lift at the hip associated with the Hands-free Crutch. It also increases the stride length compared to the Hands-free Crutch.

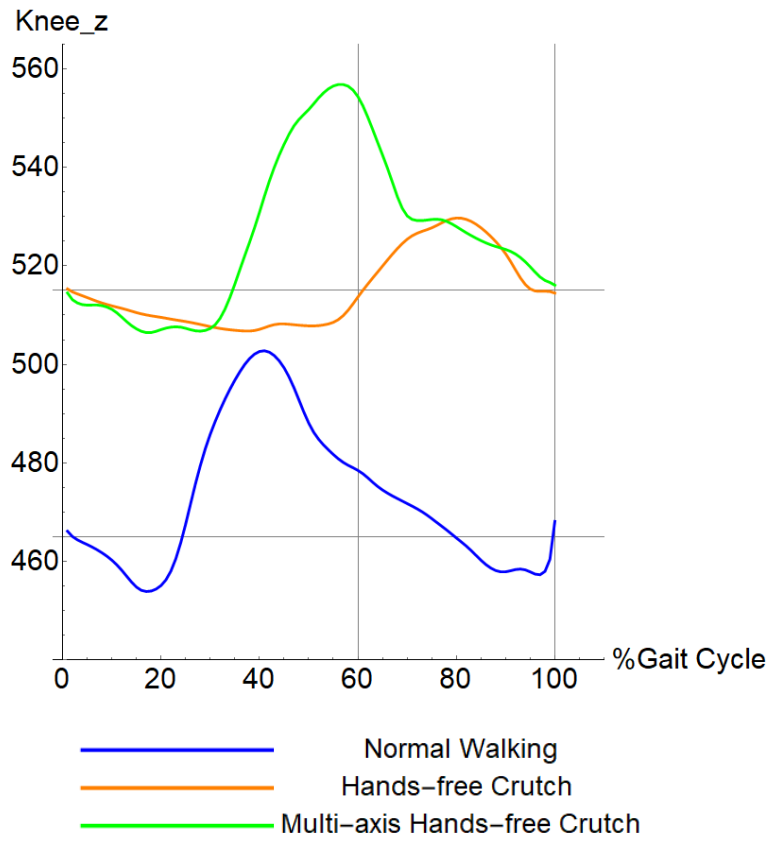


Figure 3.12: Comparison of knee height of the test subject walking normally, with a fixed-knee HFC, and with the MHC.

# Chapter 4

## Design of Knee-Ankle-Foot Orthosis based on Six-Bar Linkage

### 4.1 Introduction

A new procedure for synthesis of six-bar linkages that can coordinate the angular movement of the knee and ankle joints of an individual's leg is presented. The linkage is designed to have human-sized dimensions such that it can be adapted to the development of a wearable lower leg knee-ankle-foot orthosis.

Walking motion requires a complex coordination of hip, knee and ankle joint angles to produce the desired trajectory of the foot. While a four-bar knee mechanism can be synthesized to produce the trajectory traced by the knee joint, the limited number of structural design parameters of the four-bar are not sufficient to allow for the placement of the knee device coaxially with the anatomical knee joint axis of the human body.

A six-bar linkage based knee-ankle-foot orthosis allows the designer more control in placement

of fixed pivots and linkage body with respect to the user's leg to avoid collisions between the various components of the device, the device body, and with the human limb. Orthoses that guide complex biological motions can be programmed more successfully using six-bar linkages as they have more design parameters, and can coordinate more precision points on a given trajectory.

In this chapter we present the kinematic synthesis of an exoskeleton type knee-ankle-foot-orthosis using the individual motion data for an individual

## **4.2 Design Procedure**

### **4.2.1 Individualized Task specifications based on Lower-leg Motion Capture Data**

In order to study the motion of the knee and ankle joints, with respect the thigh, we define relative coordinate frames on each of the body segments, namely, the trunk, thigh, shank and foot. The two-dimensional embedded coordinate frames are defined such that the Z-axis points upwards along the segment, and X-axis is perpendicular to it and points to the right. The recorded data is then transformed relative to the new fixed frame embedded in the thigh segment, and Fig. 4.1 shows the trajectory traced by the third metatarsal bone in the left foot relative to the fixed thigh frame.

In gait analysis, in order to study joint motion, each distinct body segment is modeled as a rigid body and the relative rotations are assumed to take place about a fixed point in the proximal segment, which is considered to be the center of the joint. At each of the joints, flexion-extension is assumed to be the most important rotation, as the major motion occurs in the sagittal plane. A representative pattern of motion data of the knee and ankle joint

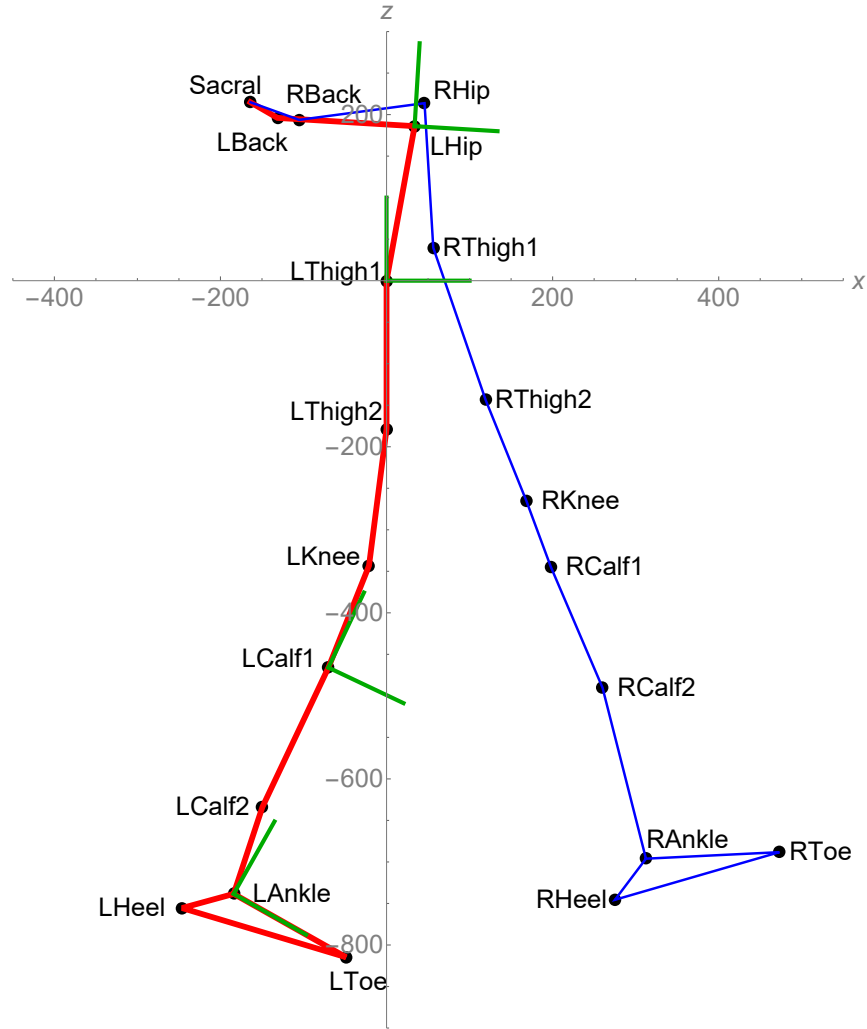


Figure 4.1: The lower leg transformed in the sagittal plane when the thigh is held stationary.

angular motions for the individual is found by averaging over seven gait cycles, and is shown in Figures. 4.2 4.3. The knee joint is almost in full extension at heel strike and then flexes to about  $20^\circ$  during loading response. It then extends until toe-off occurs, after which it starts to flex again to reach about  $60^\circ$  in flexion at the end of initial swing. During terminal swing, the knee extends again to prepare for the next heel strike.

The orthopedic knee and ankle angles specify the relative orientation of the shank and the foot with respect to the previous body segment, i.e. the thigh and the shank respectively. Since the orthopedic angles specify the relative orientation of the distal moving segment with respect to the proximal reference frames, the corresponding rotational matrix can be

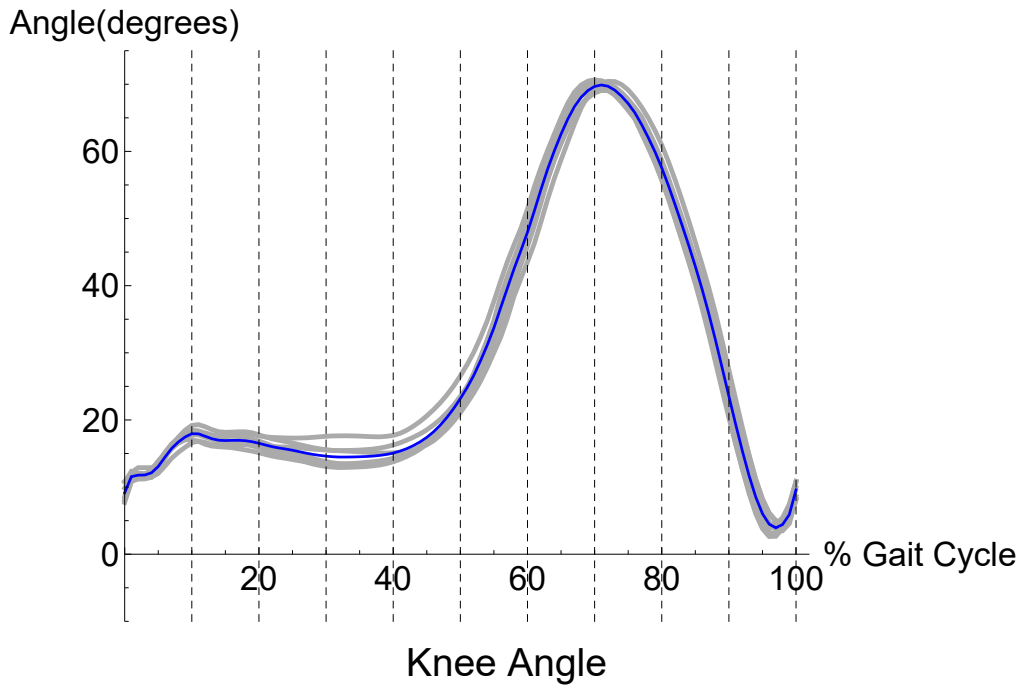


Figure 4.2: Knee joint angle variation over a complete gait cycle, beginning and ending at heel strike. Gray lines indicate knee angles calculated for a single gait cycle, and blue line indicates the average knee angle obtained from the motion data over seven gait cycles.

derived in terms of these angles. From the recorded data, we obtain a  $66.18^\circ$  average range of motion (ROM) at the knee joint during normal walking and a  $22.41^\circ$  average ankle joint ROM.

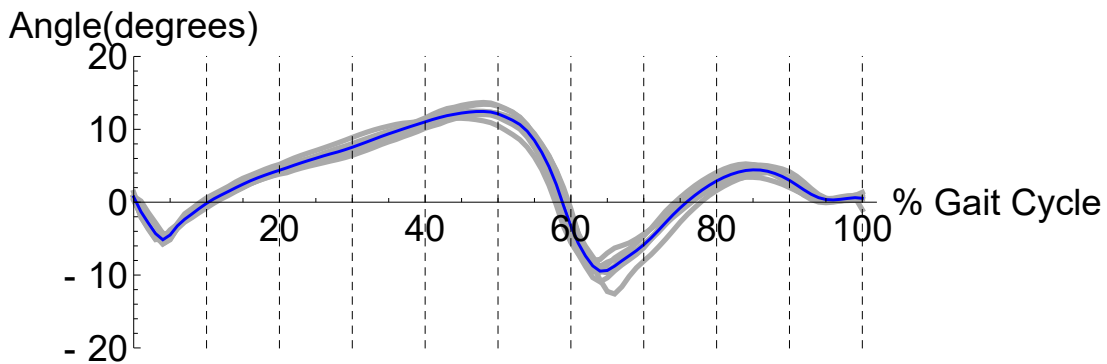


Figure 4.3: Ankle joint angle variation over a complete gait cycle, beginning and ending at heel strike. Gray lines indicate ankle angles calculated for a single gait cycle, and blue line indicates the average ankle angle obtained from the individual's motion data over seven gait cycles.

By approximating the knee and ankle joints with single revolute joints in the sagittal plane,

the human lower-leg is kinematically modeled by a serial 2R chain as shown in 4.4. The fixed pivot  $B$  of the 2R chain represents the knee joint, and the moving pivot  $F$  represents the ankle joint. The dimensions of the links of the 2R chain are obtained from the motion capture data of the subject and are presented in Table 4.1.

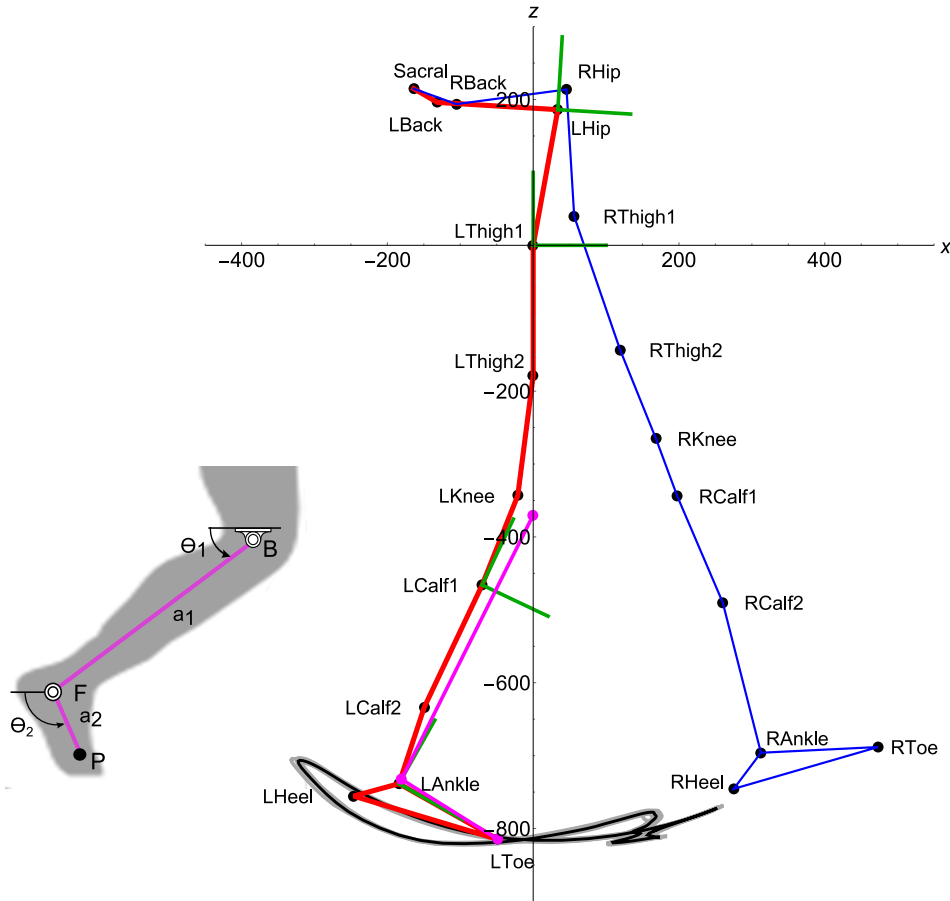


Figure 4.4: Kinematic model of the lower leg in the sagittal plane when the thigh is held fixed. The curve traced by the LToe marker gives the metatarsal trajectory with respect to a thigh fixed frame.

B (mm)	F (mm)	$a_1$ (mm)	$a_2$ (mm)
(0, -370)	(-180.56, -732.53)	405	155

Table 4.1: Selected pivot positions and dimensions for the 2R lower-leg kinematic model at the beginning of the cycle.

The point  $P$ , located at the head of the third metatarsal bone, can be expressed using

complex number notation based on the lower-leg kinematic model as:

$$P = B + a_1 e^{i\theta_1} + a_2 e^{i\theta_2} \quad (4.1)$$

Where,

$$B = B_x + iB_y$$

$$P = P_x + iP_y$$

If the position of the metatarsal, i.e. point  $P$  is known, the absolute joint angles  $\theta_1$  and  $\theta_2$  can be calculated as follows:

$$e^{i\theta_1} = \frac{1}{2a_1(\bar{P} - \bar{B})} \left( (P - B)(\bar{P} - \bar{B}) + a_1^2 - a_2^2 - \sqrt{((P - B)(\bar{P} - \bar{B}) + a_1^2 - a_2^2)^2 - 4a_1^2(P - B)(\bar{P} - \bar{B})} \right) \quad (4.2)$$

$$e^{i\theta_2} = \frac{a_2}{(\bar{P} - \bar{B} - a_1 e^{-i\theta_1})}$$

The absolute angles  $\theta_1$  and  $\theta_2$  are related to the orthopedic knee angle and ankle angles as:

$$\text{Knee Angle} = \theta_1 - \pi/2$$

$$\text{Ankle Angle} = \theta_2 - \theta_1 \quad (4.3)$$

This formulation allows us to specify the knee and ankle angular movements for any given point on the metatarsal trajectory, in order to synthesize an individualized exoskeleton type linkage that will allow us to guide the motions of the knee and ankle joints during walking. The synthesis formulation and solution of generic six-bar function generators is described in depth in Plecnik and McCarthy [72]. Plecnik and McCarthy [71] also presented an algebraic synthesis technique for the design Stephenson II six-bar function generators that can coordinate 11 input and output angles of a 2R serial chain. This Stephenson II function

generator can then be scaled and transformed to yield a Stephenson III path generator, with the coupler point  $P$  on the ternary link  $FHP$  as shown in Figure 4.5.

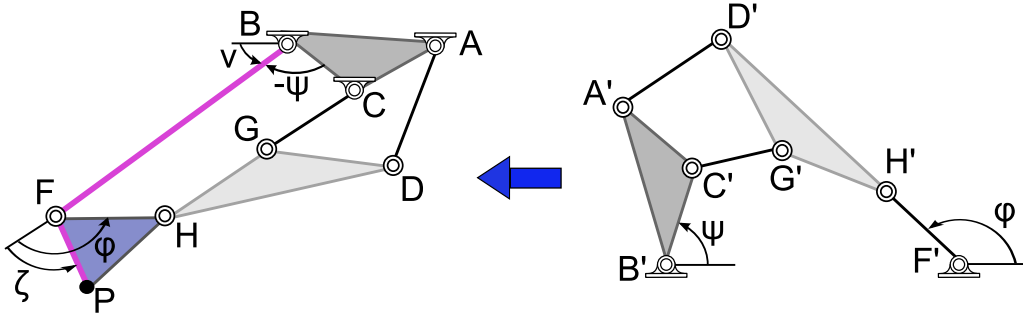


Figure 4.5: A Stephenson III path generator obtained by coordinating the RR joints with a Stephenson II function generator (adapted from [96]).

Solving the inverse kinematics of the 2R lower-leg chain yields angles  $\nu$  and  $\zeta$  shown in Figure. 4.5 as:

$$\begin{aligned} -\nu &= -\theta_1 \\ \zeta &= \theta_2 - \theta_1 + \alpha \end{aligned} \tag{4.4}$$

The angles  $\nu$  and  $\zeta$  are related to the angles  $\psi$  and  $\phi$ , which are the input and output angles for the Stephen II six bar function generator as:

$$\begin{aligned} \psi &= -\nu = -\theta_1 \\ \phi &= \zeta + \alpha = \theta_2 - \theta_1 + \alpha \end{aligned} \tag{4.5}$$

Where,  $\alpha$  is a constant angle.

Eleven points are selected on the metatarsal trajectory such that the 2R chain traces the specified metatarsal trajectory closely as shown in Figure 4.6(a). As the 2R chain  $BFP$  moves through the eleven points,  $P_j, j = 1, \dots, 11$ , along the target walking trajectory we obtain a set of coordinated knee and ankle joint angles ( $\nu$  and  $\zeta$ ) using the inverse kinematics equations shown in Equations. 4.2 and 4.4. Then  $\Delta\psi_k = \psi_k - \psi_0$  and  $\Delta\phi_k = \phi_k - \phi_0$  are

calculated using Equation. 4.5, which eliminates the constant angle  $\alpha$  as:

$$\Delta\psi_k = -\Delta\nu_k = -\Delta\theta_1 \quad (4.6)$$

$$\Delta\phi_k = \Delta\zeta_k = \Delta(\theta_2 - \theta_1) \quad k = 1, \dots, 10$$

These set of angles  $\Delta\psi$  and  $\Delta\phi$  are used for the design of the Stephenson II function generator that will be used to design the wearable lower-leg exoskeleton type orthosis. These sets of angles obtained for 11 task positions of the 2R chain shown in Figure 4.6(b) and detailed in Table 4.2.

Task Pos. #	P (mm)	$\Delta\nu$ (rad)	$\Delta\zeta$ (rad)	$\Delta\psi$ (rad)	$\Delta\phi$ (rad)
1	(155.56, -799.66)	-1.56	1.40	0	0
2	(165.21, -774.79)	-1.55	1.55	-0.02	0.14
3	(67.46, -797.2)	-1.78	1.58	0.22	0.17
4	(-49.03, -814.55)	-2.03	1.48	0.47	0.07
5	(-162.88, -809.67)	-2.25	1.31	0.69	-0.09
6	(-256.86, -763.49)	-2.47	1.31	0.91	-0.10
7	(-326.33, -697.47)	-2.69	1.36	1.12	-0.04
8	(-163.13, -781.99)	-2.30	1.50	0.74	-0.10
9	(38.50, -816.88)	-1.84	1.47	0.27	0.06
10	(141.99, -808.93)	-1.59	1.37	0.03	-0.03
11	(229.62, -783.63)	-1.38	1.28	-0.18	-0.12

Table 4.2: Coordinates of point P on the 2R backbone chain at the task positions selected for synthesis task, and the corresponding values of  $\Delta\nu$  and  $\Delta\zeta$ , the input and output of the 2R serial chain and,  $\Delta\psi$  and  $\Delta\zeta$ , the input and output angles of the Stephenson II function generator. .

## 4.2.2 Kinematic Synthesis of Six-bar Knee-Ankle-Foot Orthosis

In this section we briefly discuss the synthesis of a Stephenson II six-bar function generator for the 11 accuracy points specified in the previous subsection following the technique introduced by Plecnik and McCarthy [72].

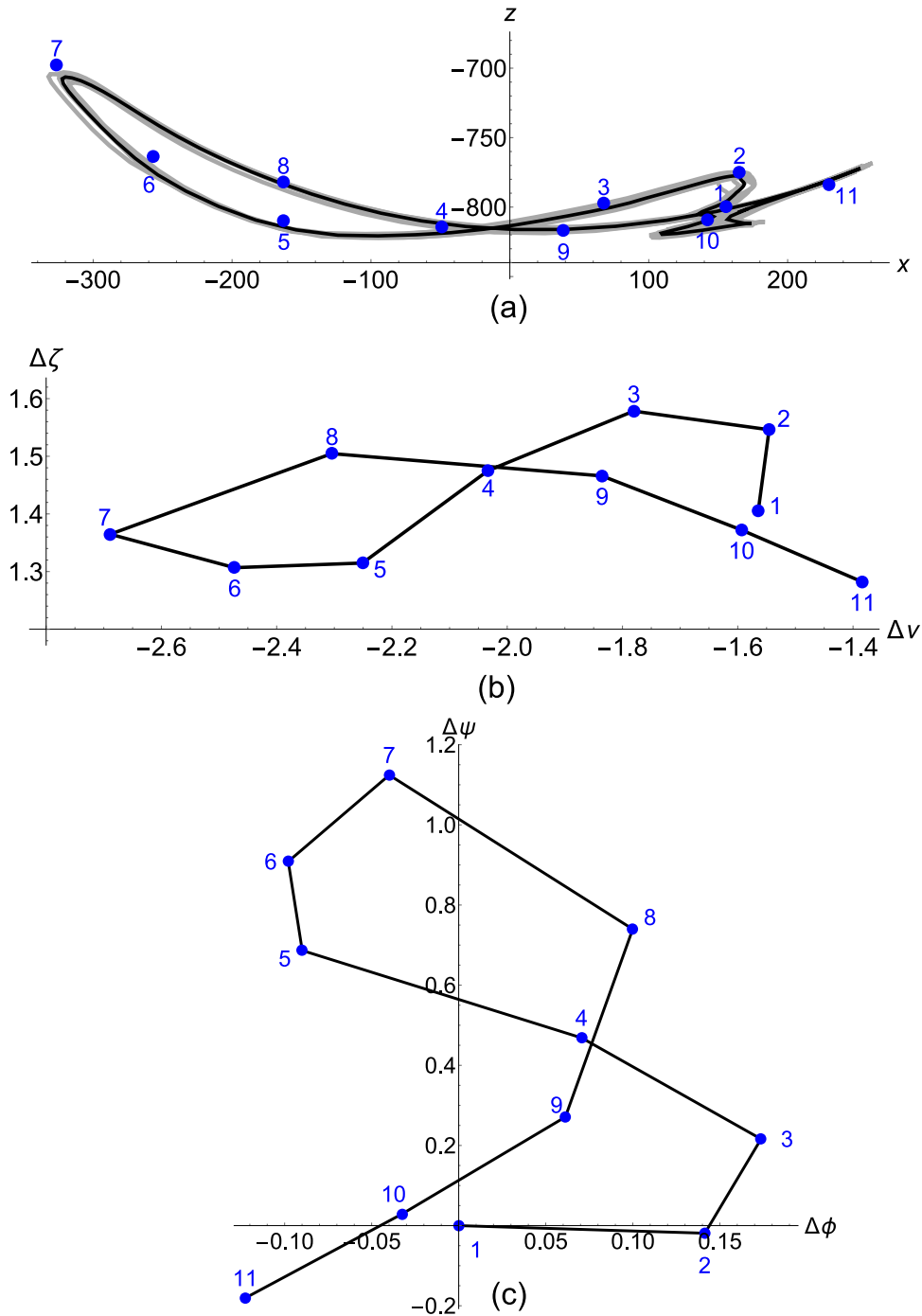


Figure 4.6: (a) Eleven specified task points on the foot trajectory, (b) The function between  $\nu$  and  $\zeta$ , the input and output of the 2R serial chain (c) The function between  $\psi$  and  $\zeta$ , the input and output angles of the Stephenson II function generator.

A Stephenson II linkage is shown in Figure 4.7. The coordinates of the seven revolute joints of the linkage are defined by complex vectors  $A$ ,  $B$ ,  $C$ ,  $D$ ,  $F$ ,  $G$  and  $H$ . Relative orientations

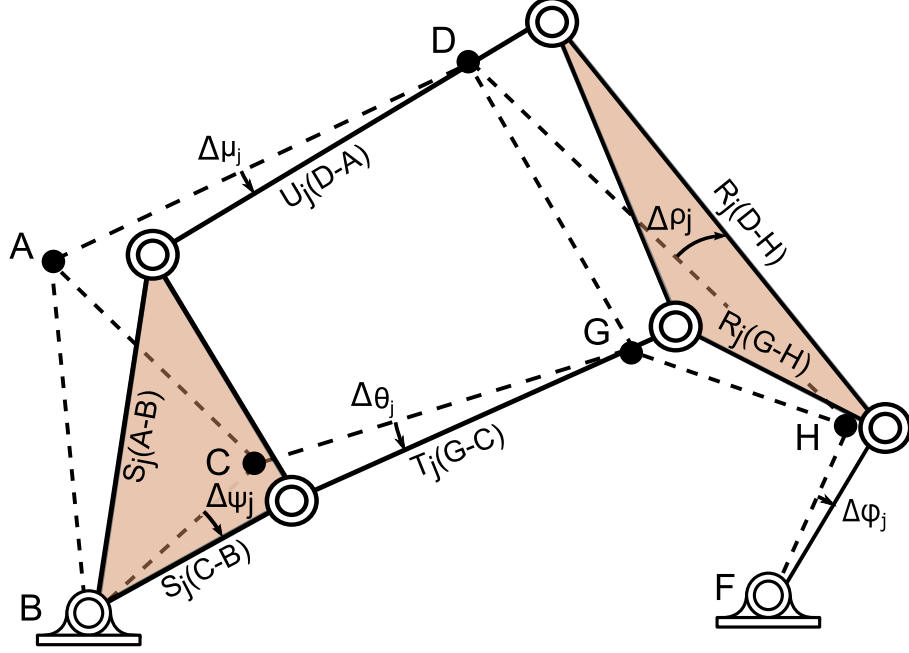


Figure 4.7: Stephenson II six bar linkage (adapted from [71]).

of the moving links are measured from the reference position to the configuration of the linkage at the  $j^{\text{th}}$  point, and are given by  $\Delta\phi_j = \phi_j - \phi_0$ ,  $\Delta\rho_j = \rho_j - \rho_0$ ,  $\Delta\psi_j = \psi_j - \psi_0$ ,  $\Delta\theta_j = \theta_j - \theta_0$  and  $\Delta\mu_j = \mu_j - \mu_0$ , where  $j = 0, \dots, 10$ . The objective is to find pivot locations to coordinate input angles  $\Delta\psi_j$  and output angles  $\Delta\phi_j$  at the  $j = 0, \dots, 10$  points selected by the user (enumerated in Table 4.2).

The ground pivots  $B$  and  $F$  become the first link of the  $2R$  backbone chain as shown in Figure 4.5, hence their position is known and specified by the designer based on experimental data. Pivot positions  $A$ ,  $C$ ,  $D$ ,  $G$  and  $H$  are to be determined.

In the  $j^{\text{th}}$  configuration, the complex rotation operators can be defined as:

$$\begin{aligned}
 Q_j &= e^{i\Delta\phi_j} & S_j &= e^{i\Delta\psi_j} \\
 R_j &= e^{i\Delta\rho_j} & T_j &= e^{i\Delta\theta_j} \\
 U_j &= e^{i\Delta\mu_j} & & j = 1, \dots, 10
 \end{aligned} \tag{4.7}$$

The two complex loop equation for the Stephenson II six bar linkage are:

$$\begin{aligned}
L_j : T_j(G - C) &= [F + Q_j(H - F) + R_j(G - H)] - [B + S_j(C - B)] \\
M_j : U_j(D - A) &= [F + Q_j(H - F) + R_j(D - H)] - [B + S_j(A - B)] \\
j &= 1, \dots, 10
\end{aligned} \tag{4.8}$$

And the associated complex conjugate loop equations are:

$$\begin{aligned}
\bar{L}_j : \bar{T}_j(\bar{G} - \bar{C}) &= [\bar{F} + \bar{Q}_j(\bar{H} - \bar{F}) + \bar{R}_j(\bar{G} - \bar{H})] - [\bar{B} + \bar{S}_j(\bar{C} - \bar{B})] \\
\bar{M}_j : \bar{U}_j(\bar{D} - \bar{A}) &= [\bar{F} + \bar{Q}_j(\bar{H} - \bar{F}) + \bar{R}_j(\bar{D} - \bar{H})] - [\bar{B} + \bar{S}_j(\bar{A} - \bar{B})] \\
j &= 1, \dots, 10
\end{aligned} \tag{4.9}$$

The normalization conditions for complex operators:

$$\begin{aligned}
R_j \bar{R}_j &= 1 \\
U_j \bar{U}_j &= 1 \\
T_j \bar{T}_j &= 1 \quad j = 1, \dots, 10
\end{aligned} \tag{4.10}$$

Equations. (4.8, 4.9, 4.10), together form the synthesis equations for the Stephenson II function generator. For 11 accuracy points represented by configurations  $j = 0, \dots, 10$ , we get 70 equations in 70 unknowns, which can be reduced to a set of equations of degree 8 in 10 design parameters formed by  $A, C, D, G, H$  and  $\bar{A}, \bar{C}, \bar{D}, \bar{G}, \bar{H}$ . The total degree of the polynomial system is  $8^{10} = 1.07 \times 10^9$ . The general synthesis equations are solved by Plecnick and McCarthy [72] using regeneration homotopy method with the software package BERTINI [97]. The time required to solve the specific synthesis equations is 2 hours, 14 minutes and 21 seconds on a single node of UC Irvine's High Performance Computing cluster. Parallel processing was used with 64 CPUs at a speed of 2.2 GHz for each core and 332 solution

candidates are obtained. BERTINI returned 7867 solutions that correspond to physical linkages, of which 3644 unique solutions were constructed after removal of very large and very small link lengths. Of these, none pass through all 11 task positions specified, nine pass through ten of the specified positions and 90 design candidates pass through nine of the specified positions, and 233 linkages pass through eight of the specified positions.

### 4.2.3 Synthesis results

Of the 332 linkages obtained, none pass through all the 11 task points. However, nine linkage solutions pass through ten of 11 specified precision points. The precision point that is not reached by any linkage is number 11, which results in a reduction of the knee extension right before heel strike occurs by  $3.28^\circ$ , or 5.62% of the  $58.3^\circ$  joint ROM of the knee during walking. However, this region of the metatarsal trajectory corresponds to a hyperextension of the knee joint of the 2R lower-leg kinematic chain, hence this task position is ignored in the future. Only six linkages (five going through ten positions, and one going through nine positions) are found to be free of order defect, i.e. they go through the specified task positions in the order specified. The pivot locations of these six solutions are presented in Tables. 4.3 - 4.5 and the linkage structures are shown in Figures. 4.8 - 4.10.

Design Parameters	Design Candidate # I	Design Candidate # II
A	(- 35.05, -361.37)	(-5.058, -361.37)
B	(0, -370)	(0, -370)
C	(55.98, -345.67)	(57.86, -717.25)
D	(3.54, -342.59)	(-106.57, -719.459)
F	(-180.558, - 732.524)	(-180.558, - 732.524)
G	(-91.63, -368.68)	(-19.67,-866.22)
H	(-67.99, -700.67)	(-67.99,-700.67)

Table 4.3: Design parameters for Design Candidates I & II (all pivot locations are given in mm).

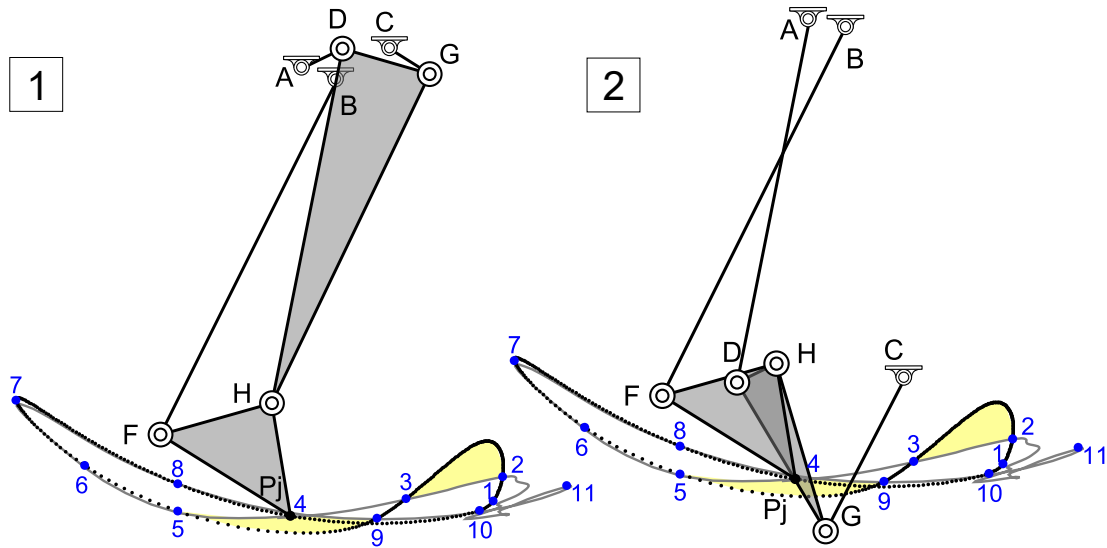


Figure 4.8: Design candidates I & II.

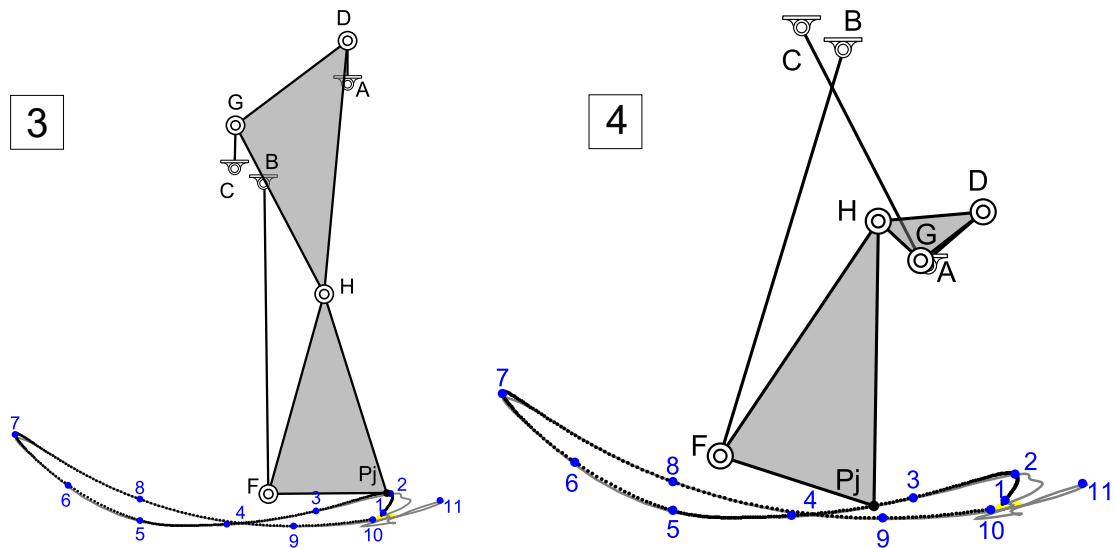


Figure 4.9: Design candidates III & IV.

On observing the angular movement at the knee and ankle joints obtained by these six design candidates, we find that design candidate number 1, 2 and 5 match the specified angular motion well, but have regions that diverge from the ideal metatarsal trajectory (marked in yellow in Figures. 4.8 - 4.10). Candidates 3 and 4 do not have continuous cyclic motion, hence are not suitable for development of the knee-ankle-foot orthosis. Only candidate 6 is free from these defects, however, linkage number 1 shows better angular movement.

Design Parameters	Design Candidate # III	Design Candidate # IV
A	(108.8, -235.38)	(79.51,-57.85)
B	(0, -370)	(0, -370)
C	(-38.95,347.93)	(-38.95,-347.93)
D	(57.5,-219.78)	(111.71, -505.47)
F	(-180.558, - 732.524)	(-180.558, - 732.524)
G	(-90.91, -327.86)	(73.37,-570.75)
H	(21.4,-550.68)	(21.4, -550.68)

Table 4.4: Design parameters for Design Candidates III & IV (all pivot locations are given in mm).

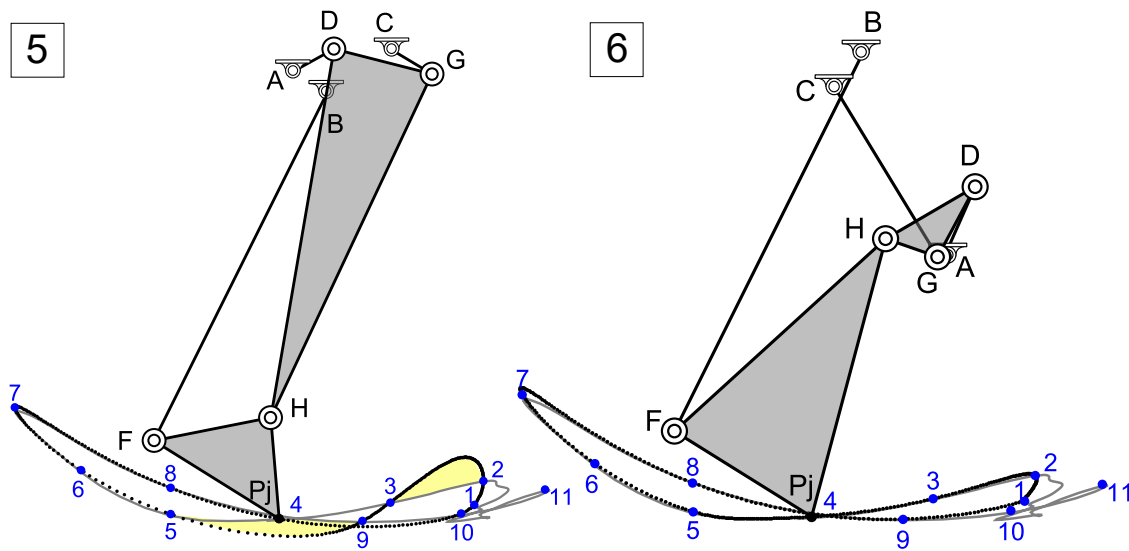


Figure 4.10: Design candidates V & VI.

Design Parameters	Design Candidate # V	Design Candidate # VI
A	(-33.11, -344.42)	(78.35, -564.92)
B	(0, -370)	(0, -370)
C	(71.5, -323.96)	(-24.94, -406.09)
D	(8.56, -321.57)	(107.93, -497.94)
F	(-180.558, - 732.524)	(-180.558, - 732.524)
G	(111.24, -347.77)	(71.85, -565.28)
H	(-57.84, -708.15)	(22.13, -547.96)

Table 4.5: Design parameters for Design Candidates V & VI (all pivot locations are given in mm).

Thus, design solution I is chosen for the development of the KAFO. This design candidate in addition to matching the desired knee and ankle trajectory closely, is also compact and has an anthropomorphic appearance. This linkage is able to produce the desired angles at the knee and ankle joints, however the coupler curve deviates from the desired metatarsal trajectory during the stance phase.

### 4.3 Knee-Ankle-Foot Orthosis Prototype

Once the linkage design is selected, we adapt it to the design of a lower-leg orthosis. A solid model of the six-bar linkage based individualized knee-ankle-foot orthosis is shown in figure. 4.11.

Using the classification scheme presented in Chapter 1, this device is classified as an end-effector type orthosis (Figure. 4.12).

To adapt the planar six-bar linkage to the design of a wearable device, the 2R chain that kinematically models the lower-leg of the user is replaced by the human's shank and foot. In order to increase stability of the wearable device, a copy of this 2R chain (marked as '1' in Figure. 4.13) is placed on the radial side of the person's leg. The pivots  $B$  and  $F$  are co-located with the anatomical joint axes of the human's knee and ankle joints by attaching them to a knee brace (marked as '4' in Figure. 4.13) and a boot (marked as '5' in Figure. 4.13) respectively. The chosen design makes the device safer to walk with by rigidly attaching it to the thigh and the shank via the knee brace with velcro straps. The knee brace provides additional support due to its rigid metallic body.

The two ternary links ('2' and '3' in Figure. 4.13) are designed to provide maximum support and rigid guidance with minimum material usage to reduce the weight of the KAFO designed (Figure. 4.14).

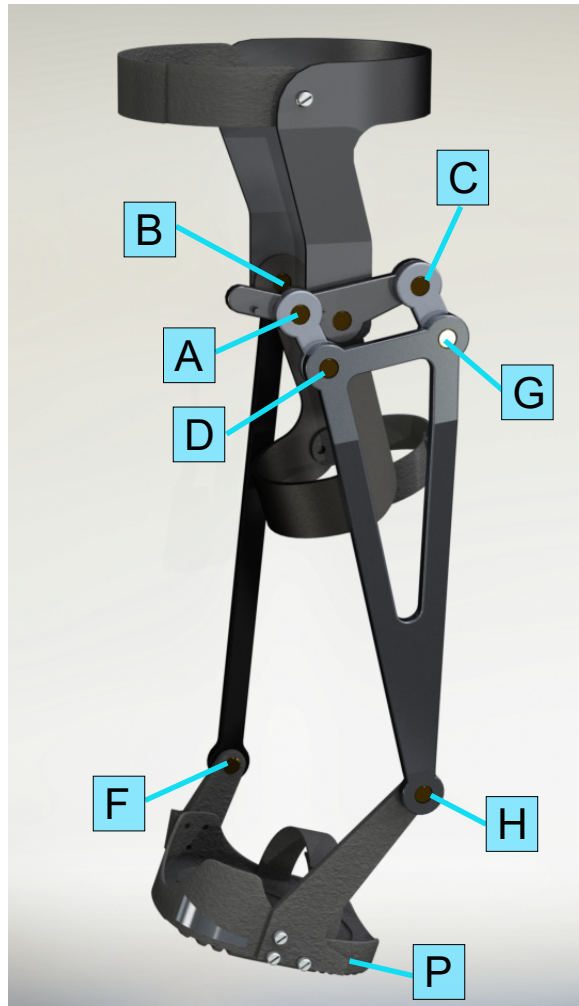


Figure 4.11: A solid model of the individualized six-bar linkage based knee-ankle-foot orthosis. The locations of the pivots of the six-bar linkage are indicated.

Finally, during the design phase the motion of the foot from the ankle to the 1st metatarsal bone is approximated. The toes cannot be approximated as a rigid body during the walking motion as they flex. In order to allow for this degree of freedom, a boot with soft inner sleeve is used to hold the foot.

A reduced scale of the orthotic device is 3-D printed to test the design (see Figure 4.15), and a full scale prototype is manufactured (Figure. 4.16).

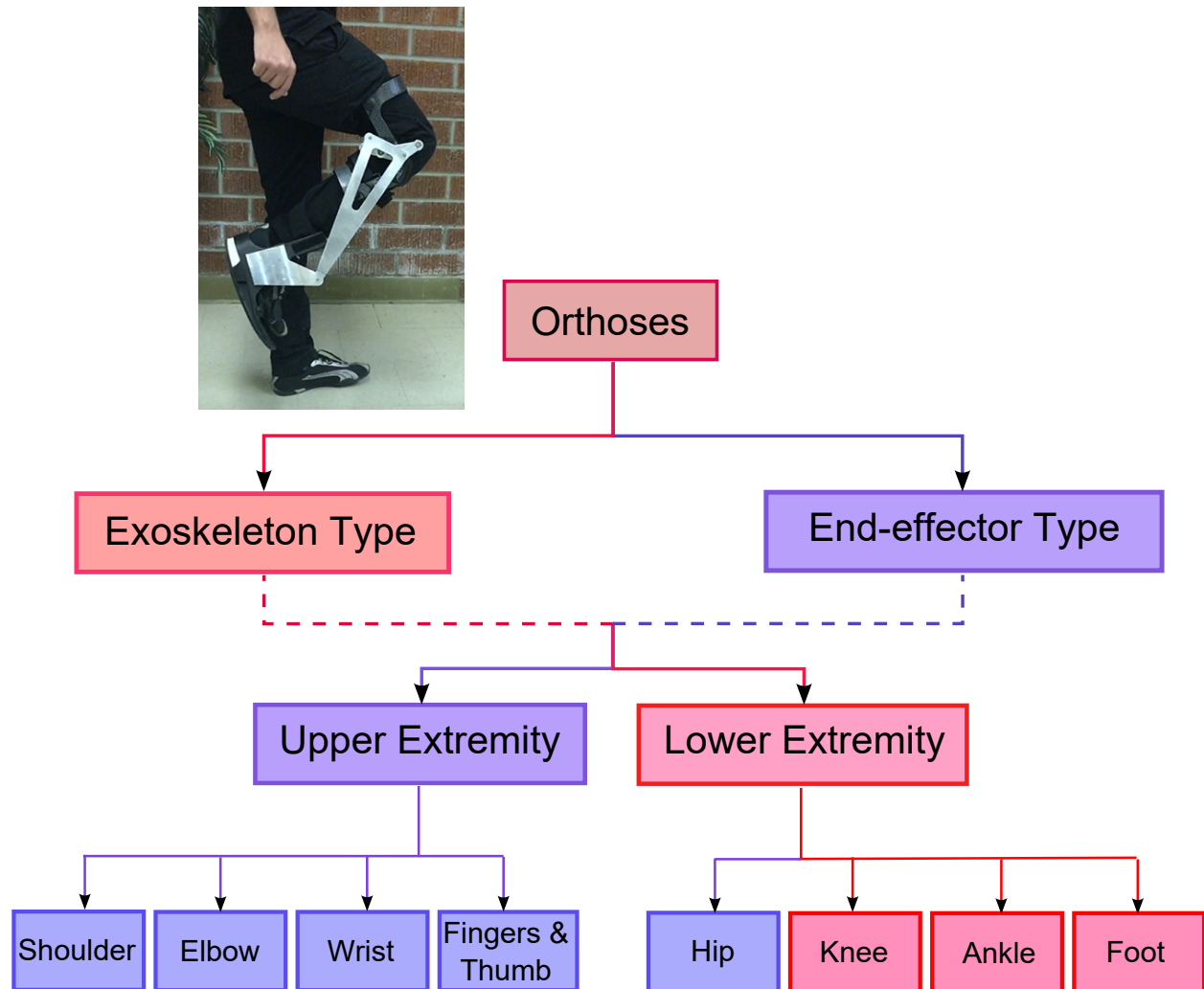


Figure 4.12: Classification of the individualized six-bar linkage based knee-ankle-foot orthosis based on modality of providing assistance.

## 4.4 Pilot Study of Prototype & Results

A single healthy male subject participated in the pilot study. The subject's right leg was securely placed and fastened into the KAFO prototype. A training and adjustment period of one hour was provided to the subject to become accustomed to walking with the KAFO. The subject then walked on the ground at a speed of 0.4 m/s, and motion capture data was collected.

Figure. 4.17, 4.18, 4.19 illustrate the healthy subject's knee and ankle movement as well

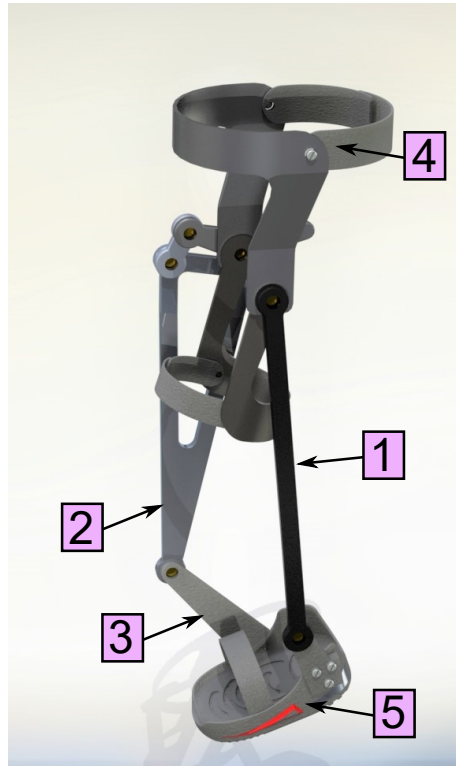


Figure 4.13: The components of the individualized knee-ankle-foot orthosis designed based on a planar six-bar linkage.

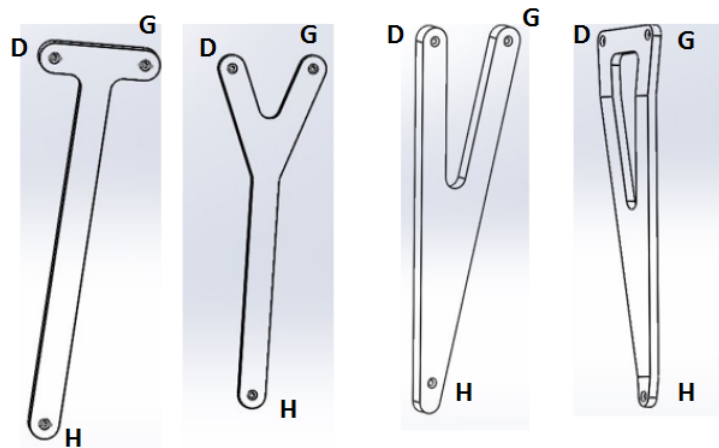


Figure 4.14: Evolution of design of link  $DGH$ .

as trajectory traced by their foot over the entire gait cycle under the following conditions: natural unassisted walking, prediction from kinematic model, and motion capture data of a person walking with the KAFO prototype. The kinematic model predicted close match between the knee and ankle joints, and a small deviation in the metatarsal trajectory. The



Figure 4.15: Reduced scale 3D printed model of the orthotic device.



Figure 4.16: Full scale prototype of the KAFO device.

experimental data of walking with the device shows that the knee joint follows the prescribed angular motion, and there are no significant differences between knee joint angle observed with and without the device. However, at the ankle joint plantarflexion increases by  $20^\circ$ , and dorsiflexion increases by  $7^\circ$  compared to predictions for the design. Stride length with

prototype is 97% of natural walking.

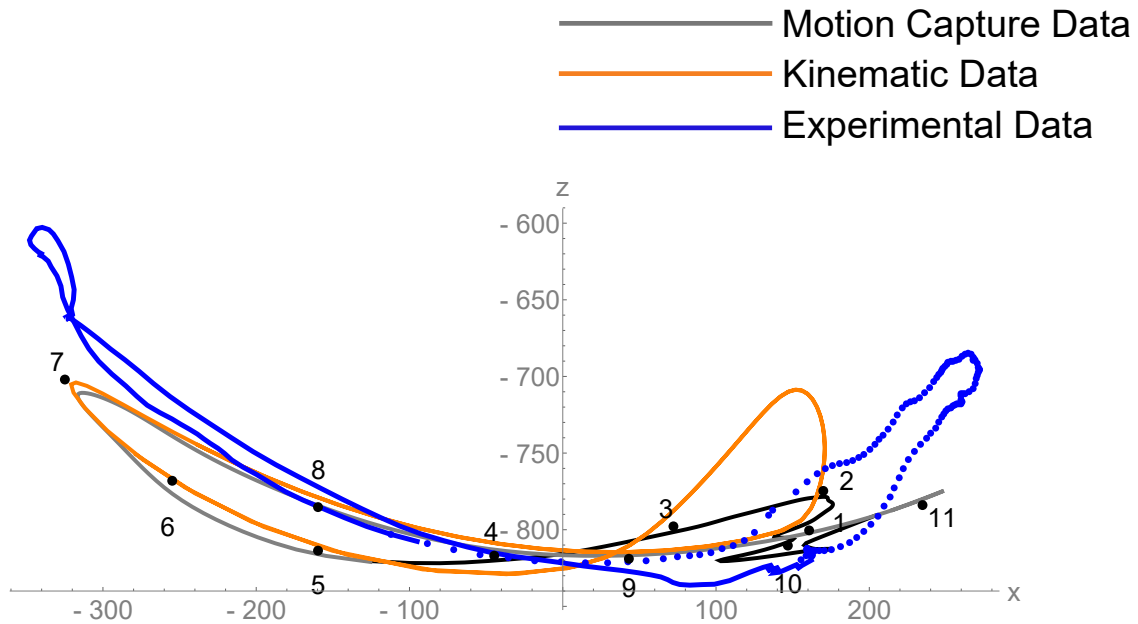


Figure 4.17: Metatarsal trajectory of a healthy subject walking with and without the KAFO device compared to design predictions.

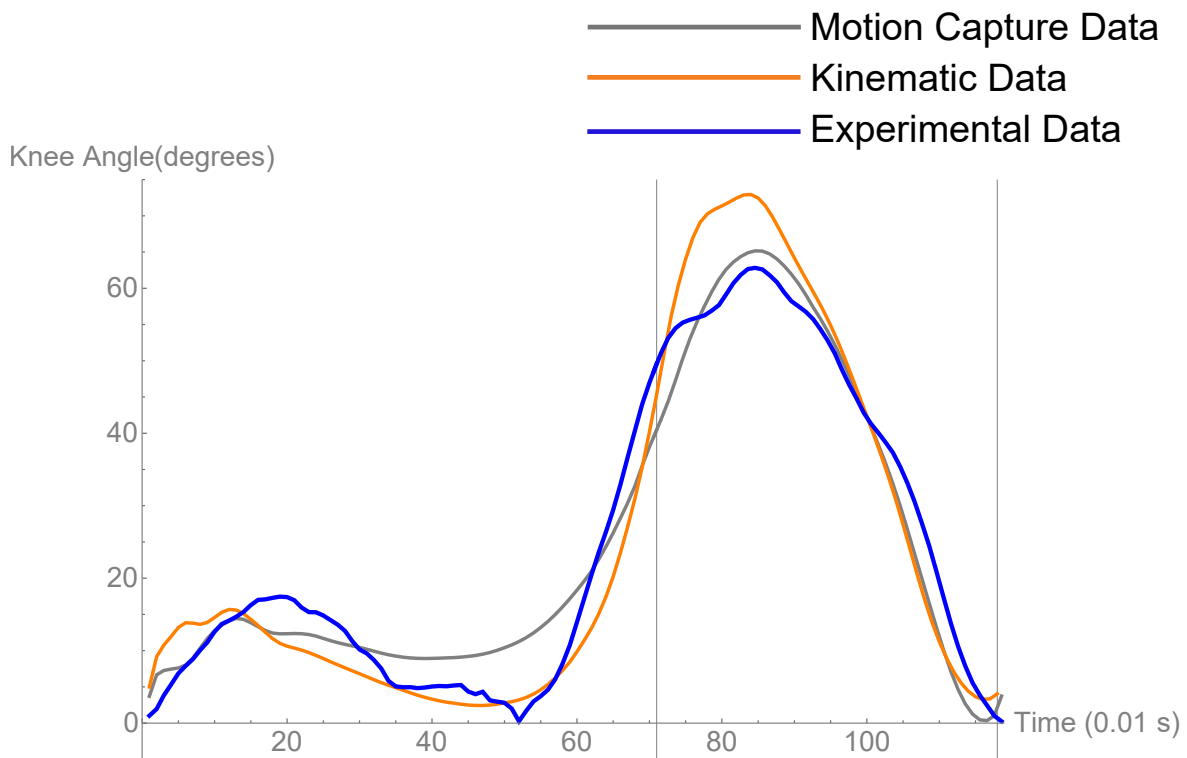


Figure 4.18: Knee angle of a healthy subject walking with and without the KAFO device compared to design predictions.

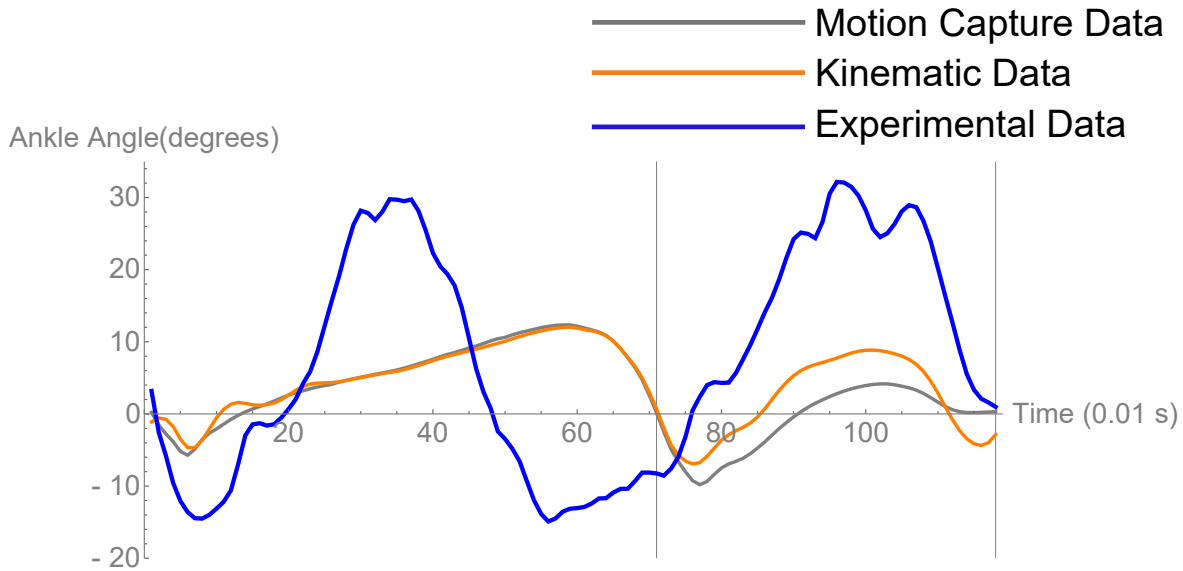


Figure 4.19: Ankle angle of a healthy subject walking with and without the KAFO device compared to design predictions.

As the knee-ankle-foot orthosis proposed in this work is a single DOF device, it was expected that driving the knee and ankle joints according to the motion data collected for the individual using motion capture, would result in near natural walking performance. However, the experimental data obtained from the preliminary test with the manufactured prototype shows that both joint and end-effector guidance play an important role for the design of a lower-leg orthosis that provides naturalistic walking gait. Thus, the following modifications are suggested to improve the performance: (a) The deviations of coupler curve of the KAFO linkage from target walking trajectory need to be reduced. The deviations at the ankle joint can be seen as compensatory actions in order for the foot to be guided by the linkage through the gait cycle, even when the knee joint motion stays close to natural. (b) The linkage selected for the KAFO design should have relatively smooth mechanical advantage profile. Sharp increases in the mechanical advantage abrupt changes on the metatarsal trajectory. (c) As the pivots  $B$  and  $F$  of the KAFO device are co-located with the knee and ankle joints of the human subject, it is essential that there is no slippage at the connections of the KAFO with the leg during operation, as it will introduce large forces on the human. Finally, out of plane motions of the linkage need to be completely eliminated by my designing the device

to tight tolerances.

## 4.5 Summary

A new procedure to design a six-bar linkage driven knee-ankle-foot orthosis is presented to produce natural walking motion. A Stephenson II six-bar function generator is designed to specify the angular movement of the knee and the ankle in the sagittal plane, based on the trajectory of the third metatarsal bone of the foot for the entire gait cycle. The six-bar linkage is designed by taking into account the dimensions of the calf and foot segments of the lower-leg of an individual, such that its ground link of the linkage is sized to individual's calf, and can be attached to it. Thus, the design methodology results in an individualized lower-leg orthosis based on the individuals anatomical movements and measurements. Details for adapting the linkage to design of an orthotic device are presented.

A pilot study is conducted to verify the design goals and to evaluate the kinematic parameters of the lower-leg as a person walks with the aid of the new custom KAFO device developed. The device is able to replicate knee joint motion very closely. However, at the ankle joint, excessive plantarflexion by  $20^\circ$ , and excessive dorsiflexion by  $7^\circ$  are observed. Stride length of walking with the KAFO prototype is found to be 97% of the subject's natural walking stride length. We hypothesize that the deviations in the gait kinematics observed with the manufactured prototype compared to design predications can be minimized by reducing deviations of linkage generated trajectory from the target metatarsal trajectory, ensuring continuity of motion on the end-effector trajectory and by improving manufacturing practices.

# Chapter 5

## Performance Optimization of Knee-Ankle-Foot Orthoses

### 5.1 Introduction

In this chapter, a new approach combining algebraic linkage synthesis with optimization to design an individualized six-bar linkage is presented. This design aims to optimize the end-effector trajectory of an exoskeleton type wearable lower-leg linkage device such that it closely matches the trajectory of the third metatarsal bone of the foot in addition to coordinating the joint angles at the knee and the foot over the entire gait cycle.

In the previous chapter, the synthesis of a Stephenson II six-bar function generator based exoskeleton type device to coordinate the motion of the knee and the ankle joints of the lower-leg is presented. The desired joint angles at the knee and the ankle are obtained by solving the inverse kinematics equations for a simplified lower-leg kinematic model at eleven points on the metatarsal trajectory obtained from an individual's motion data. The algebraic synthesis equations were solved in about two hours on a node of UC Irvine's high performance

computing cluster, and 332 design candidates were identified. Analysis of design candidates show that 233 solutions pass through eight of the eleven specified precision points, ninety pass through nine of the precision points, nine pass through ten precision points, and none pass through all the eleven precision points specified. As the goal of the exoskeleton type device was to guide the knee and ankle joints throughout the gait cycle, design candidates that pass through the most precision points were considered more desirable.

Pilot testing of the prototype of the KAFO device show angular deviations of up to  $20^\circ$  at the ankle joint (Figure. 4.19). Kinematic analysis of the linkage-based device had predicted close match for angles observed at the knee and ankle joints, while deviations were predicted in the metatarsal trajectory obtained. The test data from the prototype device show that equal consideration must be given to the trajectory of the metatarsal and the angular motion at the knee and ankle joints to obtain natural walking gait with the lower-leg orthosis. Thus, all six design candidates that were found to be free of order defects in previous chapter (Figure. 4.8). are considered for further study.

The goal of obtaining a close match between the generated and desired metatarsal trajectories is mathematically formulated as an optimization problem. The analytical solution for function generation synthesis of the Stephenson II six-bar linkage can be solved for eleven precision points, however the algebraic synthesis techniques do not guarantee control over the path generated between the consecutive precision points specified. The proposed linkage candidates can be studied at a much larger number of points on the metatarsal trajectory through the formulation of an optimization problem in order to modify their dimensions in order to optimize their performance. The previous synthesis and analysis process considers a linkage solutions passes through a defined precision position if it passes within  $10^{-2}mm$  of it. The performance optimization step considers all linkages that generate the desired metatarsal trajectory approximately, such that the generated trajectory may not exactly fall on all the precision points.

## 5.2 Forward Kinematics of Stephenson III Six-bar Linkage

The Stephenson II function generator is attached to the 2R serial chain that models the lower-leg kinematics and gives a Stephenson III six-bar linkage, whose coupler point traces the metatarsal trajectory. In order to optimize the performance of this linkage, we need to study the coupler trajectory so generated. The coupler point  $P_j$  of a Stephenson III six-bar linkage in the  $j^{th}$  position is shown in Figure 5.1.

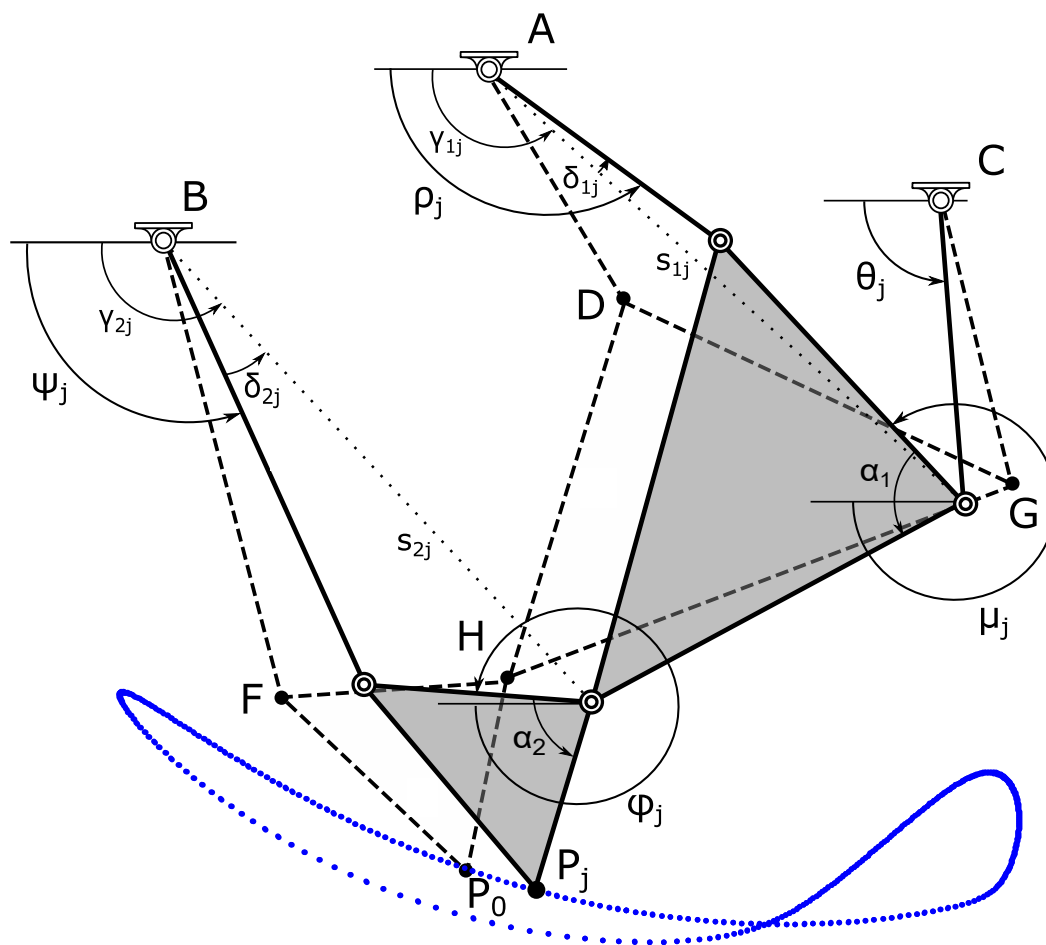


Figure 5.1: Geometry of the Stephenson III six bar linkage.

The forward kinematic equations for the point  $P_j$  of the coupler are formulated using complex numbers to represent the pivot positions in the reference position, and at the  $j^{th}$  position.  $\theta$

is the angular rotation of the input link, and the angle  $\theta_j$  defines the current position of the linkage. During a single gait cycle, the crank  $CG$  completes one full rotation around ground pivot  $C$  such that  $\theta_n = \theta_1$ . The point  $G$  on the crank in the  $j$ th position is given by the expression:

$$G_j = C + |G - C| e^{i\theta_j} \quad (5.1)$$

Let the variable  $s_{1j}$  indicate the distance between the points  $A$  and  $G_j$  in the  $j$ th position. Its value is given by:

$$s_{1j} = |G_j - A| \quad (5.2)$$

$s_{1j}$  creates the angle  $\gamma_{1j}$  with respect to the positive x-axis, hence  $\gamma_{1j}$  is given by:

$$\gamma_{1j} = \text{Arg}(G_j - A) \quad (5.3)$$

Let angle  $\delta_{1j} = \angle G_j A D_j$ . We can calculate its value by using the cosine rule for the triangle  $A D_j G_j$ :

$$\delta_{1j} = \arccos \left( \frac{|D - A|^2 + s_{1j}^2 - |G - D|^2}{2s_{1j} |D - A|} \right) \quad (5.4)$$

Then the angle  $\rho_j$  which determines if the link  $A D_j$  will be in the elbow up or elbow down position is defined as:

$$\rho_j = \gamma_{1j} - z_1 \delta_{1j} \quad (5.5)$$

Where

$z_1 = 1$  when point  $D_j$  is above the segment  $s_1$  : elbow up

$z_1 = -1$  when point  $D_j$  is below the segment  $s_1$ : elbow down

The position of the pivot  $D$  in the  $j^{th}$  position can thus be written as:

$$D_j = A + |D - A| e^{i\rho_j} \quad (5.6)$$

Angle  $\mu_j$  is defined as the angle between the positive x-axis and the side  $GD$  of the ternary link  $DGH$  in the  $j^{th}$  position:

$$\mu_j = \text{Arg}(G_j - D_j) \quad (5.7)$$

Angle  $\alpha_1$  is defined to be the constant angle between sides  $GD$  and  $GH$  of the ternary link  $DGH$ , measured counterclockwise:

$$e^{i\alpha_1} = \sqrt{\frac{(H - G)(\bar{D} - \bar{G})}{(\bar{H} - \bar{G})(D - G)}} \quad (5.8)$$

The location of the pivot  $H$  of the ternary link in the  $j^{th}$  position is then given by:

$$H_j = G_j + |H - G| e^{i(\mu_j + \alpha_1)} \quad (5.9)$$

Let the variable  $s_{2j}$  indicate the distance between the points  $B$  and  $H$  in the  $j^{th}$  position. Its value is given by:

$$s_{2j} = |H_j - B| \quad (5.10)$$

$s_{2j}$  creates the angle  $\gamma_{2j}$  with respect to the positive x-axis, hence  $\gamma_{2j}$  is given by:

$$\gamma_{2j} = \text{Arg}(H_j - B) \quad (5.11)$$

Angle  $\delta_{1j} = \angle G_j A D_j$  can be calculated by using the cosine rule for the triangle  $B F_j H_j$ :

$$\delta_{2j} = \arccos \left( \frac{|F - B|^2 + s_{2j}^2 - |H - F|^2}{2s_{2j} |F - B|} \right) \quad (5.12)$$

Then the angle  $\psi_j$  which determines if the link  $B F_j$  will be in the elbow up or elbow down position with respect to  $s_{2j}$  is given as:

$$\psi_j = \gamma_{2j} - z_2 \delta_{2j} \quad (5.13)$$

Where

$z_2 = 1$  when point  $H_j$  is above the segment  $s_2$  : elbow up

$z_2 = -1$  when point  $H_j$  is below the segment  $s_2$  : elbow down

The pivot  $F_j$  can then be written as:

$$F_j = B + |F - B| e^{i\psi_j} \quad (5.14)$$

Angle  $\phi_j$  is defined as the angle between the positive x-axis and the side  $H F$  of the coupler link  $F H P$  in the  $j^{th}$  position:

$$\phi_j = \text{Arg}(H_j - F_j) \quad (5.15)$$

Angle  $\alpha_2$  is the constant angle between sides  $H F$  and  $H P_0$  of the coupler link  $F H P$  in the reference position, measured counterclockwise:

$$e^{i\alpha_2} = \sqrt{\frac{(P_0 - H)(\bar{F} - \bar{H})}{(\bar{P}_0 - \bar{H})(F - H)}} \quad (5.16)$$

Thus, the expression for the coupler point  $P_j$  is given by:

$$P_j = H_j + |P_0 - H| e^{i(\phi_j + \alpha_2)} \quad (5.17)$$

## 5.3 Formulation of Objective Function for Performance Optimization

The objective function of the optimization problem consists of the error function that ensures that the original function generation equations continue to be satisfied as the dimensions of the linkage are systematically modified during the performance optimization process. Penalty functions are used to specify constraints on the metatarsal trajectory generated by the design candidates.

### 5.3.1 Angular Movement Error Function

Figure 5.2 shows the relative orientations of the moving links of the lower-leg linkage at the  $j^{th}$  point. The angular rotations are given by  $Q_j = e^{i\Delta\phi_j} = e^{i(\phi_j - \phi_0)}$ ,  $R_j = e^{i\Delta\rho_j} = e^{i(\rho_j - \rho_0)}$ ,  $S_j = e^{i\Delta\psi_j} = e^{i(\psi_j - \psi_0)}$ ,  $T_j = e^{i\Delta\theta_j} = e^{i(\theta_j - \theta_0)}$  and  $U_j = e^{i\Delta\mu_j} = e^{i(\mu_j - \mu_0)}$ , where  $j = 0, \dots, N - 1$ .

A point,  $P_j$  for  $j \in I\{0, N - 1\}$ , will lie on the coupler curve of the Stephenson III six-bar linkage if it satisfies its design equations, given as:

$$\begin{aligned}
 T_j(G - C) &= -U_j(H - G) - Q_j(P_0 - H) + (P_j - C) \\
 \bar{T}_j(\bar{G} - \bar{C}) &= -\bar{U}_j(\bar{H} - \bar{G}) - \bar{Q}_j(\bar{P}_0 - \bar{H}) + (\bar{P}_j - \bar{C}) \\
 R_j(D - A) &= -U_j(H - D) - Q_j(P_0 - H) + (P_j - A) \\
 \bar{R}_j(\bar{D} - \bar{A}) &= -\bar{U}_j(\bar{H} - \bar{D}) - \bar{Q}_j(\bar{P}_0 - \bar{H}) + (\bar{P}_j - \bar{A})
 \end{aligned} \tag{5.18}$$

The rotation operators  $T_j$  and  $R_j$  can be eliminated from Equations (5.18) by multiplying

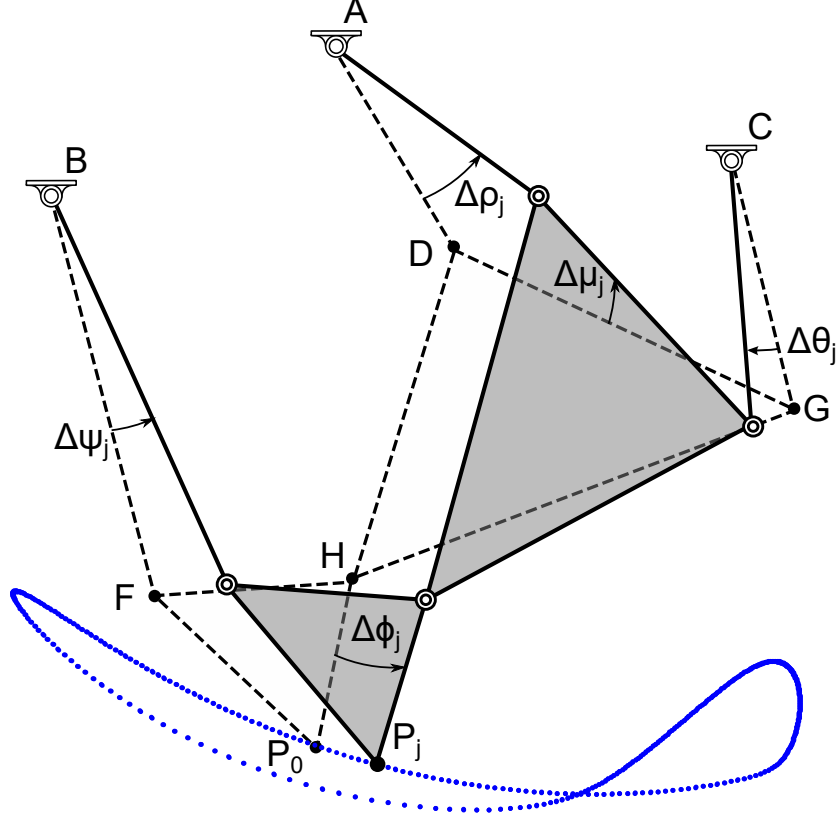


Figure 5.2: Relative orientations of moving links of the Stephen III six-bar linkage in the  $j^{th}$  position (adapted from [71]).

each equation with its complex conjugate to obtain:

$$\begin{aligned}
 |G - C|^2 &= |U_j(H - G) + Q_j(P_0 - H) - (P_j - C)|^2 \\
 |D - A|^2 &= |U_j(H - D) + Q_j(P_0 - H) - (P_j - A)|^2 \\
 j &= 0, \dots, N - 1
 \end{aligned} \tag{5.19}$$

To compute the numerical values of  $Q_j$ ,  $j \in I\{1, N - 1\}$ , consider:

$$\begin{aligned}
 S_j(F - B) + Q_j(P_0 - F) &= P_j - B \\
 \bar{S}_j(\bar{F} - \bar{B}) + \bar{Q}_j(\bar{P}_0 - \bar{F}) &= \bar{P}_j - \bar{B} \\
 S_j \bar{S}_j &= 1
 \end{aligned}$$

$$Q_j \bar{Q}_j = 1 \quad (5.20)$$

This set of equations (5.20) can be simplified by eliminating  $S_j$  and  $\bar{S}_j$  by using the relationship  $S_j \bar{S}_j = 1$  as:

$$\begin{aligned} & (\bar{P}_j - \bar{B})(P_0 - F)Q_j + \\ & \quad (F - B)(\bar{F} - \bar{B}) - (P_j - B)(\bar{P}_j - \bar{B}) - (P_0 - F)(\bar{P}_0 - \bar{F}) \\ & \quad + (P_j - B)(\bar{P}_0 - \bar{F})\bar{Q}_j = 0 \end{aligned} \quad (5.21)$$

$$j = 0, \dots, N - 1$$

Using the relationship  $Q_j \bar{Q}_j = 1$ , this equation can be written in a quadratic form with  $Q_j$  as the variable:

$$\begin{aligned} aQ_j^2 + bQ_j + c &= 0 \end{aligned} \quad (5.22)$$

$$j = 0, \dots, N - 1$$

where

$$\begin{aligned} a &= (\bar{P}_j - \bar{B})(P_0 - F) \\ b &= (F - B)(\bar{F} - \bar{B}) - (P_j - B)(\bar{P}_j - \bar{B}) - (P_0 - F)(\bar{P}_0 - \bar{F}) \\ c &= (P_j - B)(\bar{P}_0 - \bar{F}) \end{aligned}$$

The value of  $Q_j$  at point  $P_j$  is dependent only on the values of designer specified constant complex numbers  $B, F$  and  $P_0$ .

With the numerical values of  $Q_j$  corresponding to each value of  $P_j$ , we can solve for the numerical values of the rotation operator  $U_j$  and its conjugate  $\bar{U}_j$  using equations (5.19).

The following substitutions are introduced to simplify the equations:

$$\begin{aligned}
a &= a_x + ia_y = H - G \\
b_j &= b_{xj} + ib_{yj} = Q_j(P_0 - H) - P_j + C \\
c &= c_x + ic_y = H - D \\
d_j &= d_{xj} + id_{yj} = Q_j(P_0 - H) - P_j + A \\
f &= f_x + iF_y = G - C \\
g &= g_x + ig_y = D - A \\
j &= 0, \dots, N - 1
\end{aligned} \tag{5.23}$$

Substituting into equations (5.19), we obtain:

$$\begin{aligned}
\begin{bmatrix} a\bar{b}_j & \bar{a}b_j \\ c\bar{d}_j & \bar{c}d_j \end{bmatrix} \begin{bmatrix} U_j \\ \bar{U}_j \end{bmatrix} &= \begin{bmatrix} f\bar{f} - a\bar{a} - b_j\bar{b}_j \\ g\bar{g} - c\bar{c} - d_j\bar{d}_j \end{bmatrix} \\
j &= 0, \dots, N - 1
\end{aligned} \tag{5.24}$$

Which is a system of linear equations and can be solved by using Cramer's rule. If the calculated values of  $U_j$  and  $\bar{U}_j$  satisfy the relationship  $U_j\bar{U}_j = 1$ , i.e. they are conjugates of each other, the point  $P_j$  satisfies the algebraic synthesis equations of the linkage defined by the pivots  $(A, B, C, D, F, G, H, P_0)$ .

The error between the present design candidate and desired linkage is formulated as the sum of squares of the difference between their generated and desired trajectories, and is generally referred to as the Structural Error Function [80]. Here we define an alternative expression to evaluate the error between the present and desired linkages of a Stephenson III linkage, without resorting to comparison of points on the generated and desired trajectories. This Error Function for a set of  $N$  points on the desired curve for which the linkage is to be

optimized is given as:

$$Err(\mathbf{X}) = \sum_{k=1}^N U_k(\mathbf{X}) \bar{U}_k(\mathbf{X}) - 1$$

Where,  $\mathbf{X}$  is the vector consisting of the optimization variables.

### 5.3.2 Metatarsal Trajectory Constraints

Constraints on the metatarsal trajectory are formulated as penalty functions. The generated trajectory must have certain characteristics in order to be adapted to the design of a KAFO. In general, it is known that while the addition of certain constraints are essential to ensure that the linkage is functional, it increases solution complexity, and can introduce discontinuities in the solution space [85]. Hence, the smallest set of constraints are specified. Constraints that were determined to be critical for function of the obtained linkage based on the assessment of the algebraically obtained solutions are: closure of the end-effector trajectory as the crank completes one rotation, continuity between trajectory points, and minimum position and orientation mismatch between the generated and target metatarsal trajectory.

We utilize penalty methods to handle cases when the optimization variables become out-of-bounds. By setting appropriate weights for each penalty term we can create an objective function-based criterion that will drive the solutions away from undesirable areas. We utilize a policy of adaptive penalty [84], in which whenever the optimization variables violate a constraint, the objective function value is increased by a penalty that depends not only on the number and type of violation, but also their magnitude.

## Closure of Metatarsal Trajectory

For a KAFO mechanism, it is essential that the linkage coupler point completely traces the closed metatarsal trajectory as the device moves through one gait cycle, such that  $P_0 = P_{N-1}$  (see Figure. 5.3). For practical reasons, we choose to have a fully rotatable crank. Thus the existence of a real valued coupler point must be verified at each time step as the crank rotates through  $360^\circ$ , in  $N$  steps. If the coupler point cannot be computed using the forward kinematics equations presented, a penalty  $W_c$  is imposed for each violation of this condition. Additionally, the euclidean distance between the coupler point when crank angle  $\theta_0 = 0^\circ$  and  $\theta_{N-1} = 360^\circ$  is calculated. A non-zero value of  $|P_0 - P_{N-1}|$  indicates a open trajectory and imposes an additional penalty of  $W_c \times |P_0 - P_{N-1}|$  on the objective function value. The closure condition is evaluated as:

$$M_c = |P_0(\mathbf{X}) - P_{N-1}(\mathbf{X})| + \sum_{i=0}^{N-1} g_c(P_i(\mathbf{X})) \quad (5.25)$$

where

$$g_c(x + iy) = \begin{cases} 0 & \text{if } x \text{ and } y \text{ are real} \\ 1 & \text{if } x \text{ and } y \text{ are not real} \end{cases}$$

## Continuity between Trajectory Points

When the determinant of the Jacobian matrix of a general kinematic chain equals zero, different branches of the inverse kinematic problem meet [98] (see Figure. 5.4 and 5.5). Thus, in order to ensure that all the points on the generated metatarsal trajectory of the linkage optimized for both end-effector and joint guidance performance belong to the same branch of the linkage. Any instance of existence of values of the Jacobian determinant close

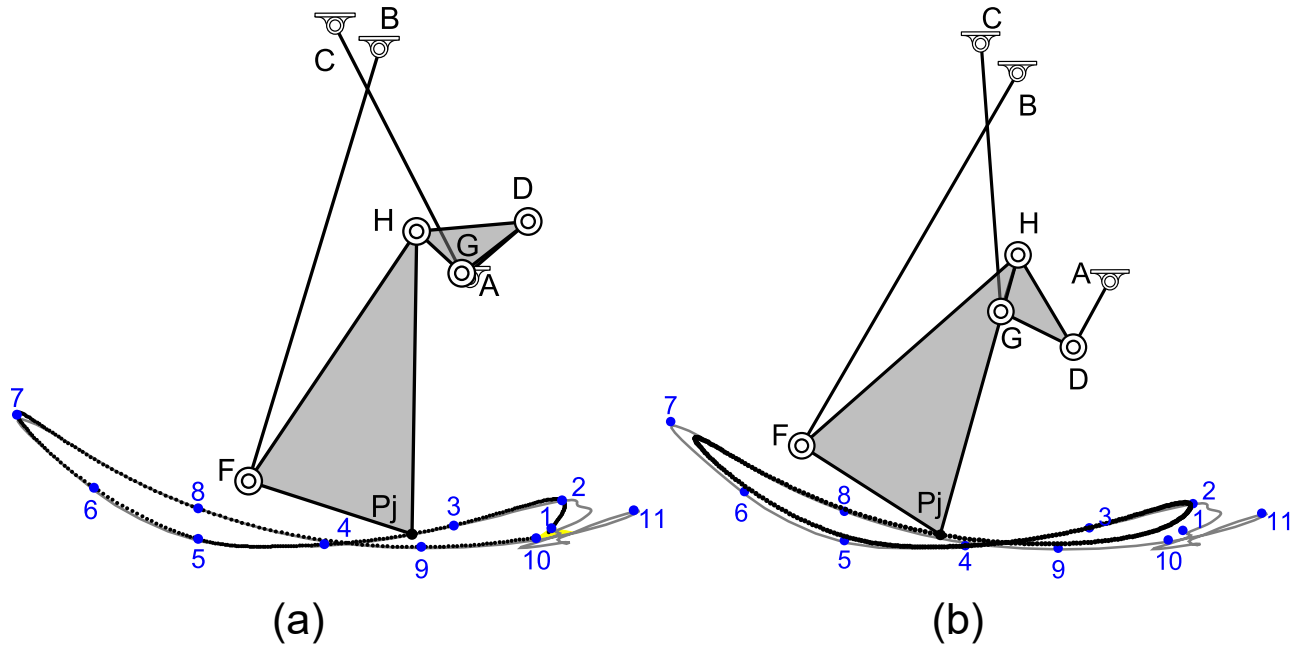


Figure 5.3: A linkage (a) without and (b) with a closed and continuous metatarsal trajectory between precision points numbered 1 and 10.

to zero ( $\pm 10^{-4}$ ) are penalized by a factor of  $W_j$  according to the following function:

$$M_b = g_j \left( \det(J_j(\mathbf{X})) \right) \quad (5.26)$$

where

$$g_j(x) = \begin{cases} 0 & \text{if } x \leq 10^{-4} \\ 1 & \text{if } x > 10^{-4} \end{cases}$$

### Minimum Position and Orientation Mismatch

When searching for a linkage that meets the shape specifications of the end-effector trajectory, it is easier to find solutions for which the final shape of the solution trajectory is similar to the desired shape, but they differ in size, location, and orientation. By translating, rotating and scaling the solution mechanism appropriately, without changing relative

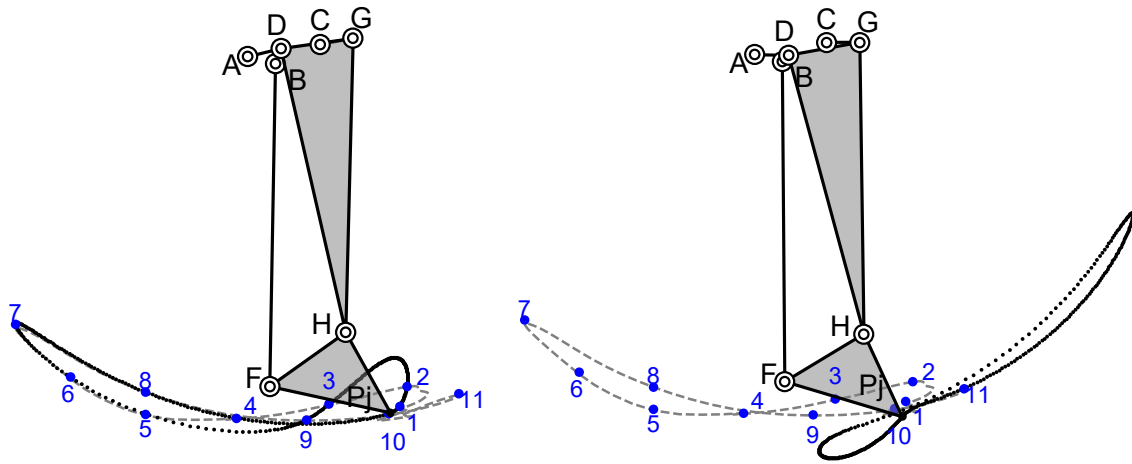


Figure 5.4: Two branches of a given linkage.

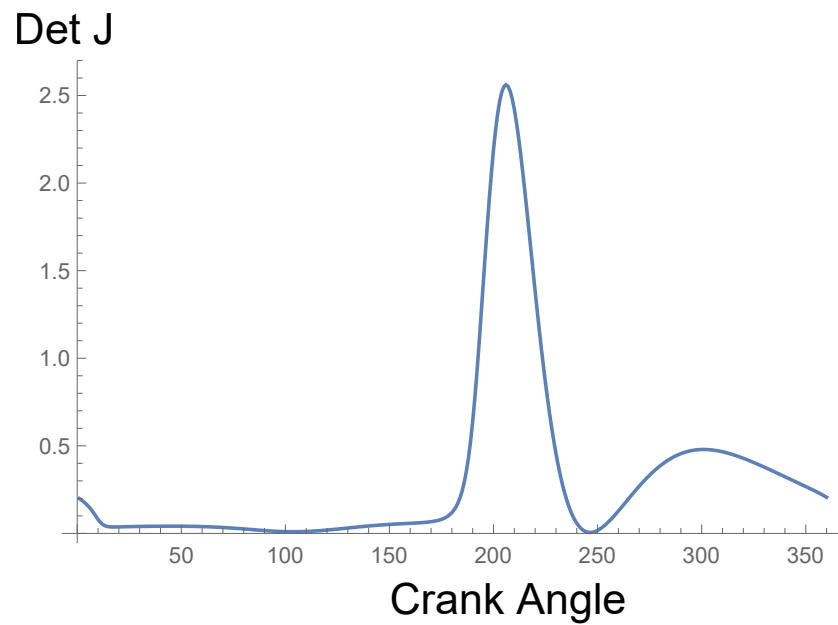


Figure 5.5: The Jacobian determinant values for a given linkage during one gait cycle.

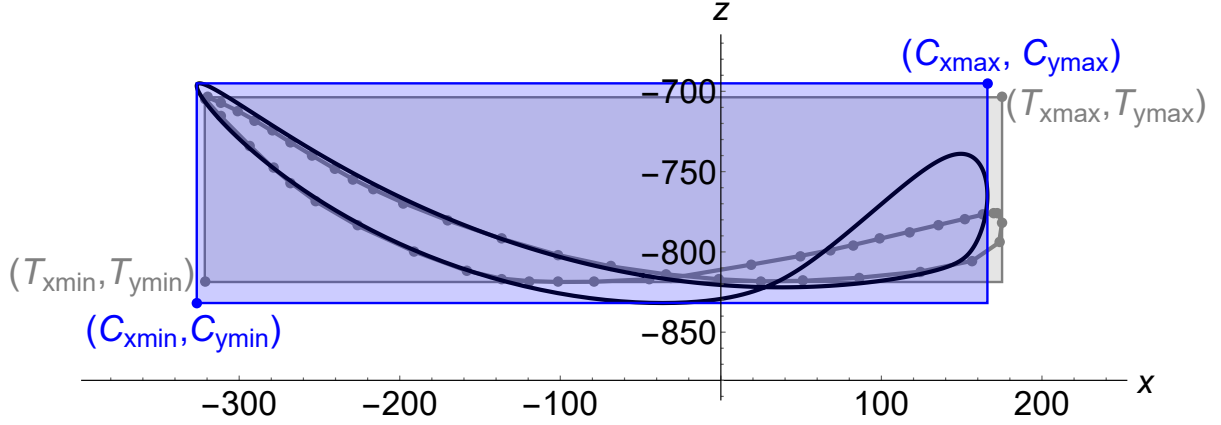


Figure 5.6: Bounding boxes of the coupler curve (blue) and the target trajectory (gray).

dimensions of various links, the end-effector trajectory can be made to coincide with the desired metatarsal trajectory in shape, position, orientation and size [75]. However, as the KAFO linkage incorporates the lower-leg kinematics via specifications of the 2R chain based on an individual's motion data, transformations of the linkage are not permitted.

Thus, it is necessary to minimize the deviations in the location and orientation between the generated metatarsal trajectory and desired metatarsal trajectory specified from motion data of the individual. For a particular optimization variable vector, bounding boxes are specified around the generated trajectory, such that the corners of the box are denoted by  $(C_{x_{min}}, C_{y_{min}})$  and  $(C_{x_{max}}, C_{y_{max}})$ . Similarly the corners of the target curve bounding box are given by  $(T_{x_{min}}, T_{y_{min}})$  and  $(T_{x_{max}}, T_{y_{max}})$ . Then, from Figure 5.6, we can see:

$$M_{tc} = \left( (T_{x_{max}} - C_{x_{max}}(\mathbf{X}))^2 + (T_{y_{max}} - C_{y_{max}}(\mathbf{X}))^2 + (T_{x_{min}} - C_{x_{min}}(\mathbf{X}))^2 + (T_{y_{min}} - C_{y_{min}}(\mathbf{X}))^2 \right)^{1/2} \quad (5.27)$$

## Objective Function

The design requirements and criteria discussed above are simultaneously evaluated in the design of the a six-bar lower-leg linkage by formulating the an optimization problem with the following general structure:

$$\underset{(\mathbf{X})}{\text{minimize}} \quad \mathbf{f}(\mathbf{X}) \quad (5.28)$$

$$\text{subject to} \quad \mathbf{G}(\mathbf{X}) \quad (5.29)$$

where,  $\mathbf{f}$  is a vector error function;  $\mathbf{X}$  is the vector of optimization variables; and  $\mathbf{G}$  is a vector function of the constraints on the end-effector trajectory. In particular, for the criteria discussed above, the optimization problem is written as:

$$\underset{(\mathbf{X})}{\text{minimize}} \quad \sum_{k=0}^{N-1} U_k(\mathbf{X}) \bar{U}_k(\mathbf{X}) - 1 \quad (5.30)$$

$$\begin{aligned} \text{subject to} \quad & | P_0(\mathbf{X}) - P_{N-1}(\mathbf{X}) | = 0 \\ & \det (J_j(\mathbf{X})) \leq 10^{-4} \\ & T_{x_{max}} - C_{x_{max}}(\mathbf{X}) = 0 \\ & T_{y_{max}} - C_{y_{max}}(\mathbf{X}) = 0 \\ & T_{x_{min}} - C_{x_{min}}(\mathbf{X}) = 0 \\ & T_{y_{min}} - C_{y_{min}}(\mathbf{X}) = 0 \end{aligned} \quad (5.31)$$

It can be written as a weighted objective function using penalties as:

$$\min_{(\mathbf{r})} \left\{ \left[ \sum_{k=0}^{N-1} U_k(\mathbf{X}) \bar{U}_k(\mathbf{X}) - 1 \right] + W_c \times M_c + W_j \times M_j + W_{tc} \times M_{tc} \right\} \quad (5.32)$$

## 5.4 Performance Optimization of Lower-leg Linkage

### 5.4.1 Selection of Target Curve

The performance optimization problem 5.32 is solved as outlined in Figure. 5.7.

The first step consists of defining the desired metatarsal trajectory using the motion capture data obtained for the individual. The motion data used for the performance optimization of the six-bar KAFO linkage spans seven gait cycles. Each cycle of walking data consists of 116 data points. The algebraic synthesis process utilized a set of eleven points the gait trajectory that is averaged over these seven cycles.

Based on the algebraic synthesis process, we find that none of the design candidates were able to pass through precision point number 11. Analysis of the motion data shows that the removal of region of the trajectory defined via precision point 11 does not affect the result of the of the performance optimization process, hence it is removed from the set of points defining the target trajectory.

During performance optimization, the objective function can be evaluated on a much larger set of points on the metatarsal trajectory of the individual as compared to the algebraic synthesis process. We select a set of points on the target trajectory such that the basis spline curve passing through these points is close to the original curve. This is done by creating a basis spline defined with the control points as the 116 data points on the metatarsal trajectory. Fifty points spread uniformly over the basis spline of the target curve are selected. These points are shown in Figure 5.8, and form the target trajectory for the numerical performance optimization procedure.

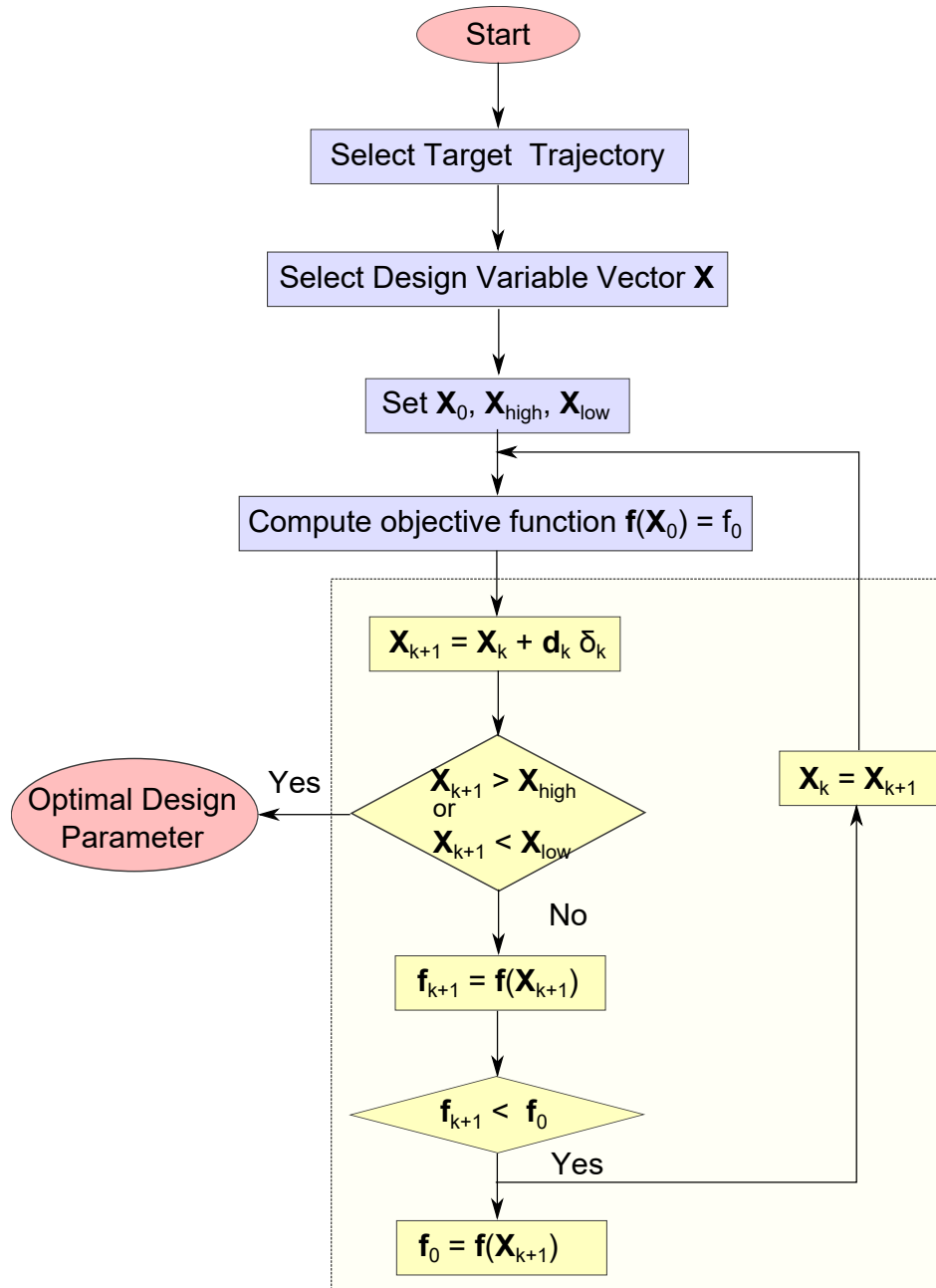


Figure 5.7: The numerical procedure for performance optimization of the lower-leg KAFO mechanism.

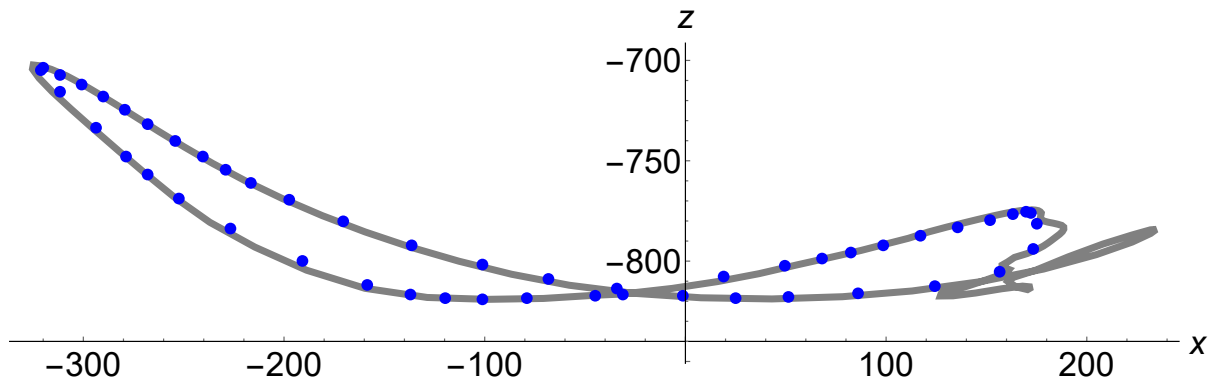


Figure 5.8: Set of 50 points obtained from basis spline of the motion data.

### 5.4.2 Selection of Design Variable Vector

It is necessary to distinguish optimization variables from design variables. The design variables are required to fully define a linkage, while the optimization variables are the input parameters for the performance optimization problem define above. The designer specified linkage parameters and variable parameters are shown in Table. 5.1. It should be noted that the crank angle  $\theta_j$  of the six-bar linkage which is the input for forward kinematics formulation for the linkage is not a variable parameter with regards to the performance optimization of the linkage. A six-bar linkage has seven pivots which determine its kinematic characteristics. Fixed pivots  $B$  and  $F$  are placed co-axially with the knee and ankle joints, respectively and are specified by the designer using motion data of the subject, hence are constants.

Input Data	Variable Parameters
Pivot B ( $B_x + iB_y$ )	Pivot A ( $A_x + iA_y$ )
Pivot F ( $F_x + iF_y$ )	Pivot C ( $C_x + iC_y$ )
Pivot $P_0$ ( $P_{0x} + iP_{0y}$ )	Pivot D ( $D_x + iD_y$ )
	Pivot G ( $G_x + iG_y$ )
	Pivot H ( $H_x + iH_y$ )

Table 5.1: Input data and variables for the synthesis and optimization process

The performance optimization problem can have at most ten optimization variables (the five pivot positions and their conjugates), not all of which contribute to an improvement in the performance of the linkage as specified by the objective function. The number optimization

variables is independent of the number of precision points. Therefore, increasing the number of precision points does not change the dimension of the search space.

However, the complexity of the performance optimization problem increases with the number of optimization variables. A design parameter vector of size ten, consisting of

$$(\mathbf{X} = (A_x, A_y, C_x, C_y, D_x, D_y, G_x, G_y, H_x, H_y)^T)$$

gives a solution space of dimension  $2^{10} = 1024$ . Thus we select a design variable vector that consists of pivot locations that contribute most to significant changes in the objective function value. It is found that varying locations of pivots D, G and H do not cause any significant change in the value of the objective function. It is also important to choose the variables as pivots whose locations can be modified without disassembling the mechanism. This will allow the mechanism to be reconfigured to obtain optimal performance without rebuilding the entire mechanism.

Based on these criteria, we identify a small subset of structural variables of the KAFO linkage, which when modified in a known fashion produce a mechanism that tracks a desired end-effector trajectory. Hence, the optimization process continues with the locations of pivots  $A$  and  $C$  as the optimization variables. The design variable vector  $\mathbf{X}$  consists of:

$$\mathbf{X} = \begin{bmatrix} A_x \\ A_y \\ C_x \\ C_y \end{bmatrix} \tag{5.33}$$

### 5.4.3 Selection of Initial Designs

The solutions obtained from the algebraic synthesis process (shown in Figure. 5.9) are used to define the initial values of the design variable vector described in the previous subsection.

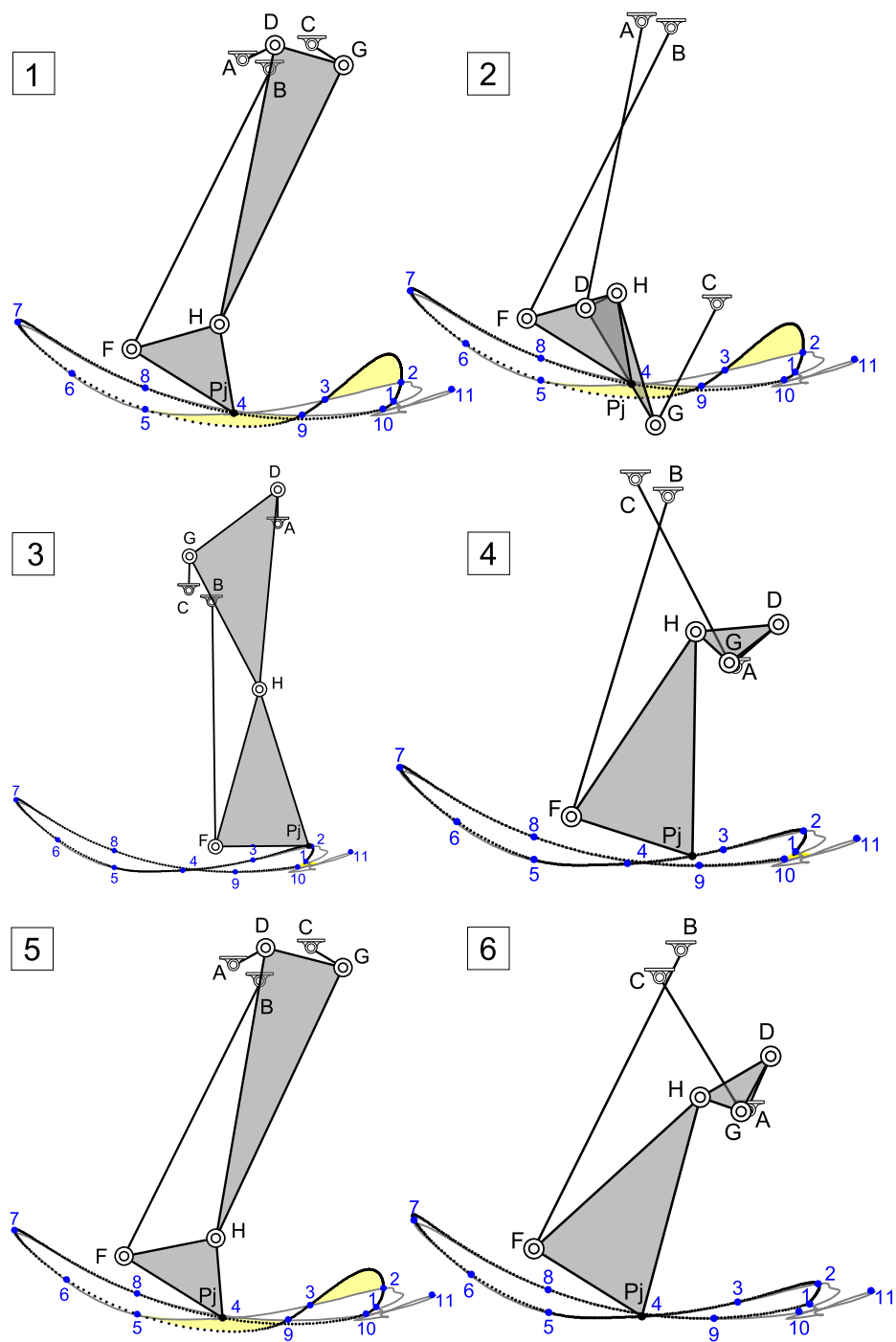


Figure 5.9: Initial designs for the performance optimization of six-bar KAFO.

#### 5.4.4 Solution of Performance Optimization Problem

Optimization algorithms can be classified based on their reliance on objective function derivatives [84]. The classical approach to optimization, which includes derivative-based methods, is not appropriate for this problem as the constrained objective function defined here corresponds to non-differentiable regions in the solution space.

Thus, we rely on derivative-free methods, also called direct search algorithms, which test the objective function at new points generated based on algorithm specific rules. Derivative-free optimization algorithms, namely, Nelder-Mead, Simulated Annealing, Differential Evolution and Random Search fail to converge to real solutions.

Analysis of the algebraic synthesis solutions show that there exist linkage solutions in the vicinity of the synthesis solutions that do not meet the strict algebraic synthesis criteria, but exhibit similar kinematic characteristics. Thus a direct search in the vicinity of the algebraic synthesis solutions is proposed. The objective functions is tested by generating a  $10 \times 10$  mm grid with a step size of 1 mm centered about the solution obtained from the algebraic synthesis process for the design parameter vector as shown in Figure 5.10. For each candidate linkage thus generated, the coupler-point trajectory is analytically determined and the values of three penalty terms are evaluated. It simulates the linkage trajectories by rotating the crank link from  $0^\circ$  to  $360^\circ$  in increments of  $1^\circ$ , solving for the corresponding positions of the other dependent pivots and links.

Figure. 5.7 schematically presents the grid search process as it visits all the generated grid points within the region given by  $\mathbf{X}_{high}$  and  $\mathbf{X}_{low}$  while storing the current best point in memory as  $\mathbf{f}_0$ . Even though generating a sequence of grid points is trivial, this method faces a step size problem. A very small step size results in the computation time increasing exponentially, as the grid with  $N = 20$  points in one dimension requires the evaluation of the objective function at  $20^4 = 160,000$  points for the 4 dimensional design variable vector.

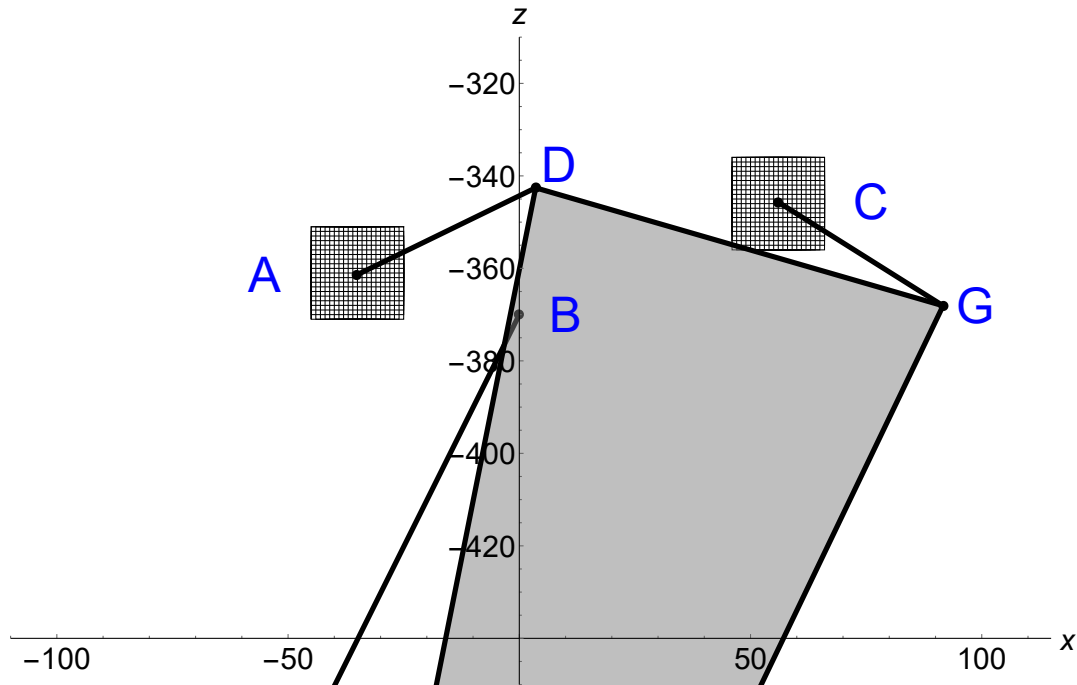


Figure 5.10: Visualization of the grid of positions where the objective function is to be evaluated.

## 5.5 Results

The grid search process successfully finds design candidates that have lower objective function values than the initial design for three of six initial designs specified (shown in Figure. 5.9). The optimal design parameters obtained for initial design candidates I, IV and V are presented in Tables. 5.2 - 5.4. Figures. 5.11 - 5.13 show the optimized linkages and their generated trajectories as compared to the initial designs.

Design Parameters	Initial Design (mm)	Optimal Solution (mm)
A	(- 35.05, -361.37)	(-38, -365)
B	(0, -370)	(0, -370)
C	(55.98, -345.67)	(57, -345)
D	(3.54, -342.59)	(3.54, -342.59)
F	(-180.558, - 732.524)	(-180.558, - 732.524)
G	(-91.63, -368.68)	(-91.63, -368.68)
H	(-67.99, -700.67)	(-67.99, -700.67)

Table 5.2: Design parameters of the optimal design solution I (all pivot locations are given in mm).

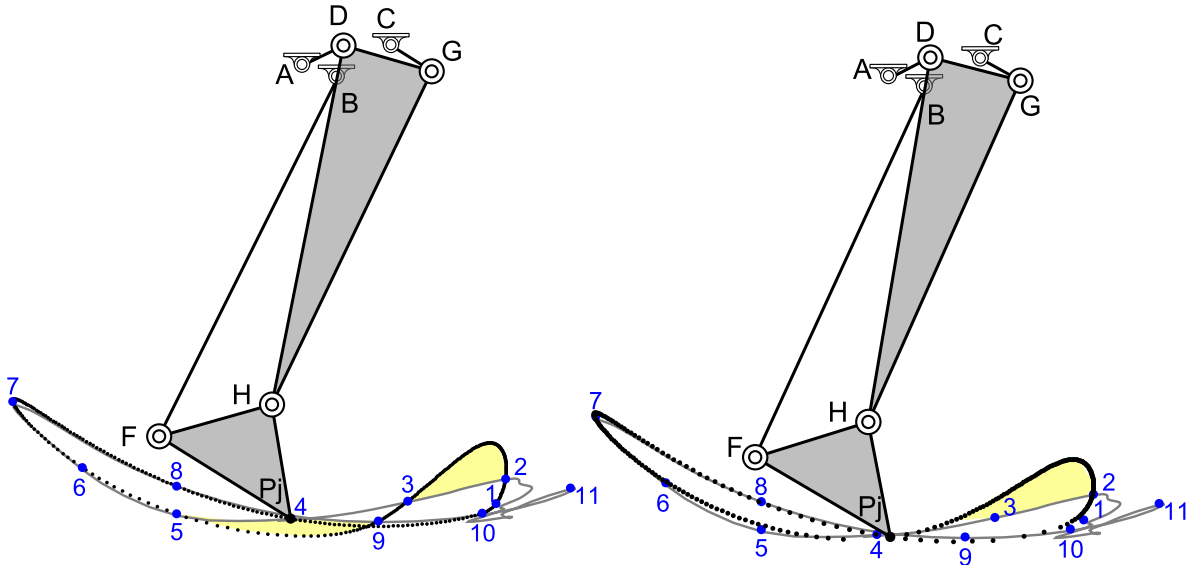


Figure 5.11: Comparison of Design Candidate 1 with the optimal linkage solution.

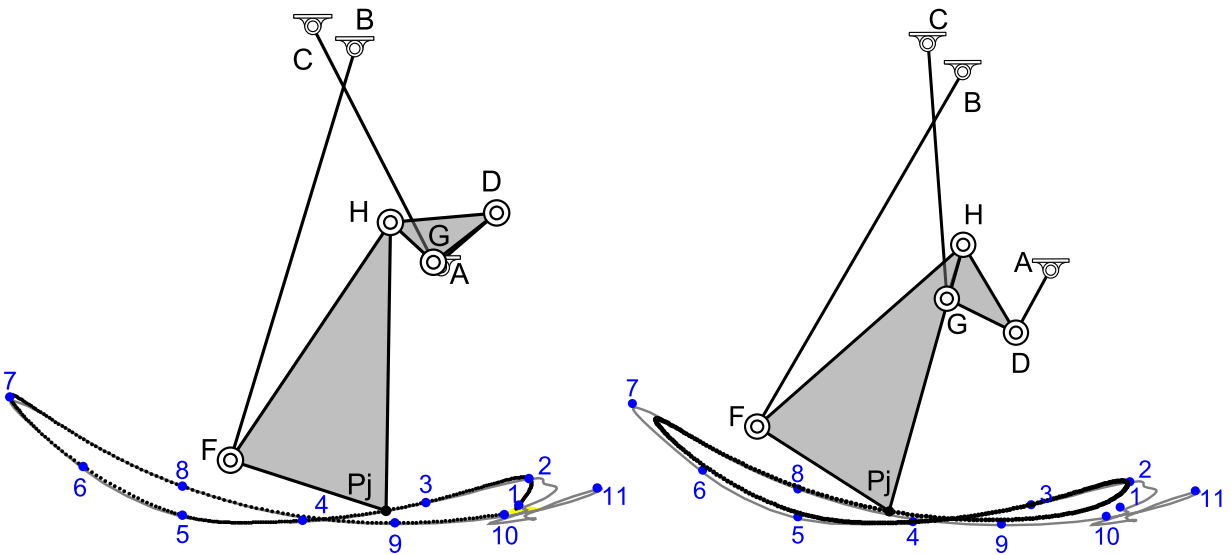


Figure 5.12: Comparison of Design Candidate 4 with the optimal linkage solution.

The new linkage selected for development of the lower-leg KAFO device is chosen based on having the closest fit to the target metatarsal trajectory as well as the desired angular motion profiles at the knee and ankle joints, its kinematic performance over the entire gait cycle. Anthropomorphism of the device is sacrificed to obtain for better functional performance. A solid model of the selected six-bar linkage design is shown in Figure. 5.14, and the manufactured prototype is shown in Figure. 5.15. Preliminary evaluation of the device show

Design Parameters	Initial Design (mm)	Optimal Solution (mm)
A	( <b>79.51</b> , <b>-57.85</b> )	( <b>81</b> , <b>-570</b> )
B	(0, -370)	(0, -370)
C	( <b>-38.95</b> , <b>-347.93</b> )	( <b>-34</b> , <b>-343</b> )
D	(111.709, - 505.472)	(111.709, - 505.472)
F	(-180.558, - 732.524)	(-180.558, - 732.524)
G	(73.3652, - 570.751)	(73.3652, - 570.751)
H	(21.4038, - 550.683)	(21.4038, - 550.683)

Table 5.3: Design parameters of the optimal design solution IV (all pivot locations are given in mm).

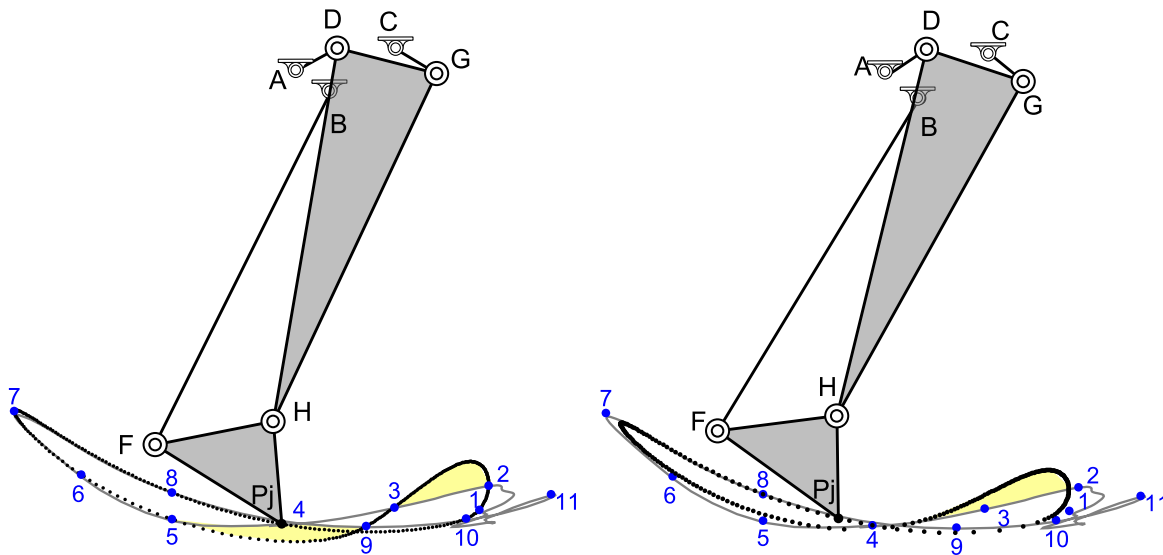


Figure 5.13: Comparison of Design Candidate 5 with the optimal linkage solution.

Design Parameters	Initial Design (mm)	Optimal Solution (mm)
A	( <b>- 33.11</b> , <b>-344.42</b> )	( <b>-34</b> , <b>-347</b> )
B	(0, -370)	(0, -370)
C	( <b>71.5</b> , <b>-323.96</b> )	( <b>72</b> , <b>323</b> )
D	(8.56, -321.57)	(8.56, -321.57)
F	(-180.558, - 732.524)	(-180.558, - 732.524)
G	(111.24,-347.77)	(111.24,-347.77)
H	(-57.84, -708.15)	(-57.84, -708.15)

Table 5.4: Design parameters of the optimal design solution V (all pivot locations are given in mm).

promising qualitative results, as the new device is easier to operate, lighter and considerably more comfortable than the previous prototype designed.

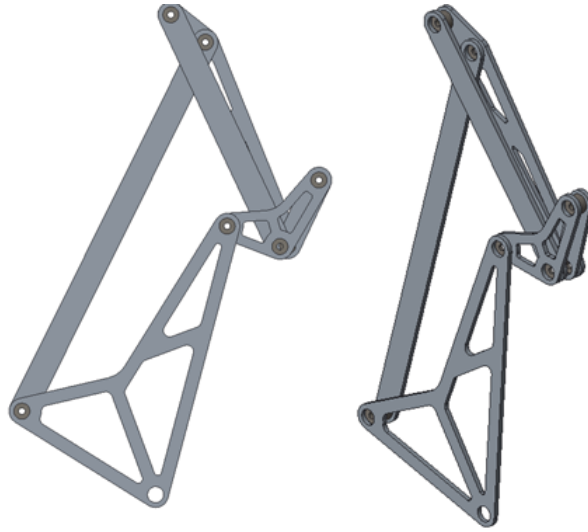


Figure 5.14: Solid model of the optimized design solution IV that is selected to be developed as a KAFO device.



Figure 5.15: Prototype of the new KAFO device.

## 5.6 Summary

A design procedure for optimally synthesizing a six-bar linkage to drive a Knee-Ankle-Foot-Orthosis with desired kinematic characteristics to accurately generate natural human walking motion is presented. The design problem is formulated as performance optimization problem

that minimizes the error between the generated and desired end-effector trajectories of the device, while maintaining the angular movement profiles specified at the joints it spans, and without violating practical physical requirements for the linkage to be successfully assembled. We find that both joint and end-effector trajectory guidance play important role in the design of single DOF knee-ankle-foot orthosis. Device testing and evaluation need to be performed to quantify the results.

The optimization problem is defined as the minimization of an objective function, formulated to capture the difference between the current guess solution and a linkage that would meet all the desired criteria. The solution space is found to be highly non-linear in structure, and requires further careful study. The complexity of the solution space is mitigated by selecting a small subset of the variable structural parameters to serve as optimization parameters. A grid search is carried out in the vicinity of the initial designs obtained from the algebraic synthesis process. Three viable linkage solutions are identified that produce the desired coordination of knee and ankle angular movements and trace the specified metatarsal trajectory accurately. The advantage of this formulation lies in the use of solutions from the algebraic synthesis process as initial designs for the optimization process.

# Chapter 6

## Conclusion

### 6.1 Summary

The contribution of this dissertation is a design process for customized wearable devices that provide joint guidance and support for individuals with disabilities in their hands or legs in order to increase mobility. The devices presented in this work are compact, passive and do not require complex locking mechanisms.

An extensive review of linkage mechanisms utilized in assistive devices is presented and an attempt is made to document the synthesis techniques. In general, existing wearable assistive devices are classified as either exoskeleton type or end-effector type based on whether they provide motion assistance for each joint of the limb or only at the distal segment. In the last five years, a number of designs for finger and thumb devices have been proposed that utilize linkage synthesis based on motion capture data of an individual. Most of these devices attempt to provide specific guidance at the joints.

Specifically, a design methodology is presented to synthesize a compact four-bar linkage

that moves smoothly between two task positions specified on a simplified planar section of the thumb tip trajectory during curling action. A 3D printed prototype of the resulting end-effector type device is built.

Then, the design, development and testing of a multi-axis hands-free crutch device is presented. It consists of a four-bar multi-axis knee designed using kinematic synthesis techniques with higher-order task constraints, and is incorporated into a hands-free crutch test bed to provide natural knee movement during walking. A review of literature on KAFO devices shows that there is a need to design KAFO knee joints that can reproduce normal knee function over the entire gait cycle, and are small in size, lightweight, and inexpensive. Four-bar knee designs have been proposed in the past due to their similarity with the knee joint, and their ability to mimic the knee joint motion more accurately as compared to a locked or a simple revolute joint knee. We design a four-bar multi-axis knee that takes into account the shape of the desired knee trajectory. We evaluate its functionality by incorporating it into a hands-free crutch device. We observed improvements with respect to hip-hiking and stride lengths compared to a locked knee device.

The design, development and testing of a Knee-Ankle-Foot-Orthosis that uses a single one DOF linkage to produce the natural human walking trajectory is also presented. The basic purpose of this research is to suggest a methodology which may be used to synthesize and correctly place a proper mechanical system, which is meant to guide externally the natural motion of an individual's lower leg. This linkage can trace the desired gait trajectory, while satisfying size constraints such that it can be adapted to the design of wearable and portable orthotic devices. These constraints are described by kinematically modeling the human body segment using a simple serial chain in the sagittal plane, which allows us to identify angular motion requirements for the knee and ankle joints based on an individual's motion capture data. A six-bar linkage is designed to coordinate the motion of both the knee and the ankle joints simultaneously. A full-scale prototype of the device is built, and we report the results

of pilot tests that show a healthy user walking with the device prototype has normal knee function, and shows good stride length compared to natural walking. Significant deviations are observed in the kinematics of the ankle joint compared to the design predictions.

Finally, a performance optimization procedure is presented to optimally modify the dimensions of six-bar linkage solutions obtained from the algebraic synthesis process. This work also illustrates the use of penalty functions for steering the optimization towards physically viable linkages that retain the specified characteristics of the knee and ankle joint movement, while minimizing the difference between the generated and desired metatarsal trajectories. The utility of algebraic synthesis solutions as initial guesses for obtaining solutions in a highly non-linear solution space is also demonstrated. The proposed linkage solutions for the design of the knee-ankle-foot orthotic device have six links with simple shapes that can be easily and quickly manufactured.

This work systematically explores different design requirements specified using individualized motion data in order to guide the movement of the thumb or the lower leg. It establishes the importance of specifying biological movements in terms of joint angular movements as well as end-effector trajectories to design linkage driven wearable devices.

## **6.2 Future Work**

The utility of specifying velocity and acceleration constraints for the design of linkages that reproduce biological motions can be explored for a larger number of task positions, as well as for more complex linkage topologies. Actuation of the designed devices needs to be explored.

Four and six-bar linkages explored in this work are limited by the number of their structural variables, which restricts the the movement features that can be specified by the designer. In order to capture the specific velocity and other higher motion derivative characteristics

of biological movements, it might be helpful to provide a larger number of task positions on the desired trajectory.

Finally, we observed that the solution space for the optimization problem formulated in this work is highly non-linear in structure. A large number of local minimas are found to be clustered around the solutions obtained from the algebraic synthesis process. It shows that a careful study of the properties of these regions will yield techniques, possibly in the form of design tables or charts, that can help the designer to selectively and accurately modify the structure of the linkage to generated trajectories that posses the desired characteristics. This will lead to the design of customized adjustable linkage driven orthoses that can produce a desired set of trajectories through simple modifications of its structure. The utility of these linkage-based orthoses can be increased if the output trajectory of the device can be adjusted in real-time to obtain particular characteristics.

# Bibliography

- [1] T. A. O. P. A. L. (AOPA), “About orthoses and prostheses.”
- [2] P. Agarwal, Y. Yun, J. Fox, K. Madden, and A. D. Deshpande, “Design, control, and testing of a thumb exoskeleton with series elastic actuation,” *The International Journal of Robotics Research*, vol. 36, no. 3, pp. 355–375, 2017.
- [3] A. R. LLP, “Global orthopedic braces & supports market analysis & trends - industry forecast to 2025,” 2017. Report ID: 3752482.
- [4] Markets and Markets, “Otc orthopedic braces - global forecast to 2021,” 2016.
- [5] TechNavio, “Global orthopedic bracing and support systems market 2017-2021,” May 2017.
- [6] P. Heo, G. M. Gu, S.-j. Lee, K. Rhee, and J. Kim, “Current hand exoskeleton technologies for rehabilitation and assistive engineering,” *International Journal of Precision Engineering and Manufacturing*, vol. 13, no. 5, pp. 807–824, 2012.
- [7] F. Tian, M. S. Hefzy, and M. Elahinia, “State of the art review of knee–ankle–foot orthoses,” *Annals of biomedical engineering*, vol. 43, no. 2, pp. 427–441, 2015.
- [8] C. N. Schabowsky, S. B. Godfrey, R. J. Holley, and P. S. Lum, “Development and pilot testing of hexorr: hand exoskeleton rehabilitation robot,” *Journal of neuroengineering and rehabilitation*, vol. 7, no. 1, p. 36, 2010.
- [9] E. Koeneman, R. Schultz, S. Wolf, D. Herring, and J. Koeneman, “A pneumatic muscle hand therapy device,” in *Engineering in Medicine and Biology Society, 2004. IEMBS’04. 26th Annual International Conference of the IEEE*, vol. 1, pp. 2711–2713, IEEE, 2004.
- [10] H. Taheri, J. B. Rowe, D. Gardner, V. Chan, K. Gray, C. Bower, D. J. Reinkensmeyer, and E. T. Wolbrecht, “Design and preliminary evaluation of the finger rehabilitation robot: controlling challenge and quantifying finger individuation during musical computer game play,” *Journal of neuroengineering and rehabilitation*, vol. 11, no. 1, p. 10, 2014.
- [11] A. Bataller, J. Cabrera, M. Clavijo, and J. Castillo, “Evolutionary synthesis of mechanisms applied to the design of an exoskeleton for finger rehabilitation,” *Mechanism and Machine Theory*, vol. 105, pp. 31–43, 2016.

- [12] T.-H. Hsu, Y.-C. Chiang, W.-T. Chan, and S.-J. Chen, “A finger exoskeleton robot for finger movement rehabilitation,” *Inventions*, vol. 2, no. 3, p. 12, 2017.
- [13] E. B. Brokaw, I. Black, R. J. Holley, and P. S. Lum, “Hand spring operated movement enhancer (handsome): a portable, passive hand exoskeleton for stroke rehabilitation,” *IEEE Transactions on Neural Systems and Rehabilitation Engineering*, vol. 19, no. 4, pp. 391–399, 2011.
- [14] N. Robson and G. S. Soh, “Geometric design of eight-bar wearable devices based on limb physiological contact task,” *Mechanism and Machine Theory*, vol. 100, pp. 358–367, 2016.
- [15] M. Fontana, S. Fabio, S. Marcheschi, and M. Bergamasco, “Haptic hand exoskeleton for precision grasp simulation,” *Journal of Mechanisms and Robotics*, vol. 5, no. 4, p. 041014, 2013.
- [16] O. Lambercy, D. Schröder, S. Zwicker, and R. Gassert, “Design of a thumb exoskeleton for hand rehabilitation,” in *Proceedings of the 7th International Convention on Rehabilitation Engineering and Assistive Technology*, p. 41, Singapore Therapeutic, Assistive & Rehabilitative Technologies (START) Centre, 2013.
- [17] N. Garcia-Hernandez, I. Sarakoglou, N. Tsagarakis, and D. Caldwell, “Under-actuated hand exoskeleton with novel kinematics for potential use in rehabilitation,” EuroHaptics, 2014.
- [18] R. Zheng and J. Li, “Kinematics and workspace analysis of an exoskeleton for thumb and index finger rehabilitation,” in *Robotics and Biomimetics (ROBIO), 2010 IEEE International Conference on*, pp. 80–84, IEEE, 2010.
- [19] S. Ueki, H. Kawasaki, S. Ito, Y. Nishimoto, M. Abe, T. Aoki, Y. Ishigure, T. Ojika, and T. Mouri, “Development of a hand-assist robot with multi-degrees-of-freedom for rehabilitation therapy,” *IEEE/ASME Transactions on Mechatronics*, vol. 17, no. 1, pp. 136–146, 2012.
- [20] Y. Yihun, R. Miklos, A. Perez-Gracia, D. J. Reinkensmeyer, K. Denney, and E. T. Wolbrecht, “Single degree-of-freedom exoskeleton mechanism design for thumb rehabilitation,” in *Engineering in medicine and biology society (EMBC), 2012 annual international conference of the IEEE*, pp. 1916–1920, IEEE, 2012.
- [21] S. S. Nishad, A. Dutta, and A. Saxena, “Design and control of a three finger hand exoskeleton for translation of a slender object,” in *Ubiquitous Robots and Ambient Intelligence (URAI), 2014 11th International Conference on*, pp. 179–184, IEEE, 2014.
- [22] D. Leonardis, M. Barsotti, C. Loconsole, M. Solazzi, M. Troncossi, C. Mazzotti, V. P. Castelli, C. Procopio, G. Lamola, C. Chisari, *et al.*, “An emg-controlled robotic hand exoskeleton for bilateral rehabilitation,” *IEEE transactions on haptics*, vol. 8, no. 2, pp. 140–151, 2015.

- [23] E. T. Wolbrecht, K. J. Morse, J. C. Perry, and D. J. Reinkensmeyer, "Design of a thumb module for the finger rehabilitation robot," in *Engineering in Medicine and Biology Society (EMBC), 2016 IEEE 38th Annual International Conference of the*, pp. 582–585, IEEE, 2016.
- [24] H. Schmidt, C. Werner, R. Bernhardt, S. Hesse, and J. Krüger, "Gait rehabilitation machines based on programmable footplates," *Journal of neuroengineering and rehabilitation*, vol. 4, no. 1, p. 2, 2007.
- [25] L. Lunenburger, G. Colombo, R. Riener, and V. Dietz, "Clinical assessments performed during robotic rehabilitation by the gait training robot lokomat," in *Rehabilitation Robotics, 2005. ICORR 2005. 9th International Conference on*, pp. 345–348, IEEE, 2005.
- [26] D. J. Reinkensmeyer, D. Aoyagi, J. L. Emken, J. A. Galvez, *et al.*, "Tools for understanding and optimizing robotic gait training," *Journal of rehabilitation research and development*, vol. 43, no. 5, p. 657, 2006.
- [27] J. F. Veneman, R. Kruidhof, E. E. Hekman, R. Ekkelenkamp, E. H. Van Asseldonk, and H. Van Der Kooij, "Design and evaluation of the lopes exoskeleton robot for interactive gait rehabilitation," *IEEE Transactions on Neural Systems and Rehabilitation Engineering*, vol. 15, no. 3, pp. 379–386, 2007.
- [28] S. K. Banala, S. K. Agrawal, and J. P. Scholz, "Active leg exoskeleton (alex) for gait rehabilitation of motor-impaired patients," in *Rehabilitation Robotics, 2007. ICORR 2007. IEEE 10th International Conference on*, pp. 401–407, IEEE, 2007.
- [29] S. Viteckova, P. Kutilek, and M. Jirina, "Wearable lower limb robotics: A review," *Biocybernetics and Biomedical Engineering*, vol. 33, no. 2, pp. 96–105, 2013.
- [30] G. Colombo, M. Joerg, R. Schreier, and V. Dietz, "Treadmill training of paraplegic patients using a robotic orthosis," *Journal of rehabilitation research and development*, vol. 37, no. 6, p. 693, 2000.
- [31] Z. Ji and Y. Manna, "Synthesis of a pattern generation mechanism for gait rehabilitation," *Journal of Medical Devices*, vol. 2, no. 3, p. 031004, 2008.
- [32] B. Y. Tsuge and J. M. McCarthy, "Synthesis of a 10-bar linkage to guide the gait cycle of the human leg," in *ASME 2015 International Design Engineering Technical Conferences and Computers and Information in Engineering Conference*, pp. V05BT08A083–V05BT08A083, American Society of Mechanical Engineers, 2015.
- [33] Y. Shao, Z. Xiang, H. Liu, and L. Li, "Conceptual design and dimensional synthesis of cam-linkage mechanisms for gait rehabilitation," *Mechanism and Machine Theory*, vol. 104, pp. 31–42, 2016.
- [34] B. Talu and Z. Bazancir, "The effect of different ankle and knee supports on balance in early ambulation of post-stroke hemiplegic patients," *Neurological Sciences*, vol. 38, no. 10, pp. 1811–1816, 2017.

- [35] F.-C. Wang, C.-H. Yu, T.-Y. Chou, and N.-C. Chang, “Design and control of an active gait trainer,” in *Industrial Electronics, 2009. ISIE 2009. IEEE International Symposium on*, pp. 1779–1784, IEEE, 2009.
- [36] P. Berkelman, P. Rossi, T. Lu, and J. Ma, “Passive orthosis linkage for locomotor rehabilitation,” in *Rehabilitation Robotics, 2007. ICORR 2007. IEEE 10th International Conference on*, pp. 425–431, IEEE, 2007.
- [37] S. K. Banala, S. K. Agrawal, A. Fattah, V. Krishnamoorthy, W.-L. Hsu, J. Scholz, and K. Rudolph, “Gravity-balancing leg orthosis and its performance evaluation,” *IEEE Transactions on Robotics*, vol. 22, no. 6, pp. 1228–1239, 2006.
- [38] J. O’Connor, D. McCaughan, C. McDaid, A. Booth, D. Fayter, R. Rodriguez-Lopez, R. Bowers, L. Dyson, C. P. Iglesias, S. Lalor, *et al.*, “Orthotic management of instability of the knee related to neuromuscular and central nervous system disorders: systematic review, qualitative study, survey and costing analysis.,” *Health Technology Assessment*, vol. 20, no. 55, 2016.
- [39] “Kafo custom products by collier orthotics in sacramento, ca.”
- [40] M. Eriksson, L. Villard, and Å. Bartonek, “Walking, orthoses and physical effort in a swedish population with arthrogryposis,” *Journal of children’s orthopaedics*, vol. 8, no. 4, pp. 305–312, 2014.
- [41] H. Uustal, “Prosthetics and orthotics,” *Essential Physical Medicine and Rehabilitation*, pp. 101–118, 2006.
- [42] M. Rafiaei, M. Bahramizadeh, M. Arazpour, M. Samadian, S. W. Hutchins, F. Farahmand, and M. A. Mardani, “The gait and energy efficiency of stance control knee–ankle–foot orthoses: A literature review,” *Prosthetics and orthotics international*, vol. 40, no. 2, pp. 202–214, 2016.
- [43] E. Pröbsting, A. Kannenberg, and B. Zacharias, “Safety and walking ability of kafo users with the c-brace® orthotronic mobility system, a new microprocessor stance and swing control orthosis,” *Prosthetics and orthotics international*, vol. 41, no. 1, pp. 65–77, 2017.
- [44] T. Yakimovich, E. Lemaire, and J. Kofman, “Engineering design review of stance-control knee-ankle-foot orthoses.,” *Journal of rehabilitation research and development*, vol. 46, no. 2, pp. 257–267, 2008.
- [45] J. W. Michael, “Summary from the academys seventh state-of-the-science conference on knee-ankle-foot orthoses for ambulation,” *JPO: Journal of Prosthetics and Orthotics*, vol. 18, no. 7, pp. P132–P136, 2006.
- [46] E. Perreault, L. Hargrove, D. Ludvig, H. Lee, and J. Sensinger, “Considering limb impedance in the design and control of prosthetic devices,” in *Neuro-Robotics*, pp. 59–83, Springer, 2014.

- [47] M. Arazpour, M. Ahmadi Bani, M. Samadian, M. E. Mousavi, S. W. Hutchins, M. Bahramizadeh, S. Curran, and M. A. Mardani, “The physiological cost index of walking with a powered knee–ankle–foot orthosis in subjects with poliomyelitis: A pilot study,” *Prosthetics and orthotics international*, vol. 40, no. 4, pp. 454–459, 2016.
- [48] B.-S. Yang, Y.-W. Chen, and J.-R. Tong, “User experience of lower-limb orthosis,” *Assistive Technology*, pp. 1–7, 2017.
- [49] C. McDaid, D. Fayter, A. Booth, J. O’Connor, R. Rodriguez-Lopez, D. McCaughan, R. Bowers, C. P. Iglesias, S. Lalor, R. J. O’Connor, *et al.*, “Systematic review of the evidence on orthotic devices for the management of knee instability related to neuromuscular and central nervous system disorders,” *BMJ open*, vol. 7, no. 9, p. e015927, 2017.
- [50] R. Foster and J. Milani, “The genucentric knee orthosis a new concept,” *Orthotics and Prosthetics*, vol. 33, no. 2, pp. 31–44, 1979.
- [51] P. Walker, H. Kurosawa, J. Rovick, and R. Zimmerman, “External knee joint design based on normal motion,” *J Rehabil Res Dev*, vol. 22, no. 1, pp. 9–22, 1985.
- [52] J. Townsend and S. Knecht, “Tension assisted ankle joint and orthotic limb braces incorporating same,” June 22 2004. US Patent 6,752,774.
- [53] C. Radcliffe, “Four-bar linkage prosthetic knee mechanisms: kinematics, alignment and prescription criteria,” *Prosthetics and orthotics international*, vol. 18, no. 3, pp. 159–173, 1994.
- [54] J. De Vries, “Conventional 4-bar linkage knee mechanisms: a strength-weakness analysis,” *Journal of rehabilitation research and development*, vol. 32, no. 1, pp. 36–42, 1995.
- [55] J. H. Townsend and R. J. Williams, “Multiaxis controlled motion knee brace with a four bar joint and method for producing same,” July 19 1994. US Patent 5,330,418.
- [56] J. M. B. Bertomeu, J. M. B. Lois, R. B. Guillem, Á. P. Del Pozo, J. Lacuesta, C. G. Mollà, P. V. Luna, and J. P. Pastor, “Development of a hinge compatible with the kinematics of the knee joint,” *Prosthetics and orthotics international*, vol. 31, no. 4, pp. 371–383, 2007.
- [57] G. M. Bapat and S. Sujatha, “A method for optimal synthesis of a biomimetic four-bar linkage knee joint for a knee-ankle-foot orthosis,” in *Journal of Biomimetics, Biomaterials and Biomedical Engineering*, vol. 32, pp. 20–28, Trans Tech Publ, 2017.
- [58] D. Jin, R. Zhang, H. Dimo, R. Wang, and J. Zhang, “Kinematic and dynamic performance of prosthetic knee joint using six-bar mechanism,” *Journal of rehabilitation research and development*, vol. 40, no. 1, pp. 39–48, 2003.

- [59] N. Sancisi, R. Caminati, and V. Parenti-Castelli, “Optimal four-bar linkage for the stability and the motion of the human knee prostheses,” in *Atti del XIX CONGRESSO dell’Associazione Italiana di Meccanica Teorica e Applicata*. Ancona, pp. 1–10, 2009.
- [60] A. Hamon and Y. Aoustin, “Cross four-bar linkage for the knees of a planar bipedal robot,” in *Humanoid Robots (Humanoids), 2010 10th IEEE-RAS International Conference on*, pp. 379–384, IEEE, 2010.
- [61] H.-L. Xie, Z.-Z. Liang, F. Li, and L.-X. Guo, “The knee joint design and control of above-knee intelligent bionic leg based on magneto-rheological damper,” *International Journal of Automation and Computing*, vol. 7, no. 3, pp. 277–282, 2010.
- [62] M. P. Kadaba, H. Ramakrishnan, and M. Wootten, “Measurement of lower extremity kinematics during level walking,” *Journal of orthopaedic research*, vol. 8, no. 3, pp. 383–392, 1990.
- [63] K. R. Luker, A. Aguinaldo, D. Kenney, K. Cahill-Rowley, and A. L. Ladd, “Functional task kinematics of the thumb carpometacarpal joint,” *Clinical Orthopaedics and Related Research*®, vol. 472, no. 4, pp. 1123–1129, 2014.
- [64] F. H. Netter, *Atlas of Human Anatomy, Professional Edition E-Book: including Netter-Reference. com Access with Full Downloadable Image Bank*. Elsevier Health Sciences, 2014.
- [65] J. O’connor, T. Shercliff, E. Biden, and J. Goodfellow, “The geometry of the knee in the sagittal plane,” *Proceedings of the Institution of Mechanical Engineers, Part H: Journal of Engineering in Medicine*, vol. 203, no. 4, pp. 223–233, 1989.
- [66] V. Parenti-Castelli, A. Leardini, R. Di Gregorio, and J. J. O’connor, “On the modeling of passive motion of the human knee joint by means of equivalent planar and spatial parallel mechanisms,” *Autonomous Robots*, vol. 16, no. 2, pp. 219–232, 2004.
- [67] J. R. Nymark, S. J. Balmer, E. H. Melis, E. D. Lemaire, and S. Millar, “Electromyographic and kinematic nondisabled gait differences at extremely slow overground and treadmill walking speeds,” *Journal of rehabilitation research and development*, vol. 42, no. 4, p. 523, 2005.
- [68] Y. Okita, N. Tatematsu, K. Nagai, T. Nakayama, T. Nakamata, T. Okamoto, J. Toguchida, N. Ichihashi, S. Matsuda, and T. Tsuboyama, “The effect of walking speed on gait kinematics and kinetics after endoprosthetic knee replacement following bone tumor resection,” *Gait & posture*, vol. 40, no. 4, pp. 622–627, 2014.
- [69] J. Wang, J. Li, Y. Zhang, and S. Wang, “Design of an exoskeleton for index finger rehabilitation,” in *Engineering in Medicine and Biology Society, 2009. EMBC 2009. Annual International Conference of the IEEE*, pp. 5957–5960, IEEE, 2009.
- [70] J. M. McCarthy and G. S. Soh, *Geometric design of linkages*, vol. 11. Springer Science & Business Media, 2010.

- [71] M. M. Plecnik and J. M. McCarthy, “Design of Stephenson linkages that guide a point along a specified trajectory,” *Mechanism and Machine Theory*, vol. 96, pp. 38–51, 2016.
- [72] M. M. Plecnik and J. M. McCarthy, “Computational Design of Stephenson II Six-bar Function Generators for 11 Accuracy Points,” *Journal of Mechanisms and Robotics*, vol. 8, no. 1, p. 011017, 2016.
- [73] R. Sancibrian, F. Viadero, P. Garcia, and A. Fernández, “Gradient-based optimization of path synthesis problems in planar mechanisms,” *Mechanism and machine theory*, vol. 39, no. 8, pp. 839–856, 2004.
- [74] J. Cabrera, A. Ortiz, F. Nadal, and J. Castillo, “An evolutionary algorithm for path synthesis of mechanisms,” *Mechanism and Machine Theory*, vol. 46, no. 2, pp. 127–141, 2011.
- [75] I. Ullah and S. Kota, “Optimal synthesis of mechanisms for path generation using fourier descriptors and global search methods,” *Journal of Mechanical Design*, vol. 119, no. 4, pp. 504–510, 1997.
- [76] H. Zhou and E. H. Cheung, “Optimal synthesis of crank–rocker linkages for path generation using the orientation structural error of the fixed link,” *Mechanism and Machine Theory*, vol. 36, no. 8, pp. 973–982, 2001.
- [77] A. Sedano, R. Sancibrian, A. de Juan, F. Viadero, and F. Egana, “Hybrid optimization approach for the design of mechanisms using a new error estimator,” *Mathematical Problems in Engineering*, vol. 2012, 2012.
- [78] S. B. Matekar and G. R. Gogate, “Optimum synthesis of path generating four-bar mechanisms using differential evolution and a modified error function,” *Mechanism and Machine Theory*, vol. 52, pp. 158–179, 2012.
- [79] J. Buśkiewicz, “A method for optimal path synthesis of four-link planar mechanisms,” *Inverse Problems in Science and Engineering*, vol. 23, no. 5, pp. 818–850, 2015.
- [80] F. Nadal, J. A. Cabrera, A. Bataller, J. J. Castillo, and A. Ortiz, “Turning functions in optimal synthesis of mechanisms,” *Journal of Mechanical Design*, vol. 137, no. 6, p. 062302, 2015.
- [81] J.-W. Kim, T. Seo, and J. Kim, “A new design methodology for four-bar linkage mechanisms based on derivations of coupler curve,” *Mechanism and Machine Theory*, vol. 100, pp. 138–154, 2016.
- [82] S. H. Kafash and A. Nahvi, “Optimal synthesis of four-bar path generator linkages using circular proximity function,” *Mechanism and Machine Theory*, vol. 115, pp. 18–34, 2017.
- [83] B. Y. Tsuge, M. M. Plecnik, and J. M. McCarthy, “Homotopy directed optimization to design a six-bar linkage for a lower limb with a natural ankle trajectory,” *Journal of Mechanisms and Robotics*, vol. 8, no. 6, p. 061009, 2016.

- [84] R. Storn and K. Price, “Differential evolution—a simple and efficient heuristic for global optimization over continuous spaces,” *Journal of global optimization*, vol. 11, no. 4, pp. 341–359, 1997.
- [85] A. A. Smaili, N. A. Diab, and N. A. Atallah, “Optimum synthesis of mechanisms using tabu-gradient search algorithm,” *Journal of Mechanical Design*, vol. 127, no. 5, pp. 917–923, 2005.
- [86] J. Cabrera, A. Simon, and M. Prado, “Optimal synthesis of mechanisms with genetic algorithms,” *Mechanism and Machine theory*, vol. 37, no. 10, pp. 1165–1177, 2002.
- [87] R. R. Bulatovic, S. R. Dordevic, and V. S. Dordevic, “Cuckoo search algorithm: a metaheuristic approach to solving the problem of optimum synthesis of a six-bar double dwell linkage,” *Mechanism and Machine Theory*, vol. 61, pp. 1–13, 2013.
- [88] S. Ebrahimi and P. Payvandy, “Efficient constrained synthesis of path generating four-bar mechanisms based on the heuristic optimization algorithms,” *Mechanism and Machine Theory*, vol. 85, pp. 189–204, 2015.
- [89] R. R. Bulatovic, G. Miodragovic, and M. S. Boskovic, “Modified krill herd (mkh) algorithm and its application in dimensional synthesis of a four-bar linkage,” *Mechanism and Machine Theory*, vol. 95, pp. 1–21, 2016.
- [90] M. Laribi, A. Mlika, L. Romdhane, and S. Zeghloul, “A combined genetic algorithm–fuzzy logic method (ga–fl) in mechanisms synthesis,” *Mechanism and machine theory*, vol. 39, no. 7, pp. 717–735, 2004.
- [91] W.-Y. Lin, “A ga–de hybrid evolutionary algorithm for path synthesis of four-bar linkage,” *Mechanism and Machine Theory*, vol. 45, no. 8, pp. 1096–1107, 2010.
- [92] Y. Hongying, T. Dewei, and W. Zhixing, “Study on a new computer path synthesis method of a four-bar linkage,” *Mechanism and machine theory*, vol. 42, no. 4, pp. 383–392, 2007.
- [93] N. P. Robson and J. M. McCarthy, “Kinematic synthesis with contact direction and curvature constraints on the workpiece,” in *ASME 2007 International Design Engineering Technical Conferences and Computers and Information in Engineering Conference*, pp. 581–588, American Society of Mechanical Engineers, 2007.
- [94] N. P. Robson and J. M. McCarthy, “Second order task specifications in the geometric design of spatial mechanical linkages,” *International Journal of Modern Engineering*, vol. 11, 2010.
- [95] B. Hunter, “Hands-free crutch,” July 6 2016. US Patent App. 15/203,409.
- [96] M. M. Plecnik and J. M. McCarthy, “Controlling the movement of a TRR spatial chain with coupled six-bar function generators for biomimetic motion,” *Journal of Mechanisms and Robotics*, vol. 8, no. 5, p. 051005, 2016.

- [97] D. J. Bates, J. D. Hauenstein, A. J. Sommese, and C. W. Wampler, “Bertini: Software for numerical algebraic geometry.” Available at [bertini.nd.edu](http://bertini.nd.edu) with permanent doi: [dx.doi.org/10.7274/R0H41PB5](https://doi.org/10.7274/R0H41PB5).
- [98] C. Gosselin and J. Angeles, “Singularity analysis of closed-loop kinematic chains,” *IEEE transactions on robotics and automation*, vol. 6, no. 3, pp. 281–290, 1990.

# Appendix A

## Mathematica Code

### A.1 Import and Plot Motion Capture Data

```
(* Import gait data for lower-leg *)
SetDirectory[NotebookDirectory[]];
NotebookDirectory[];
directoryName = NotebookDirectory[] <> "Walk_data0001_pos.tsv";
WalkData1 = Import[directoryName]
Table[{i, WalkData1[[1, i]]}, {i, Length[WalkData1[[1]]}]
(* Sample lower-leg mocap data *)
{{1, "Frame"}, {2, "Time"}, {3, "Lthigh2_pos_X"}, {4, "Lthigh2_pos_Y"}, {5,
  "Lthigh2_pos_Z"}, {6, "LKnee_pos_X"}, {7, "LKnee_pos_Y"}, {8,
  "LKnee_pos_Z"}, {9, "Lheel_pos_X"}, {10, "Lheel_pos_Y"}, {11,
  "Lheel_pos_Z"}, {12, "Ltoe_pos_X"}, {13, "Ltoe_pos_Y"}, {14,
  "Ltoe_pos_Z"}, {15, "Back_pos_X"}, {16, "Back_pos_Y"}, {17,
  "Back_pos_Z"}, {18, "RpelvisBack_pos_X"}, {19, "RpelvisBack_pos_Y"}, {20,
```

```

"RpelvisBack_pos_Z"}, {21, "RpelvisFront_pos_X"}, {22,
"RpelvisFront_pos_Y"}, {23, "RpelvisFront_pos_Z"}, {24,
"Rthigh1_pos_X"}, {25, "Rthigh1_pos_Y"}, {26, "Rthigh1_pos_Z"}, {27,
"Rthigh2_pos_X"}, {28, "Rthigh2_pos_Y"}, {29, "Rthigh2_pos_Z"}, {30,
"Rknee_pos_X"}, {31, "Rknee_pos_Y"}, {32, "Rknee_pos_Z"}, {33,
"Rcalf1_pos_X"}, {34, "Rcalf1_pos_Y"}, {35, "Rcalf1_pos_Z"}, {36,
"Rcalf2_pos_X"}, {37, "Rcalf2_pos_Y"}, {38, "Rcalf2_pos_Z"}, {39,
"Rankle_pos_X"}, {40, "Rankle_pos_Y"}, {41, "Rankle_pos_Z"}, {42,
"Rtoe_pos_X"}, {43, "Rtoe_pos_Y"}, {44, "Rtoe_pos_Z"}, {45,
"Rheel_pos_X"}, {46, "Rheel_pos_Y"}, {47, "Rheel_pos_Z"}, {48,
"LpelvisBack_pos_X"}, {49, "LpelvisBack_pos_Y"}, {50,
"LpelvisBack_pos_Z"}, {51, "LpelvisFront_pos_X"}, {52,
"LpelvisFront_pos_Y"}, {53, "LpelvisFront_pos_Z"}, {54,
"Lthigh1_pos_X"}, {55, "Lthigh1_pos_Y"}, {56, "Lthigh1_pos_Z"}, {57,
"Lcalf1_pos_X"}, {58, "Lcalf1_pos_Y"}, {59, "Lcalf1_pos_Z"}, {60,
"Lcalf2_pos_X"}, {61, "Lcalf2_pos_Y"}, {62, "Lcalf2_pos_Z"}, {63,
"Lankle_pos_X"}, {64, "Lankle_pos_Y"}, {65, "Lankle_pos_Z"}}
(* Sort Data According to Marker Names*)
WalkData2 = Transpose[Rest[WalkData1]];
dataPoints =
  Table[MapThread[{{#1, #2, #3} &, WalkData2[[i ;; i + 2]]], {i, 3, 63, 3}];
{Lthigh2, Lknee, Lheel, Ltoe, Backk, RpelvisBack, RpelvisFront, Rthigh1,
  Rthigh2, Rknee, Rcalf1, Rcalf2, Rankle, Rtoe, Rheel, LpelvisBack,
  LpelvisFront, Lthigh1, Lcalf1, Lcalf2, Lankle} = dataPoints;

(* Plot 3D data *)
Manipulate[

```

```

Graphics3D[{
  PointSize[Large], Map[Point[#] &, dataPoints[[All, frame]]],
  Red, Line[{Backk, LpelvisBack, LpelvisFront, Lthigh1, Lthigh2, Lknee,
    Lcalf1, Lcalf2, Lankle, Lheel, Ltoe}[[All, frame]]],
  Blue, Line[{Backk, RpelvisBack, RpelvisFront, Rthigh1, Rthigh2, Rknee,
    Rcalf1, Rcalf2, Rankle, Rheel, Rtoe}[[All, frame]]]
}, Axes -> True, PlotRange -> {{-200, 800}, {-200, 400}, {-100, 1200}},
  AxesLabel -> {x, y, z}
, {frame, 1, Length[dataPoints[[1]]], 1}]

```

(\* Obtain 2D data from 3D \*)

```

dataPoints2D = Apply[{-#1, #3} &, dataPoints, {2}];
{Lthigh22D, Lknee2D, Lheel2D, Ltoe2D, Back2D,
RpelvisBack2D, RpelvisFront2D,
  Rthigh12D, Rthigh22D, Rknee2D, Rcalf12D, Rcalf22D, Rankle2D, Rtoe2D,
  Rheel2D, LpelvisBack2D, LpelvisFront2D, Lthigh12D, Lcalf12D, Lcalf22D,
  Lankle2D} = dataPoints2D;

```

(\* Plot 2D gait data \*)

```

Manipulate[
  Graphics[{
    PointSize[0.025], Map[Point[#] &, dataPoints2D[[All, frame]]],
    Thickness[0.009], Red,
    Line[{Back2D, LpelvisBack2D, LpelvisFront2D, Lthigh12D, Lthigh22D, Lknee2D,
      Lcalf12D, Lcalf22D, Lankle2D, Lheel2D, Ltoe2D, Lankle2D}[[All, frame]]],
    Blue, Line[{Back2D, RpelvisBack2D, RpelvisFront2D, Rthigh12D, Rthigh22D,
      Rknee2D, Rcalf12D, Rcalf22D, Rankle2D, Rheel2D, Rtoe2D, Rankle2D}[[All,

```

```

    frame]]],
Black, Text[Style["Sacral", 26], Back2D[[frame]] + {10, 25}],
Text[Style["LBack", 26], LpelvisBack2D[[frame]] + {-30, -30}],
Text[Style["LHip", 26], LpelvisFront2D[[frame]] + {-45, -25}],
Text[Style["LThigh1", 26], Lthigh12D[[frame]] + {-80, 0}],
Text[Style["LThigh2", 26], Lthigh22D[[frame]] + {-80, 0}],
Text[Style["LKnee", 26], Lknee2D[[frame]] + {-70, 0}],
Text[Style["LCalf1", 26], Lcalf12D[[frame]] + {-70, 0}],
Text[Style["LCalf2", 26], Lcalf22D[[frame]] + {-70, 0}],
Text[Style["LAnkle", 26], Lankle2D[[frame]] + {70, 0}],
Text[Style["LHeel", 26], Lheel2D[[frame]] + {-70, 0}],
Text[Style["LToe", 26], Ltoe2D[[frame]] + {70, -20}],
Text[Style["RBack", 26], RpelvisBack2D[[frame]] + {30, 30}],
Text[Style["RHip", 26], RpelvisFront2D[[frame]] + {45, 25}],
Text[Style["RThigh1", 26], Rthigh12D[[frame]] + {90, 0}],
Text[Style["RThigh2", 26], Rthigh22D[[frame]] + {90, 0}],
Text[Style["RKnee", 26], Rknee2D[[frame]] + {70, 0}],
Text[Style["RCalf1", 26], Rcalf12D[[frame]] + {70, 0}],
Text[Style["RCalf2", 26], Rcalf22D[[frame]] + {70, 0}],
Text[Style["RAnkle", 26], Rankle2D[[frame]] + {70, 20}],
Text[Style["RHeel", 26], Rheel2D[[frame]] + {-70, -10}],
Text[Style["RToe", 26], Rtoe2D[[frame]] + {90, 0}
}, Axes -> True, PlotRange -> {{-800, 200}, {-100, 1200}},
AxesLabel -> {x, z}, AxesOrigin -> {200, 0}, (*ImageSize\[Rule]800,*)
AxesStyle -> Directive[Black, 26]]
, {frame, 1, Length[dataPoints[[1]]], 1}]

```

### A.1.1 Transformation of Lower-leg Data

```
DHom[\[Theta]_, {dx_, dy_}] := {{Cos[\[Theta]], -Sin[\[Theta]],
  dx}, {Sin[\[Theta]], Cos[\[Theta]], dy}, {0, 0, 1}}
DHomPts[pt1_, pt2_] := Module[{d, vect, \[Theta]},
  d = pt1;
  vect = pt2 - pt1;
  \[Theta] = ArcTan[vect[[1]], vect[[2]]];
  DHom[\[Theta], d]
DHomPtsHip[pt1_, pt2_] := Module[{d, vect, \[Theta]},
  d = pt1;
  vect = pt2 - pt1;
  \[Theta] = ArcTan[vect[[1]], vect[[2]]];
  DHom[\[Theta] + \[Pi], d]
hipFrame =
  MapThread[DHomPtsHip[#1, #2] &, {LpelvisFront2D, LpelvisBack2D}];
thighFrame = MapThread[DHomPts[#1, #2] &, {Lthigh12D, Lthigh22D}];
calfFrame = MapThread[DHomPts[#1, #2] &, {Lcalf12D, Lcalf22D}];
footFrame = MapThread[DHomPts[#1, #2] &, {Lankle2D, Ltoe2D}];
thighFrame = Map[#.DHom[\[Pi]/2, {0, 0}] &, thighFrame];
calfFrame = Map[#.DHom[\[Pi]/2, {0, 0}] &, calfFrame];
DrawTaskFrame[taskFrame_] := Module[{e1, e2, d, sc},
  e1 = taskFrame[{{1, 2}, 1}];
  e2 = taskFrame[{{1, 2}, 2}];
  d = taskFrame[{{1, 2}, 3}];
  sc = 100;
  {Line[{d, d + sc*e1}], Line[{d, d + sc*e2}]}
```

```

hipFrameThF = MapThread[Inverse[#2].#1 &, {hipFrame, thighFrame}];
thighFrameThF = MapThread[Inverse[#2].#1 &, {thighFrame, thighFrame}];
calfFrameThF = MapThread[Inverse[#2].#1 &, {calfFrame, thighFrame}];
footFrameThF = MapThread[Inverse[#2].#1 &, {footFrame, thighFrame}];
dataPoints2DThF =
  Table[MapThread[
    Most[Inverse[#1].Append[#2, 1]] &, {thighFrame,
      dataPoints2D[[i]]}], {i, Length[dataPoints2D]}];
{Lthigh22DThF, Lknee2DThF, Lheel2DThF, Ltoe2DThF, Back2DThF,
  RpelvisBack2DThF, RpelvisFront2DThF, Rthigh12DThF, Rthigh22DThF,
  Rknee2DThF, Rcalf12DThF, Rcalf22DThF, Rankle2DThF, Rtoe2DThF,
  Rheel2DThF, LpelvisBack2DThF, LpelvisFront2DThF, Lthigh12DThF,
  Lcalf12DThF, Lcalf22DThF, Lankle2DThF} = dataPoints2DThF;

c1ThF = Ltoe2DThF[[164 ;; 279]];
c2ThF = Ltoe2DThF[[279 ;; 394]];
c3ThF = Ltoe2DThF[[509 ;; 624]];
c4ThF = Ltoe2DThF[[624 ;; 739]];
c5ThF = Ltoe2DThF[[739 ;; 854]];
c6ThF = Ltoe2DThF[[854 ;; 969]];
avgLtoe2DThF = Mean[{c1ThF, c2ThF, c3ThF, c4ThF, c5ThF, c6ThF}];

InvKin2R[\[ScriptCapitalK]_, l1_, l2_, \[ScriptCapitalP]_] :=
Module[{K, P, Z, V},
  {K, P} =
    Apply[#1 + #2*I &, {\[ScriptCapitalK], \[ScriptCapitalP]}, 1];

```

```

Z = Map[
  1/(2*l1*l2)*((P - K)*(P\[Conjugate] - K\[Conjugate]) - l1^2 -
    l2^2 + #*
    Sqrt[((P - K)*(P\[Conjugate] - K\[Conjugate]) - l1^2 -
      l2^2)^2 - 4*l1^2*l2^2]) &, {+1, -1}];
V = Map[(P - K)/(l1 + #*l2) &, Z];
MapThread[{Arg[#1], Arg[#2]} &, {V, Z}]
Manipulate[
  toePoint = {toePointx, toePointy, 1};
  toePointThF = Map[Most[#.toePoint] &, footFrameThF];
  kneePoint = {kneePointx, kneePointy};
  RRangles = Map[InvKin2R[kneePoint, l1, l2, #][[1]] &, toePointThF];
  Lpoint = Map[kneePoint + l1*{Cos[#], Sin[#]} &, RRangles[[All, 1]]];
  plot = Graphics[{
    Thickness[0.005], Lighter[Gray], Line[c1ThF],
    Line[c2ThF],
    Line[c3ThF],
    Line[c4ThF],
    Line[c5ThF],
    Line[c6ThF],
    Black, Thickness[0.004], Line[avgLtoe2DThF],
    PointSize[0.015], Map[Point[#] &, dataPoints2DThF[[All, frame]]],
    Red, Thickness[0.007],
    Line[{Back2DThF, LpelvisBack2DThF, LpelvisFront2DThF,
      Lthigh12DThF, Lthigh22DThF, Lknee2DThF, Lcalf12DThF,
      Lcalf22DThF, Lankle2DThF, Lheel2DThF, Ltoe2DThF, Lankle2DThF}][[
    All, frame]]],

```

```

Blue, Thickness[0.003],
Line[{Back2DThF, RpelvisBack2DThF, RpelvisFront2DThF,
      Rthigh12DThF, Rthigh22DThF, Rknee2DThF, Rcalf12DThF,
      Rcalf22DThF, Rankle2DThF, Rheel2DThF, Rtoe2DThF, Rankle2DThF}[[
      All, frame]]],
Thickness[0.005], Darker[Green],
DrawTaskFrame[hipFrameThF[[frame]]],
DrawTaskFrame[thighFrameThF[[frame]]],
DrawTaskFrame[calfFrameThF[[frame]]],
DrawTaskFrame[footFrameThF[[frame]]],
(*Blue,PointSize[0.01],Table[Point[toePointThF[[i]]],{i,{1,5,9,17,
31,38,41,46,72,98,110}}],*)
Magenta, Point[toePointThF[[frame]]],
Point[kneePoint],
Point[Lpoint[[frame]]],
Line[{kneePoint, Lpoint[[frame]], toePointThF[[frame]]}],
Black, Text[Style["Sacral", 26], Back2DThF[[frame]] + {10, 25}],
Text[Style["LBack", 26], LpelvisBack2DThF[[frame]] + {-30, -30}],
Text[Style["LHip", 26], LpelvisFront2DThF[[frame]] + {45, -25}],
Text[Style["LThigh1", 26], Lthigh12DThF[[frame]] + {-60, 20}],
Text[Style["LThigh2", 26], Lthigh22DThF[[frame]] + {-60, 20}],
Text[Style["LKnee", 26], Lknee2DThF[[frame]] + {-70, 0}],
Text[Style["LCalf1", 26], Lcalf12DThF[[frame]] + {-70, 0}],
Text[Style["LCalf2", 26], Lcalf22DThF[[frame]] + {-70, 0}],
Text[Style["LAnkle", 26], Lankle2DThF[[frame]] + {70, 0}],
Text[Style["LHeel", 26], Lheel2DThF[[frame]] + {-90, 0}],
Text[Style["LToe", 26], Ltoe2DThF[[frame]] + {20, -30}],

```

```

Text[Style["RBack", 26], RpelvisBack2DThF[[frame]] + {30, 30}],
Text[Style["RHip", 26], RpelvisFront2DThF[[frame]] + {45, 25}],
Text[Style["RThigh1", 26], Rthigh12DThF[[frame]] + {90, 0}],
Text[Style["RThigh2", 26], Rthigh22DThF[[frame]] + {90, 0}],
Text[Style["RKnee", 26], Rknee2DThF[[frame]] + {70, 0}],
Text[Style["RCalf1", 26], Rcalf12DThF[[frame]] + {70, 0}],
Text[Style["RCalf2", 26], Rcalf22DThF[[frame]] + {70, 0}],
Text[Style["RAnkle", 26], Rankle2DThF[[frame]] + {50, 20}],
Text[Style["RHeel", 26], Rheel2DThF[[frame]] + {-50, 10}],
Text[Style["RToe", 26], Rtoe2DThF[[frame]] + {50, 0}]
}, Axes -> True, PlotRange -> {{-450, 550}, {-900, 300}},
AxesLabel -> {x, z}, AxesStyle -> Directive[Black, 28],
ImageSize -> 600];
{plot(*,toePointThF[[frame]]*)}
, {frame, 1, Length[Lthigh12DThF], 1}
, {{toePointx, 155}, 100, 300}
, {{toePointy, 0}, -50, 50}
, {{kneePointx, 0}, -200, 200}
, {{kneePointy, -370}, -450, -250}
, {{11, 405}, 300, 500}
, {{12, 155}, 100, 300}, ControlPlacement -> Bottom]

```

## A.1.2 Transformation of Thumb Data

```

rem = {{1, 0, 0, 0}, {0, 1, 0, 0}, {0, 0, 1, 0}};
Dd = Table[{{1, 0, 0, -ThumbMCP[[i, 1]]}, {0, 1,
0, -ThumbMCP[[i, 2]]}, {0, 0, 1, -ThumbMCP[[i, 3]]}, {0, 0, 0,

```

```

    1}}, {i, Length[ThumbMCP]}}];
dpMCPO = Table[
  Table[Flatten[
    rem.Dd[[i]].{{dataPoints[[j]][[i, 1]], {dataPoints[[j]][[i,
      2]]}, {dataPoints[[j]][[i, 3]]}, {1}}}, {i,
    Length[dataPoints[[1]]}], {j, Length[dataPoints]}}];
{Hand00, IndexMCPO, HandX0, MiddleMCPO, ThumbMCPO, ThumbIPO,
  ThumbTip0, IndexPIPO, IndexDIPO, IndexTIPO, MiddlePIPO, MiddleDIPO,
  MiddleTip0} = dpMCPO;
a1 = ThumbIPO[[;; , 1]];
b1 = ThumbIPO[[;; , 2]];
c1 = ThumbIPO[[;; , 3]];
l1 = Sqrt[a1^2 + b1^2 + c1^2];
v1 = Sqrt[b1^2 + c1^2];
rx = Table[ {{1, 0, 0, 0}, {0, c1[[i]]/v1[[i]], -b1[[i]]/v1[[i]],
  0}, {0, b1[[i]]/v1[[i]], c1[[i]]/v1[[i]], 0}, {0, 0, 0, 1}}, {i,
  Length[c1]}}];
dpMCP1 = Table[
  Table[Flatten[
    rem.rx[[i]].Dd[[
      i]].{{dataPoints[[j]][[i, 1]], {dataPoints[[j]][[i,
        2]]}, {dataPoints[[j]][[i, 3]]}, {1}}}, {i,
      Length[dataPoints[[1]]}], {j, Length[dataPoints]}}];
{Hand01, IndexMCP1, HandX1, MiddleMCP1, ThumbMCP1, ThumbIP1,
  ThumbTip1, IndexPIP1, IndexDIP1, IndexTIP1, MiddlePIP1, MiddleDIP1,
  MiddleTip1} = dpMCP1;
(* Plot the transformed data in 3D*)

```

```

Manipulate[
Graphics3D[{
  PointSize[Large], Map[Point[#] &, dpMCP1[[All, frame]]],
  Red, Line[{IndexMCP1, Hand01, HandX1}[[All, frame]]],
  Blue, Line[{ThumbMCP1, ThumbIP1, ThumbTip1}[[All, frame]]],
  Green,
  Line[{IndexMCP1, IndexPIP1, IndexDIP1, IndexTIP1}[[All, frame]]],
  Line[{MiddleMCP1, MiddlePIP1, MiddleDIP1, MiddleTip1}[[All, frame]]]
}, Axes -> True, AxesOrigin -> {0, 0, 0},
PlotRange -> {{-120, 20}, {-70, 70}, {-70, 70}},
AxesLabel -> {x, y, z}, ImageSize -> 600]
, {frame, 1, Length[dpMCP1[[1]]], 1}
(* Get 2D Data *)
dpMCP12D = Apply[{-#1, #3} &, dpMCP1, {2}];
{Hand012D, IndexMCP12D, HandX12D, MiddleMCP12D, ThumbMCP12D,
  ThumbIP12D, ThumbTip12D, IndexPIP12D, IndexDIP12D, IndexTIP12D,
  MiddlePIP12D, MiddleDIP12D, MiddleTip12D} = dpMCP12D;
(* Plot Planar thumb data *)

```

```

Manipulate[
Graphics[{
  PointSize[Large], Map[Point[#] &, dpMCP12D[[All, frame]]],
  PointSize[0.001], Point[ThumbTip12D],
  Red, Line[{IndexMCP12D, Hand012D, HandX12D}[[All, frame]]],
  Blue, Line[{ThumbMCP12D, ThumbIP12D, ThumbTip12D}[[All, frame]]],
  Green,
  Line[{IndexMCP12D, IndexPIP12D, IndexDIP12D, IndexTIP12D}[[All,
    frame]]],

```

```

Line[{MiddleMCP12D, MiddlePIP12D, MiddleDIP12D, MiddleTip12D}][[All,
    frame]]]
}, Axes -> True, PlotRange -> {{-10, 150}, {-100, 60}},
AxesLabel -> {x, z}]
, {frame, 1, Length[dpMCP12D[[1]]], 1}]

```

### A.1.3 Motion Capture Data for Thumb Trajectory

Three-dimensional motion capture data of the thumb of an individual.

```

{{52.6947, 41.835}, {52.6999, 41.8311}, {52.7063, 41.8267}, {52.7141,
    41.822}, {52.7231, 41.8169}, {52.7333, 41.8114}, {52.7446,
    41.8054}, {52.757, 41.7987}, {52.7703, 41.7913}, {52.7845,
    41.7831}, {52.7996, 41.774}, {52.8154, 41.7639}, {52.8319,
    41.7527}, {52.8491, 41.7403}, {52.8667, 41.7268}, {52.8848,
    41.7124}, {52.9032, 41.6973}, {52.9218, 41.6816}, {52.9404,
    41.6655}, {52.959, 41.6492}, {52.9774, 41.6328}, {52.9956,
    41.6166}, {53.0133, 41.6006}, {53.0306, 41.585}, {53.0472,
    41.5699}, {53.0634, 41.5551}, {53.079, 41.5402}, {53.0942,
    41.5252}, {53.1089, 41.5096}, {53.1232, 41.4934}, {53.1372,
    41.4762}, {53.1508, 41.4579}, {53.1641, 41.4381}, {53.1771,
    41.4167}, {53.19, 41.3934}, {53.2028, 41.3684}, {53.2159,
    41.342}, {53.2296, 41.3142}, {53.2441, 41.2853}, {53.2597,
    41.2555}, {53.2767, 41.225}, {53.2953, 41.1941}, {53.3158,
    41.1628}, {53.3385, 41.1316}, {53.3636, 41.1004}, {53.3912,
    41.0696}, {53.4209, 41.0391}, {53.4523, 41.0091}, {53.4852,
    40.9796}, {53.5192, 40.9507}, {53.5541, 40.9225}, {53.5895,

```

40.8951}, {53.625, 40.8685}, {53.6604, 40.8428}, {53.6953,  
40.8182}, {53.7295, 40.7946}, {53.7631, 40.7718}, {53.796,  
40.7496}, {53.8283, 40.7278}, {53.8602, 40.7062}, {53.8917,  
40.6845}, {53.9228, 40.6625}, {53.9536, 40.6399}, {53.9843,  
40.6167}, {54.0148, 40.5924}, {54.0452, 40.567}, {54.0757,  
40.5404}, {54.1063, 40.5129}, {54.1371, 40.4846}, {54.1682,  
40.4559}, {54.1998, 40.4268}, {54.2319, 40.3977}, {54.2647,  
40.3687}, {54.2982, 40.34}, {54.3325, 40.3118}, {54.3678,  
40.2844}, {54.404, 40.2578}, {54.441, 40.2318}, {54.4786,  
40.2063}, {54.5164, 40.181}, {54.5545, 40.1557}, {54.5924,  
40.1301}, {54.6301, 40.1042}, {54.6672, 40.0777}, {54.7036,  
40.0503}, {54.7392, 40.0218}, {54.7736, 39.9921}, {54.807,  
39.9613}, {54.8394, 39.9294}, {54.8712, 39.8965}, {54.9023,  
39.8629}, {54.9329, 39.8286}, {54.9633, 39.7937}, {54.9934,  
39.7584}, {55.0236, 39.7228}, {55.0538, 39.687}, {55.0843,  
39.6513}, {55.1151, 39.6155}, {55.1462, 39.5795}, {55.1773,  
39.5434}, {55.2084, 39.507}, {55.2393, 39.4701}, {55.2701,  
39.4327}, {55.3006, 39.3947}, {55.3306, 39.3559}, {55.3601,  
39.3163}, {55.3889, 39.2758}, {55.4171, 39.2342}, {55.445,  
39.1914}, {55.473, 39.1475}, {55.5015, 39.1022}, {55.531,  
39.0554}, {55.5618, 39.0071}, {55.5944, 38.9572}, {55.6292,  
38.9055}, {55.6666, 38.852}, {55.707, 38.7965}, {55.7509,  
38.7391}, {55.7983, 38.6796}, {55.8488, 38.618}, {55.9022,  
38.5545}, {55.9583, 38.489}, {56.0167, 38.4217}, {56.0771,  
38.3524}, {56.1393, 38.2813}, {56.203, 38.2083}, {56.2678,  
38.1336}, {56.3336, 38.0571}, {56.4, 37.9791}, {56.4665,  
37.9002}, {56.5326, 37.8211}, {56.5978, 37.7424}, {56.6616,

37.665}, {56.7236, 37.5895}, {56.7832, 37.5166}, {56.8399,  
37.447}, {56.8932, 37.3814}, {56.9428, 37.3205}, {56.988,  
37.2649}, {57.0293, 37.2142}, {57.0673, 37.1674}, {57.1028,  
37.1236}, {57.1362, 37.0817}, {57.1685, 37.0409}, {57.2001,  
37.0002}, {57.2319, 36.9586}, {57.2645, 36.9152}, {57.2985,  
36.8691}, {57.3346, 36.8192}, {57.3732, 36.7652}, {57.4136,  
36.7081}, {57.4555, 36.6485}, {57.4983, 36.5873}, {57.5416,  
36.5253}, {57.5848, 36.4634}, {57.6274, 36.4023}, {57.669,  
36.343}, {57.7091, 36.2863}, {57.7471, 36.2329}, {57.7827,  
36.1836}, {57.8162, 36.138}, {57.8481, 36.0955}, {57.8791,  
36.0554}, {57.9096, 36.0173}, {57.9401, 35.9804}, {57.9713,  
35.9441}, {58.0037, 35.9079}, {58.0377, 35.8711}, {58.074,  
35.833}, {58.113, 35.7931}, {58.1548, 35.7512}, {58.199,  
35.7073}, {58.245, 35.6615}, {58.2926, 35.6139}, {58.3411,  
35.5646}, {58.3902, 35.5139}, {58.4394, 35.4616}, {58.4883,  
35.408}, {58.5363, 35.3532}, {58.5831, 35.2973}, {58.6283,  
35.2404}, {58.6718, 35.183}, {58.7137, 35.1256}, {58.754,  
35.0686}, {58.7928, 35.0126}, {58.83, 34.9579}, {58.8658,  
34.9052}, {58.9, 34.8549}, {58.9328, 34.8074}, {58.9642,  
34.7632}, {58.9943, 34.7228}, {59.0231, 34.6858}, {59.0511,  
34.6512}, {59.0786, 34.6182}, {59.1059, 34.5858}, {59.1334,  
34.5531}, {59.1613, 34.5192}, {59.1899, 34.4831}, {59.2197,  
34.4441}, {59.2509, 34.4011}, {59.2838, 34.3532}, {59.3187,  
34.3001}, {59.3555, 34.2423}, {59.3942, 34.1803}, {59.4348,  
34.1149}, {59.4773, 34.0467}, {59.5215, 33.9763}, {59.5675,  
33.9045}, {59.6153, 33.8317}, {59.6647, 33.7588}, {59.7158,  
33.6863}, {59.7685, 33.6148}, {59.8222, 33.5448}, {59.8762,

33.4766}, {59.9298, 33.4106}, {59.9823, 33.3471}, {60.033,  
33.2865}, {60.0812, 33.2291}, {60.1261, 33.1753}, {60.1671,  
33.1254}, {60.2034, 33.0798}, {60.2344, 33.0387}, {60.26,  
33.0022}, {60.2808, 32.9696}, {60.2978, 32.9403}, {60.3117,  
32.9136}, {60.3232, 32.8889}, {60.3331, 32.8656}, {60.3423,  
32.8429}, {60.3514, 32.8204}, {60.3614, 32.7972}, {60.3729,  
32.7729}, {60.3865, 32.7468}, {60.4022, 32.7194}, {60.4195,  
32.6909}, {60.4383, 32.6619}, {60.4581, 32.6327}, {60.4787,  
32.6039}, {60.4997, 32.5758}, {60.5209, 32.5488}, {60.5419,  
32.5235}, {60.5623, 32.5001}, {60.582, 32.4792}, {60.6008,  
32.4605}, {60.6186, 32.4435}, {60.6357, 32.4276}, {60.652,  
32.4121}, {60.6676, 32.3964}, {60.6825, 32.38}, {60.6968,  
32.3622}, {60.7105, 32.3423}, {60.7237, 32.3199}, {60.7364,  
32.2942}, {60.7488, 32.265}, {60.761, 32.2328}, {60.7734,  
32.1982}, {60.7861, 32.162}, {60.7995, 32.1246}, {60.8138,  
32.0868}, {60.8292, 32.0493}, {60.846, 32.0125}, {60.8645,  
31.9772}, {60.8848, 31.9441}, {60.9073, 31.9136}, {60.9319,  
31.8856}, {60.9582, 31.8594}, {60.986, 31.8344}, {61.0151,  
31.81}, {61.0453, 31.7857}, {61.0762, 31.7607}, {61.1077,  
31.7345}, {61.1395, 31.7065}, {61.1712, 31.6761}, {61.2028,  
31.6426}, {61.234, 31.6058}, {61.2649, 31.5658}, {61.2956,  
31.5229}, {61.3262, 31.4774}, {61.3568, 31.4294}, {61.3873,  
31.3793}, {61.418, 31.3272}}

### A.1.4 Motion Capture Data for Knee Trajectory

Three-dimensional motion capture data of the knee of an individual for one complete gait cycle.

{-5.10647, -348.171}, {-5.3855, -348.302}, {-5.75482, -348.444}, \  
{-6.119, -348.583}, {-6.30589, -348.747}, {-6.4263, -348.915}, \  
{-6.45757, -349.087}, {-6.50565, -349.243}, {-6.81673, -349.399}, \  
{-7.19008, -349.573}, {-7.7002, -349.741}, {-8.09987, -349.903}, \  
{-8.47546, -349.946}, {-8.9153, -349.955}, {-9.16068, -349.949}, \  
{-9.39766, -350.}, {-9.85426, -350.075}, {-10.4802, -350.137}, \  
{-11.1538, -350.171}, {-11.7294, -350.12}, {-12.2277, -349.995}, \  
{-12.7384, -349.814}, {-13.4324, -349.513}, {-14.2347, -349.158}, \  
{-14.935, -348.83}, {-15.7503, -348.419}, {-16.8579, -347.849}, \  
{-18.5174, -346.746}, {-20.1286, -345.171}, {-21.4122, -343.303}, \  
{-22.7916, -341.196}, {-24.3983, -339.019}, {-26.0574, -337.205}, \  
{-27.4031, -335.845}, {-27.9876, -334.598}, {-27.5744, -333.479}, \  
{-26.3328, -332.449}, {-24.5351, -331.386}, {-22.6709, -330.255}, \  
{-21.266, -328.947}, {-20.3638, -327.333}, {-20.0686, -325.797}, \  
{-20.2993, -324.476}, {-20.9244, -323.272}, {-21.5709, -322.212}, \  
{-21.9056, -321.388}, {-21.7763, -320.815}, {-21.4867, -320.434}, \  
{-21.336, -320.168}, {-21.4705, -319.981}, {-21.9177, -319.855}, \  
{-22.6358, -319.985}, {-23.6718, -320.414}, {-24.8671, -321.21}, \  
{-25.9644, -322.321}, {-26.7961, -323.57}, {-27.2813, -324.833}, \  
{-27.6012, -326.161}, {-27.9016, -327.543}, {-28.1843, -329.049}, \  
{-28.4344, -330.717}, {-28.572, -332.309}, {-28.3253, -333.932}, \  
{-27.0978, -335.502}, {-24.5037, -336.973}, {-20.5414, -338.302}, \  
{-16.3915, -339.366}, {-11.6323, -340.159}, {-6.57821, -340.797}, \

$\{-1.33681, -341.319\}, \{3.79305, -341.721\}, \{8.07994, -341.952\}, \backslash$   
 $\{11.1447, -342.034\}, \{13.1706, -342.074\}, \{13.919, -342.241\}, \backslash$   
 $\{13.3159, -342.501\}, \{11.2396, -342.558\}, \{7.86133, -342.654\}, \backslash$   
 $\{3.93402, -342.92\}, \{0.161376, -343.281\}, \{-3.6585, -343.407\}, \backslash$   
 $\{-6.25677, -343.624\}, \{-5.30597, -344.065\}, \{-1.38382, -344.017\}, \backslash$   
 $\{3.79287, -343.573\}, \{7.30802, -343.169\}, \{6.70037, -343.342\}, \backslash$   
 $\{1.59731, -344.357\}, \{-6.05015, -345.394\}, \{-12.2493, -345.897\}, \backslash$   
 $\{-13.9784, -346.156\}, \{-11.2852, -346.585\}, \{-7.35499, -347.079\}, \backslash$   
 $\{-4.30956, -347.364\}, \{-1.7605, -347.385\}, \{0.353882, -347.203\}, \backslash$   
 $\{0.534883, -347.046\}, \{-1.65818, -347.107\}, \{-4.41745, -347.269\}, \backslash$   
 $\{-6.27238, -347.47\}, \{-6.8726, -347.791\}, \{-6.30436, -348.089\}, \backslash$   
 $\{-5.25354, -348.25\}, \{-4.67946, -348.345\}, \{-4.68513, -348.41\}, \backslash$   
 $\{-4.90242, -348.468\}, \{-5.00799, -348.51\}, \{-5.1565, -348.544\}, \backslash$   
 $\{-5.2564, -348.531\}, \{-5.36891, -348.5\}, \{-5.471, -348.499\}$

### A.1.5 Motion Capture Data for Metatarsal Trajectory

Three-dimensional motion capture data of the metatarsal of an individual for one complete gait cycle.

$\{-92.272, -26.389, 68.645\}, \{-107.808, -24.316,$   
 $73.906\}, \{-120.729, -22.233, 79.069\}, \{-130.832, -20.032,$   
 $83.768\}, \{-137.729, -17.827, 87.053\}, \{-141.009, -15.782,$   
 $88.086\}, \{-140.366, -13.758, 86.321\}, \{-136.135, -11.294,$   
 $81.847\}, \{-129.104, -8.159, 75.269\}, \{-119.891, -4.311,$   
 $67.426\}, \{-110.2, -0.343, 58.123\}, \{-102.277, 1.82,$

50.007}, {-96.717, 3.531, 45.451}, {-92.172, 3.289,  
41.278}, {-86.502, 2.932, 35.559}, {-78.565, 2.284,  
32.062}, {-69.19, 2.11, 30.362}, {-59.536, 2.572, 29.312}, {-50.68,  
2.033, 28.316}, {-41.527, 1.174, 27.766}, {-31.993, 0.565,  
27.371}, {-22.27, 0.762, 27.034}, {-12.467, 0.721, 26.702}, {-2.949,  
0.189, 26.321}, {6.613, -0.102, 26.038}, {15.989, -0.068,  
25.849}, {25.436, -0.1, 25.778}, {34.869, -0.2,  
25.757}, {44.404, -0.288, 25.835}, {53.816, -0.528,  
25.94}, {63.077, -0.641, 26.068}, {72.332, -0.608,  
26.325}, {81.459, -0.732, 26.502}, {90.601, -0.837,  
26.648}, {99.693, -0.899, 26.822}, {108.687, -0.895,  
26.973}, {117.58, -0.915, 27.153}, {126.547, -0.974,  
27.321}, {135.465, -1.092, 27.415}, {144.371, -1.176,  
27.492}, {153.253, -1.204, 27.606}, {162.297, -1.375,  
27.663}, {171.213, -1.3, 27.608}, {180.029, -1.413,  
27.561}, {188.991, -1.471, 27.58}, {197.864, -1.517,  
27.62}, {206.784, -1.584, 27.643}, {215.649, -1.63,  
27.701}, {224.471, -1.664, 27.766}, {233.237, -1.788,  
27.887}, {242.161, -1.622, 27.788}, {251.008, -1.704,  
27.853}, {259.769, -1.764, 27.961}, {268.563, -1.818,  
28.028}, {277.341, -1.847, 28.111}, {286.158, -1.859,  
28.223}, {295.059, -1.768, 28.345}, {304.046, -1.57,  
28.368}, {312.915, -1.664, 28.739}, {321.887, -1.611,  
28.931}, {330.836, -1.57, 29.119}, {339.914, -1.521,  
29.326}, {348.976, -1.494, 29.573}, {358.058, -1.523,  
29.826}, {367.165, -1.619, 30.014}, {376.405, -1.73,  
30.274}, {385.669, -1.891, 30.468}, {395.13, -2.21,

30.101}, {404.046, -2.517, 29.98}, {413.474, -2.462,  
30.347}, {423.133, -2.475, 30.92}, {432.343, -2.411,  
31.346}, {441.627, -2.047, 31.58}, {450.746, -1.812,  
31.667}, {459.398, -1.898, 32.123}, {467.572, -1.859,  
33.068}, {476.04, -1.24, 33.059}, {483.578, -0.879,  
33.598}, {490.936, -0.575, 34.248}, {498.187, -0.732,  
35.804}, {502.914, -1.129, 40.286}, {505.258, -1.448,  
45.559}, {506.077, -1.769, 51.386}, {504.605, -3.122,  
57.866}, {498.905, -6.365, 64.183}, {490.583, -9.669,  
70.114}, {480.395, -12.551, 75.146}, {469.139, -14.887,  
78.864}, {456.863, -16.809, 81.549}, {443.339, -18.455,  
83.358}, {428.416, -19.841, 84.373}, {412.029, -21.011,  
84.668}, {394.271, -21.912, 84.25}, {375.236, -22.957,  
83.417}, {355.48, -23.781, 81.923}, {335.02, -24.853,  
80.023}, {314.018, -26.139, 77.789}, {292.625, -27.627,  
75.186}, {270.876, -29.352, 72.368}, {248.79, -31.271,  
69.355}, {226.331, -33.356, 66.385}, {203.541, -35.536,  
63.578}, {180.452, -37.62, 61.081}, {157.169, -39.375,  
58.931}, {133.712, -40.603, 57.163}, {110.071, -41.201,  
55.796}, {86.238, -41.218, 54.937}, {62.356, -40.644,  
54.608}, {38.635, -39.708, 54.846}, {15.305, -38.479,  
55.769}, {-7.357, -37.063, 57.536}, {-29.114, -35.488,  
60.164}, {-49.641, -33.924, 63.458}, {-68.641, -32.371,  
67.217}, {-85.767, -30.948, 71.158}, {-100.759, -29.62, 75.227}}

## A.2 2R Synthesis with Position, Velocity and Acceleration Constraints

```
(* Show Task Pos *)

scl = 1;
taskpos = Table[{Pdata[[i, 2]], Pdata[[i, 3]]}, {i, Length[Pdata]};
xax1 = Table[{taskpos[[i, 1]] + scl*Cos[Pdata[[i, 1]]],
  taskpos[[i, 2]] + scl*Sin[Pdata[[i, 1]]]}, {i, 1, Length[taskpos]};
yax1 = Table[{taskpos[[i, 1]] + scl*Cos[Pdata[[i, 1]] + \[Pi]/2],
  taskpos[[i, 2]] + scl*Sin[Pdata[[i, 1]] + \[Pi]/2]}, {i, 1,
  Length[taskpos]};
vax1 = Table[{taskpos[[i, 1]]*Cos[Pdata[[i, 1]]] + VData[[i, 2]],
  taskpos[[i, 2]]*Sin[Pdata[[i, 1]] + \[Pi]/2] + VData[[i, 3]]}, {i, 1,
  Length[taskpos]};
aax1 = Table[{taskpos[[i, 1]]*Cos[Pdata[[i, 1]]] + AData[[i, 2]],
  taskpos[[i, 2]]*Sin[Pdata[[i, 1]] + \[Pi]/2] + AData[[i, 3]]}, {i, 1,
  Length[taskpos]};
frames = {
  Darker[Green], Line[{taskpos[[1]], xax1[[1]]},
  Line[{taskpos[[1]], yax1[[1]]},
  Line[{taskpos[[2]], xax1[[2]]},
  Line[{taskpos[[2]], yax1[[2]]},
  Blue, Line[{taskpos[[1]], vax1[[1]]},
  Line[{taskpos[[2]], vax1[[2]]},
  Magenta, Line[{taskpos[[1]], aax1[[1]]},
  Line[{taskpos[[2]], aax1[[2]]},
```

```

    Brown, PointSize[0.01], Point[taskpos]
  };
Graphics[{
  frames
}, {Axes -> True, AxesLabel -> {x, y}}]

```

(\* Complex Notation \*)

```

P0 = Pdata[[1, 2]] + I*Pdata[[1, 3]]
P1 = Pdata[[2, 2]] + I*Pdata[[2, 3]]
P0c = Pdata[[1, 2]] - I*Pdata[[1, 3]]
P1c = Pdata[[2, 2]] - I*Pdata[[2, 3]]

```

```

t0 = Pdata[[1, 1]]
t1 = Pdata[[2, 1]]

```

```

T0 = N[Exp[I*t0]]
T1 = N[Exp[I*(t1 - t0)]]
T0c = N[Exp[-I*t0]]
T1c = N[Exp[-I*(t1 - t0)]]

```

```

p0x = Pdata[[1, 2]]
p0y = Pdata[[1, 3]]
p1x = Pdata[[2, 2]]
p1y = Pdata[[2, 3]]

```

(\* Position Design Equations \*)

W = {Wx, Wy, 1} ;

Pos = Table[N[Disp[pvData[[i, 1]]]], {i, npos}]

G = {Gx, Gy, 1};

RelPos = Simplify[Table[Chop[Pos[[i]].Inverse[Pos[[1]]]],  
{i, Length[Pos]}]]

Eqns = Table[  
Simplify[Expand[N[Dot[RelPos[[i]].W - G, RelPos[[i]].W - G] - r^2]],  
{i, Length[RelPos]}]

RelEqns = Table[Chop[Simplify[Eqns[[i]] - Eqns[[1]]]],  
{i, 2, Length[Eqns]}]

(\* Velocity Design Equations

Position and Velocity Data is formatted as a pair of 3-vectors

{{theta, xtrans, ytrans}, {thetadot, xvel, yvel}}.

\*)

Om[pv\_] := {{0, -pv[[2, 1]], pv[[2, 2]] + pv[[2, 1]]\*pv[[1, 3]]}  
, {pv[[2, 1]],  
0, pv[[2, 3]] - pv[[2, 1]]\*pv[[1, 2]]}, {0, 0, 0}}

```
OmMatrices = Table[Om[pvData[[i]]], {i, Length[pvData]}
```

```
Wdot = Table[N[OmMatrices[[i]].RelPos[[i]].W],  
{i, Length[OmMatrices]}
```

```
vEqns = Table[  
  Chop[Expand[Dot[Wdot[[i]], RelPos[[i]].W - G]],  
  {i, Length[Wdot]}
```

```
(* Acceleration Design Equations *)
```

```
aEqns = {aEqn}
```

```
(* The Four Design Equations *)
```

```
Deqns = Join[RelEqns, vEqns, aEqns]
```

```
(* Solve the Design Equations *)
```

```
sol = NSolve[Deqns]
```

```
insol = 4; outsol = 3;
```

```
valW = W /. sol[[outsol]]
```

```
valG = G /. sol[[outsol]]
```

```

p0 = (rem.G) /. sol[[insol]];
pC = (rem.G) /. sol[[outsol]];
pA = (rem.W) /.
  sol[[insol]];
pB = (rem.W) /. sol[[outsol]];

(* Display *)
scale = 1;
pointA = {{2.2', 1.414}, {2.5', 3.2'}};
xax = Table[
  Flatten[{{1, 0, 0}, {0, 1, 0}}.{{1, 0, scale}, {0, 1, 0}, {0, 0,
    1}}.{{pointA[[i, 1]], {pointA[[i, 2]]}, {1}}}, {i, 1,
    Length[pointA]}];
yax = Table[
  Flatten[{{1, 0, 0}, {0, 1, 0}}.{{1, 0, 0}, {0, 1, scale}, {0, 0,
    1}}.{{pointA[[i, 1]], {pointA[[i, 2]]}, {1}}}, {i, 1,
    Length[pointA]}];
vax = Table[
  Flatten[{{1, 0, 0}, {0, 1, 0}}.{{1, 0, 0}, {0, 1, 0}, {0, 0,
    1}}.{{pointA[[i, 1]] + scale*vdat[[i, 1]], {pointA[[i, 2]] +
    scale*vdat[[i, 2]]}, {1}}}, {i, 1, Length[pointA]}];
aax = Table[
  Flatten[{{1, 0, 0}, {0, 1, 0}}.{{1, 0, 0}, {0, 1, 0}, {0, 0,
    1}}.{{pointA[[i, 1]] + scale*adat[[i, 1]], {pointA[[i, 2]] +

```

```

        scale*adat[[i, 2]], {1}], {i, 1, Length[pointA]}}];
(* Linkage description *)
pointa = pointA[[1, 1]] + I* pointA[[1, 2]];
p0 = {0.5756300589625868', 0.8578801215867536'};
pA = {0.9973958545782199', -0.1311611654707437'};
pB = {0.835676813078608', 1.4819970078101465'};
pC = {-1.102900033228121', 2.725821786025163'};
po = p0[[1]] + I*p0[[2]];
pa = pA[[1]] + I*pA[[2]];
pb = pB[[1]] + I*pB[[2]];
pc = pC[[1]] + I*pC[[2]];
\[Theta] = N[Table[i*\[Pi]/180, {i, 0, 360, 1}]];
traja = Table[
    po + (Abs[pa - po]*Exp[I*\[Theta][[i]]]), {i, Length[\[Theta]}}];
trajA = Map[{Re[#], Im[#]} &, traja];
s = Chop[Sqrt[(pc - traja)*(Conjugate[pc] - Conjugate[traja])]];
\[Phi] = ArcTan[Re[traja] - Re[pc], Im[traja] - Im[pc]];
ab = Chop[Sqrt[(pb - pa)*(Conjugate[pb] - Conjugate[pa])]];
bc = Chop[Sqrt[(pc - pb)*(Conjugate[pc] - Conjugate[pb])]];
\[Gamma] =
    Table[ArcCos[(bc^2 + s[[i]]^2 - ab^2)/(2*bc*s[[i]])], {i,
        Length[s]};
zo = -1;
trajb = Table[
    pc + (Abs[pb - pc])*Exp[I*(\[Phi][[i]] - zo*\[Gamma][[i]])], {i,
        Length[\[Gamma]}}];
trajB = Map[{Re[#], Im[#]} &, trajb];

```

```

\[Delta] =
  Table[ArcTan[Re[trajb[[i]]] - Re[traja[[i]]],
    Im[trajb[[i]]] - Im[traja[[i]]], {i, Length[traja]};
\[Alpha] =
  Sqrt[((pointa - pa)*
    Conjugate[pb - pa])/(Conjugate[pointa - pa]*(pb - pa))] ;
trajp = Table[
  traja[[i]] + (Abs[
    pointa - pa])*(Exp[I*(\[Delta] [[i]])]*\[Alpha]), {i,
    Length[\[Delta]]};
trajP = Map[{Re[#], Im[#]} &, trajp];
display = Graphics[{
  (*Task pos*)
  Darker[Green], Thickness[0.004], Line[{pointA[[1]], xax[[1]]},
  Line[{pointA[[2]], xax[[2]]},
  Line[{pointA[[1]], yax[[1]]},
  Line[{pointA[[2]], yax[[2]]},
  Blue, Line[{pointA[[1]], vax[[1]]},
  Line[{pointA[[2]], vax[[2]]},
  Thickness[0.003], Magenta, Line[{pointA[[1]], aax[[1]]},
  Line[{pointA[[2]], aax[[2]]},
  Red, PointSize[0.01], Point[pointA[[2]]],
  Point[pointA[[1]]],
  (*Linkage*)
  Blue, PointSize[0.015], Point[p0],
  Purple, Point[pA],
  Red, Point[pB],

```

```

Magenta, Point[pC],
PointSize[0.005], Purple, Point[trajA],
Red, Point[trajB],
Black, Point[trajP],
Line[{p0, pA}],
Line[{pC, pB}],
Line[{pB, pA, trajP[[1]], pB}]
}, {Axes -> True, GridLines -> Automatic, AxesLabel -> {x, z},
AxesOrigin -> {0, 0}, AxesStyle -> Directive[Black, 26],
ImageSize -> 600}]

```

## A.3 Performance Optimization

### A.3.1 Objective Function

```

ObjFunc[config_, taskpoints_, {ax_, ay_, cx_, cy_}] :=
Module[{A, B, CC, DD, F, G, H, P0, aQuad, bQuad, cQuad, Qj, aLin,
  bLin, cLin, dLin, fLin, gLin, num, numC, den, Uj, UCj, ErrorTab,
  DevError, imPt, cDist, ClosureErr, ArErr, \[Theta], cg, Gj,
  s1, \[Gamma]1, dg, ad, \[Delta]1, z1, \[Rho], Dj, \[Mu], hg, dh,
  x1, r1, Hj, s2, \[Gamma]2, bf, fh, \[Delta]2, z2, \[Psi],
  Fj, \[Phi], hp0, fp0, x2, r2, Pj, k1, k2, k3, k4, k5, k6, k7, k8,
  k9, k10, k11, k12, JJ, jErr, wC, wA, wJ, ObjFunc},
A = ax + I*ay;
B = config[[1]];

```

```

CC = cx + I*cy;
DD = config[[2]];
F = config[[3]];
G = config[[4]];
H = config[[5]];
P0 = config[[6]];
aQuad =
  Table[(Conjugate[taskpoints[[i]]] - Conjugate[B])*(P0 - F), {i,
    Length[taskpoints]}];
bQuad =
  Table[(F - B)*(Conjugate[F] - Conjugate[B]) - (taskpoints[[i]] -
    B)*(Conjugate[taskpoints[[i]]] - Conjugate[B]) - (P0 -
    F)*(Conjugate[P0] - Conjugate[F]), {i, Length[taskpoints]}];
cQuad =
  Table[(taskpoints[[i]] - B)*(Conjugate[P0] - Conjugate[F]), {i,
    Length[taskpoints]}];
Qj = Table[(-bQuad[[i]] +
  Sqrt[bQuad[[i]]^2 - 4*aQuad[[i]]*cQuad[[i]]])/(2*
  aQuad[[i]]), {i, Length[aQuad]}];
aLin = H - DD;
bLin = Table[
  Qj[[i]]*(P0 - H) - taskpoints[[i]] + A, {i, Length[taskpoints]}];
cLin = H - G;
dLin = Table[
  Qj[[i]]*(P0 - H) - taskpoints[[i]] + CC, {i, Length[taskpoints]}];
fLin = DD - A;
gLin = G - CC;

```

```

num = Table[{{fLin*Conjugate[fLin] - aLin*Conjugate[aLin] -
  bLin[[i]]*Conjugate[bLin[[i]]],
  Conjugate[aLin]*bLin[[i]]}, {gLin*Conjugate[gLin] -
  cLin*Conjugate[cLin] - dLin[[i]]*Conjugate[dLin[[i]]],
  Conjugate[cLin]*dLin[[i]]}}, {i, Length[bLin]};
numC =
Table[{{aLin*Conjugate[bLin[[i]]],
  fLin*Conjugate[fLin] - aLin*Conjugate[aLin] -
  bLin[[i]]*Conjugate[bLin[[i]]]}, {cLin*Conjugate[dLin[[i]]],
  gLin*Conjugate[gLin] - cLin*Conjugate[cLin] -
  dLin[[i]]*Conjugate[dLin[[i]]]}}, {i, Length[bLin]};
den = Table[{{aLin*Conjugate[bLin[[i]]],
  Conjugate[aLin]*bLin[[i]]}, {cLin*Conjugate[dLin[[i]]],
  Conjugate[cLin]*dLin[[i]]}}, {i, Length[bLin]};
Uj = Table[Det[num[[i]]]/Det[den[[i]]], {i, Length[num]};
UCj = Table[Det[numC[[i]]]/Det[den[[i]]], {i, Length[numC]};
ErrorTab = Table[(Chop[Uj[[i]]*UCj[[i]]] - 1)^2, {i, Length[Uj]};
DevError = Re[Chop[Total[ErrorTab]]];
\[Theta] = N[Table[i*\[Pi]/180, {i, 0, 360, 1}]];
cg = Re[Sqrt[(CC - G)*(Conjugate[CC] - Conjugate[G])]];
Gj = Table[{Re[CC] + cg*Cos[\[Theta][[i]]],
  Im[CC] + cg*Ssin[\[Theta][[i]]]}, {i, Length[\[Theta]}}];
s1 = Table[
  EuclideanDistance[Gj[[i]], {Re[A], Im[A]}], {i, Length[Gj]};
\[Gamma]1 =
Table[ArcTan[Gj[[i, 1]] - Re[A], Gj[[i, 2]] - Im[A]], {i,
  Length[Gj]};

```

```

dg = Re[Sqrt[(DD - G)*(Conjugate[DD] - Conjugate[G])]];
ad = Re[Sqrt[(DD - A)*(Conjugate[DD] - Conjugate[A])]];
\[Delta]1 =
  Table[ArcCos[(ad^2 + s1[[i]]^2 - dg^2)/(2*ad*s1[[i]])], {i,
    Length[s1]};
z1 = -1;
\[Rho] = \[Gamma]1 - z1*\[Delta]1;
Dj = Table[{Re[A] + ad*Cos\[Gamma]1[[i]] - z1*\[Delta]1[[i]],
  Im[A] + ad*Sin\[Gamma]1[[i]] - z1*\[Delta]1[[i]]}, {i,
  Length\[Gamma]1};
\[Mu] =
  Table[ArcTan[Dj[[i, 1]] - Gj[[i, 1]], Dj[[i, 2]] - Gj[[i, 2]]], {i,
    Length[Dj]};
hg = Re[Sqrt[(H - G)*(Conjugate[H] - Conjugate[G])]];
dh = Re[Sqrt[(DD - H)*(Conjugate[DD] - Conjugate[H])]];
x1 = (hg^2 - dh^2 + dg^2)/(2*dg);
r1 = Sqrt[hg^2 - x1^2];
Hj = Table[{Gj[[i, 1]] + x1*Cos\[Mu]1[[i]] +
  r1*Cos\[Pi]/2 + \[Mu]1[[i]],
  Gj[[i, 2]] + x1*Ssin\[Mu]1[[i]] +
  r1*Ssin\[Pi]/2 + \[Mu]1[[i]]}, {i, Length\[Mu]1};
s2 = Table[
  EuclideanDistance[Hj[[i]], {Re[B], Im[B]}], {i, Length[Hj]};
\[Gamma]2 =
  Table[ArcTan[Hj[[i, 1]] - Re[B], Hj[[i, 2]] - Im[B]], {i,
    Length[Hj]};
bf = Re[Sqrt[(B - F)*(Conjugate[B] - Conjugate[F])]];

```

```

fh = Re[Sqrt[(F - H)*(Conjugate[F] - Conjugate[H])]];
\Delta2 =
Table[ArcCos[(bf^2 + s2[[i]]^2 - fh^2)/(2*s2[[i]]*bf)], {i,
Length[s2]};
z2 = 1;
\Psi = \Gamma2 - z2*\Delta2;
Fj = Table[{Re[B] + bf*Cos[\Gamma2[[i]] - z2*\Delta2[[i]]],
Im[B] + bf*Sin[\Gamma2[[i]] - z2*\Delta2[[i]]]}, {i,
Length[\Gamma2]};
\Phi =
Table[ArcTan[Fj[[i, 1]] - Hj[[i, 1]], Fj[[i, 2]] - Hj[[i, 2]]], {i,
Length[Hj]};
hp0 = Re[Sqrt[(P0 - H)*(Conjugate[P0] - Conjugate[H])]];
fp0 = Re[Sqrt[(F - P0)*(Conjugate[F] - Conjugate[P0])]];
x2 = (hp0^2 + fh^2 - fp0^2)/(2*fh);
r2 = Sqrt[hp0^2 - x2^2];
Pj = Table[{Hj[[i, 1]] + x2*Cos[\Phi][[i]] +
r2*Cos[\Pi]/2 + \Phi][[i]],
Hj[[i, 2]] + x2*Sin[\Phi][[i]] +
r2*Sin[\Pi]/2 + \Phi][[i]]}, {i, Length[\Phi]};
imPt = Table[If[Im[Pj[[i]]] != {0, 0}, 1, 0], {i, Length[Pj]};
cDist = EuclideanDistance[Pj[[Length[Pj]]], Pj[[1]]];
ClosureErr = Total[imPt] + cDist;
ArErr =
If[Total[imPt] == 0,
Sqrt[(Max[Re[taskpoints]] -
Max[Pj[[;, 1]]])^2 + (Max[Im[taskpoints]] -

```

```

      Max[Pj[[;; , 2]])^2 + (Min[Re[taskpoints]] -
      Min[Pj[[;; , 1]])^2 + (Min[Im[taskpoints]] -
      Min[Pj[[;; 2]])^2], Total[imPt]];
k1 = Table[(ad^2 - dg^2 - s1[[i]]^2)/(ad*s1[[i]]^2*
      Sqrt[-(ad^4 + (dg^2 - s1[[i]]^2)^2 -
      2*ad^2*(dg^2 + s1[[i]]^2))/(ad^2*s1[[i]]^2)]), {i,
      Length[s1]};
k2 = Table[(Gj[[i, 1]] - Re[A] +
      k1[[i]]*s1[[i]]^2*(Gj[[i, 2]] - Im[A]))*
      Cos[\[Theta][[i]]] + (Gj[[i, 2]] - Im[A] -
      k1[[i]]*s1[[i]]^2*(Gj[[i, 1]] - Re[A]))*
      Sin[\[Theta][[i]]], {i, Length[s1]};
k3 = Table[(Dj[[i, 1]] -
      Gj[[i, 1]]*(-s1[[i]]^2*Cos[\[Theta][[i]]] +
      ad*k2[[i]]*Cos[\[Rho][[i]]]))/
      s1[[i]]^2 + (Dj[[i, 2]] -
      Gj[[i, 2]]*(-s1[[i]]^2*Sin[\[Theta][[i]]] +
      ad*k2[[i]]*Sin[\[Rho][[i]]]))/s1[[i]]^2, {i, Length[s1]};
k4 = Table[
      k3[[i]]*r1*Cos[\[Mu][[i]]] +
      k3[[i]]*x1*Sin[\[Mu][[i]] + dg^2*Sin[\[Theta][[i]]]], {i,
      Length[k3]};
k5 = Table[
      k3[[i]]*x1*Cos[\[Mu][[i]]] -
      k3[[i]]*r1*Sin[\[Mu][[i]] + dg^2*Cos[\[Theta][[i]]]], {i,
      Length[k3]};
k6 = Table[(bf^2 - fh^2 - s2[[i]]^2)/(bf*s2[[i]]^2*

```

```

Sqrt[-(bf^4 + (fh^2 - s2[[i]]^2)^2 -
      2*bf^2*(fh^2 + s2[[i]]^2))/(bf^2*s2[[i]]^2)], {i,
Length[s2]}}];
k7 = Table[(Hj[[i, 1]] - Fj[[i, 1]])*
  Cos[\Psi][[i]]] + (Hj[[i, 2]] - Fj[[i, 2]])*
  Sin[\Psi][[i]]], {i, Length[\Psi]}}];
k8 = Table[
  k5[[i]]*s2[[i]]*(Hj[[i, 1]] - Fj[[i, 1]]) -
  k4[[i]]*fh^2*(Re[B] - Hj[[i, 1]]) +
  k4[[i]]*s2[[i]]*(Hj[[i, 2]] - Fj[[i, 2]]) -
  k5[[i]]*fh^2*(Im[B] - Hj[[i, 2]]), {i, Length[s2]}}];
k9 = Table[(r2*Cos[\Phi][[i]]] +
  x2*Sin[\Phi][[i]])/(fh^4*(1 + k7[[i]]*s2[[i]])), {i,
Length[s2]}}];
k10 = Table[
  k5[[i]]*(Fj[[i, 1]] - Hj[[i, 1]]) +
  k4[[i]]*(Fj[[i, 2]] - Hj[[i, 2]]), {i, Length[k5]}}];
k11 = Table[(x2*Cos[\Phi][[i]]] -
  r2*Sin[\Phi][[i]])/(fh^4*(1 + k7[[i]]*s2[[i]])), {i,
Length[s2]}}];
k12 = Table[
  fh^2*(1 + k7[[i]])*s2[[i]]*k10[[i]] + bf*k8[[i]]*k7[[i]], {i,
Length[s2]}}];
JJ = Table[((k5[[i]] - k11[[i]]*k12[[i]])^2 + (-k4[[i]] +
  k9[[i]]*k12[[i]])^2), {i, Length[k12]}}];
jErr = Total[
  Table[If[Im[JJ[[i]]] != 0, 1, If[JJ[[i]] < 10^-4, 1, 0]], {i,

```

```

    Length[JJ]]]);
wA = 1;
wC = 1;
wJ = 1;
ObjFunc = DevError + wC*ClosureErr + wA*ArErr + wJ*jErr;
ObjFunc]

```

### A.3.2 Grid Search

```

(* width of grid from central point and threshold for error
- SET *)
dLimit = {{10, 10}, {10, 10}};
threshold = 0.5;
(* domain format = {{x1Min, x1Max},{y1Min, y1Max}}*)
domain = {{Round[Re[A]] - dLimit[[1, 1]],
    Round[Re[A]] + dLimit[[1, 1]]}, {Round[Im[A]] - dLimit[[1, 2]],
    Round[Im[A]] + dLimit[[1, 2]]}, {Round[Re[CC]] - dLimit[[2, 1]],
    Round[Re[CC]] + dLimit[[2, 1]]}, {Round[Im[CC]] - dLimit[[2, 2]],
    Round[Im[CC]] + dLimit[[2, 2]]}}
(* Sample domain output *)
{{-45, -25}, {-371, -351}, {46, 66}, {-356, -336}}
(* step size for grid search. Format = {step size for x1,
step size for y1} SET *)
s1 = {1, 1, 1, 1}

(* Generate nodal points of the grid where the
function is to be evaluated *)

```

```

node = ParallelTable[{domain[[1, 1]] + i, domain[[2, 1]] + j,
  domain[[3, 1]] + k, domain[[4, 1]] + 1}, {1,
  0, (domain[[4, 2]] - domain[[4, 1]]), s1[[4]]}, {k,
  0, (domain[[3, 2]] - domain[[3, 1]]), s1[[3]]}, {j,
  0, (domain[[2, 2]] - domain[[2, 1]]), s1[[2]]}, {i,
  0, (domain[[1, 2]] - domain[[1, 1]]), s1[[1]]}}];
(* Evaluate function at all nodal points *)
pass1 = ParallelTable[
  ObjFunc[config, fitPt, node[[i, j, k, 1]]],
  {i, 1, Length[node], 1}, {j, 1,
  Length[node[[1]]], 1}, {k, 1, Length[node[[1, 1]]], 1}, {1, 1,
  Length[node[[1, 1, 1]]], 1}];
(* Lowest function value in region, and associated coordinates,
and verify \
function value *)
minVal1 = Min[Re[pass1]]
{{x1, y1, x2, y2}} = Position[pass1, Min[Re[pass1]]];
node[[x1, y1, x2, y2]]
ObjFunc[config, fitPt, node[[x1, y1, x2, y2]]]

```